

Dissertation zur Erlangung des Doktorgrades
der Fakultät für Chemie und Pharmazie
der Ludwig-Maximilians-Universität München

**Exciton Mobility and Localized Defects
in Single Carbon Nanotubes Studied with
Tip-Enhanced Near-Field Optical Microscopy**

von
Carsten Georgi
aus
Schwerin

2010

Erklärung

Diese Dissertation wurde im Sinne von § 13 Abs. 3 der Promotionsordnung vom 29. Januar 1998 von Herrn Prof. Dr. Achim Hartschuh betreut.

Ehrenwörtliche Versicherung

Diese Dissertation wurde selbständig, ohne unerlaubte Hilfe erarbeitet.

München, den 09.12.2010

.....
(Unterschrift des Autors)

Dissertation eingereicht am 09.12.2010
1. Gutachter: Prof. Dr. Achim Hartschuh
2. Gutachter: Prof. Dr. Tobias Hertel
Mündliche Prüfung am 07.02.2011

Abstract

In this work, single-walled carbon nanotubes (SWNTs) have been studied using tip-enhanced near-field optical microscopy (TENOM). This technique provides a sub-diffraction spatial resolution of 15 nm on the basis of strong local signal enhancement, which allows for nanoscale imaging of the photoluminescence (PL) intensity and energy along single semiconducting SWNTs. Thereby, the mobility of excitons and their interaction with defects and spatial exciton energy variations can be directly visualized. Similarly, the local Raman scattering properties of metallic SWNTs have been investigated, revealing the microscopic relation of localized defects and the resulting Raman D-band intensity.

The first part of the thesis presents a newly developed numerical description of exciton mobility and local quenching at defect sites, accounting also for the TENOM imaging process. This highly flexible model is used to quantitatively evaluate experimental observations such as photo-induced PL blinking and strong spatial PL intensity variations of single semiconducting SWNTs. The main finding is that exciton propagation can be described as one-dimensional diffusion with a diffusion length of 100 nm for the studied nanotubes, determined independently from both the PL blinking characteristics and the direct visualization using high-resolution TENOM. The temporal and spatial PL variations result from efficient exciton quenching at localized defects and the nanotube ends.

The second part reports on the first observation of exciton localization in SWNTs at room temperature, leading to strongly confined and bright PL emission. Localization results from narrow exciton energy minima with depths of more than 15 meV, evidenced by energy-resolved near-field PL imaging. Complementary simulations using a modified numerical model accounting for energy gradients are in good agreement, predicting a significant directed diffusion towards energy minima yielding locally enhanced exciton densities. The energy variations are attributed to inhomogeneous DNA-wrapping of the nanotubes, used for their separation during sample preparation.

In the last part, the microscopic relation between the defect-induced Raman D-band and the defect density has been investigated for metallic SWNTs. The length scale of the D-band scattering process in the vicinity of defects was imaged with TENOM for the first time and found to be about 2 nm. Furthermore, localized defects have been photo-generated intentionally by the strong fields at the tip while recording the evolution of the local Raman spectrum. Based on this data, a quantitative relation could be determined, that is highly relevant for the characterization of carbon nanotubes via Raman spectroscopy.

Contents

1	Introduction	1
2	Single-walled carbon nanotubes	5
2.1	Structure	5
2.1.1	Real space lattice	5
2.1.2	Reciprocal space	8
2.2	Band structure and excitons	9
2.2.1	Derivation from graphene	10
2.2.2	Metallic SWNTs	12
2.2.3	Semiconducting SWNTs	13
2.2.4	Excitons	15
2.3	Photoluminescence	18
2.4	Raman scattering	21
2.4.1	Resonance Raman scattering	23
2.4.2	Raman scattering of graphene	23
2.4.3	Raman scattering of SWNTs	27
3	High-resolution optical microscopy	31
3.1	Propagation of light and the diffraction limit	32
3.1.1	Angular spectrum representation	32
3.1.2	The resolution limit	35
3.2	Near-field concepts	36
3.3	Tip-enhanced near-field optical microscopy	39
3.3.1	Field enhancement at a metal tip	40
3.3.2	Signal enhancement	42
3.3.3	Illumination schemes	44
3.4	Far-field concepts	46
4	Experimental details	49
4.1	TENOM setup	49
4.1.1	Confocal laser scanning microscope	49
4.1.2	Shear-force AFM	52
4.2	Sample preparation	55
4.3	Near-field imaging	56
4.3.1	APD based near-field imaging	56
4.3.2	Spectroscopic imaging	58
5	Photo-induced photoluminescence bleaching and blinking	59
5.1	Influence of excitation power and surrounding atmosphere	59
5.2	Evaluation of step-like PL bleaching and blinking	65

6	Exciton diffusion - analytical and numerical treatment	69
6.1	Analytical description	69
6.2	Numerical simulation	71
6.3	Numerical simulation of the TENOM imaging process	74
6.4	Simulation of exciton diffusion in an inhomogeneous environment	76
6.5	Modeling of time-resolved experiments	78
6.6	Influence of QY and exciton mobility on the near-field PL enhancement	80
7	Exciton mobility and quenching studied with TENOM	83
7.1	PL intensity variations along individual SWNTs	83
7.2	Exciton quenching near ends and defects - experiment and simulation	84
7.3	Exciton quenching near a localized single defect	86
7.4	Exciton diffusion length and the SWNT environment	88
8	Exciton localization visualized using near-field spectroscopic imaging	91
8.1	Observation of strongly localized PL	92
8.2	Experimental evidence for exciton energy gradients at localization sites	92
8.3	Simulation of exciton diffusion directed by energy gradients	95
8.4	Origin of the exciton energy variations	96
9	High-resolution spectroscopic imaging of localized defects	99
9.1	Spatial extension of the D-band scattering process	99
9.2	Tip-induced generation of localized defects	103
9.3	Relation between defect density and D-band intensity	105
10	Summary and outlook	107
	Appendix: Tip-enhanced Raman scattering on single-layer graphene	111
	Bibliography	117
	Abbreviations	131
	List of Figures	133
	List of Publications	135
	List of Conferences	137
	Acknowledgments	139

1 Introduction

In the last two decades, the newly discovered nanoscale allotropes of carbon - namely fullerenes, carbon nanotubes and graphene - have attracted enormous interest due to their unique electronic and optical properties. The huge attention directed to this research field is exemplified by the two Nobel prizes that have been awarded for the discovery of fullerenes and graphene. These nanoscale carbon materials hold great promise for applications in future nano- and optoelectronic devices, as well as chemical sensors and photovoltaics.

Single-walled carbon nanotubes (SWNTs) are quasi one-dimensional objects that can be regarded as seamless cylinders formed by rolling up a narrow ribbon of graphene. The wide variety of possible structures, defined by their geometry with respect to the graphene lattice, results in many specific optical and electronic properties that can be exploited in future devices [1, 2]. SWNTs can be either metallic with a very high current-carrying capacity up to 10^9 A/cm^2 , or they can be semiconducting with band gap energies in the range of $0.5 - 1.5 \text{ eV}$ and charge carrier mobilities up to $10^5 \text{ cm}^2/\text{Vs}$ [3]. Importantly, the one-dimensional nature of carbon nanotubes leads to an excitonic character of the optical excitations, which strongly affects their optical properties [4, 5]. For any application, it is necessary to understand the interaction of the charge-carriers and excitons with lattice vibrations (phonons), structural defects and the nanotube environment.

Optical spectroscopy is an ideal tool to study these effects. Structural properties and electron phonon-coupling are expressed in the Raman scattering spectrum, whereas the exciton properties are reflected in the photoluminescence (PL) of semiconducting SWNTs [6, 7]. Optical microscopy can be used to image these information on the single nanotube level. However, owing to the diffraction limit in conventional far-field microscopy, the spatial resolution that can be attained is limited to about few hundred nanometers. Variations that occur on length scales far below the wavelength of the light can therefore not be examined. A sophisticated approach is needed to study the carbon nanotube optical properties on the nanoscale, since the relevant length scales and interaction ranges are often only a few nanometers.

Near-field optical microscopy exploits the fact that sub-wavelength spatial information is contained in the near-field of the sample, but can not be carried by propagating waves and is therefore not detectable in a conventional microscope [8]. When the sample is excited or probed in its near-field using e.g. a tiny sub-wavelength aperture within few nanometers distance, the diffraction limit can be circumvented and the spatial resolution

is only defined by the aperture size. This approach, nowadays known as scanning near-field optical microscopy (SNOM) has been proposed already in 1928 by E. H. Synge and could be realized experimentally in the mid 80's [9]. It has since then been successfully applied for nanoscale imaging of optical phenomena such as single molecule fluorescence or plasmonic near-fields [10, 11].

The specific approach used in this work is tip-enhanced near-field optical microscopy (TENOM) which has been proposed in 1985 by John Wessel [12]. Instead of using an aperture as the near-field probe, the strongly confined optical field enhancement in the vicinity of a laser-illuminated sharp gold tip is used to realize a nanoscale light source and detector. This has the important advantage of an enormous signal enhancement which facilitates the nanoscale imaging and spectroscopy of weak optical signals such as Raman scattering. Using this technique, the Raman scattering and photoluminescence properties of individual SWNTs on a substrate can be imaged with a spatial resolution of 15 nm [13, 14]. Interactions of phonons and structural defects as well as the exciton distribution and their energy can thereby be investigated on length scales of few nanometers.

In this thesis, TENOM was applied to study the exciton propagation and interaction with quenching defects and the nanotube environment. The exciton propagation was found to follow a one-dimensional diffusion process with a diffusion length of about 100 nm, which can be directly visualized with TENOM. In the case of strong exciton energy variations that can result from the nanotube environment, it was observed that excitons get localized at energy minima, which leads to spatially confined PL emission with high intensity. Furthermore, the interplay of structural defects and the local Raman scattering spectrum has been investigated, yielding a quantitative relation between the defect density and a characteristic Raman scattering response. This can be used to determine the defect density from a simple measurement of the Raman spectrum, which is highly relevant for carbon nanotube metrology.

The thesis is structured as follows. After this introduction, chapter 2 introduces the fundamental structural and optical properties of single-walled carbon nanotubes. Based on the underlying two-dimensional graphene lattice, the geometry and systematic description of the many different SWNT types are discussed. Then, their particular electronic band structure is derived, which is significantly modified by the excitonic character of the excited states. Based on this, their photoluminescence properties are briefly presented, reflecting the exciton properties of the nanotube. Finally, the Raman scattering process in SWNTs is introduced, which is connected to their structural properties.

Chapter 3 provides the fundamental principles of high-resolution optical microscopy, starting from the description of light propagation and the resulting resolution limit. Afterwards, different near-field concepts to overcome the diffraction limit are discussed, which offer nanoscale spatial resolution at optical light frequencies. The particular approach used in this work - tip-enhanced near-field optical microscopy - is then introduced in more

detail, including the physical basics of near-field enhancement and possible experimental realizations. At the end of this chapter, the expanding field of far-field nanoscopy is briefly discussed and its strengths and weaknesses are compared to the near-field approach.

Following this, chapter 4 describes the experimental setup that was used to perform TENOM in this work. Furthermore, the sample preparation process is specified and the different modes for the acquisition of near-field optical images are presented, including typical examples of experimental data.

Experimental results are discussed starting from chapter 5. Here, the photoluminescence properties of individual nanotubes under laser irradiation were studied using far-field excitation and detection. The temporal evolution of the PL intensity depending on the incident laser power was investigated for different substrates and atmospheres. Generally, bleaching and pronounced blinking of the PL intensity was observed. It was found that the bleaching rate increases with laser power and is lower in argon atmosphere compared to air. The bleaching is attributed to photo-induced oxidation of the SWNTs, which introduces hole-doping and thereby leads to efficient exciton quenching. Step-like changes of the PL corresponding to the impact of individual quenching sites were analyzed regarding the relative intensity change. The strong PL decrease results from a high exciton mobility in SWNTs, as this determines the influence range of quenching. Based on these experiments, an exciton excursion range of 105 nm was estimated.

Chapter 6 introduces the analytical and numerical description of exciton diffusion, which is necessary to accurately evaluate the experimental results, as e.g. the PL blinking traces in chapter 5. The calculation of the exciton distribution in SWNTs interacting with distinct quenching sites is extended to account also for the TENOM imaging process. It is shown that the numerical simulations can reproduce experimental images and that they are required to understand and determine the underlying nanotube properties. The simulations have been subsequently applied to derive the exciton diffusion length based on a near-field PL image, as reported in chapter 7. A further modification of the model is presented, which accounts for the non-uniform exciton energy along SWNTs, often seen in TENOM experiments. Thereby, exciton diffusion is directed towards energy minima which can explain the observation of exciton localization in chapter 8. The last two sections show that the model can also be used to describe time-resolved PL experiments and study the influence of quantum yield and exciton mobility on the signal enhancement in a TENOM experiment.

Chapter 7 presents experimental near-field PL measurements revealing the impact of individual quenching sites by nanoscale imaging of the PL distribution along SWNTs. It is often found that the PL intensity varies strongly along the nanotube, showing alternating bright and dark sections on length scales below 100 nm. By employing the numerical model, these observations can be interpreted by few distinct quenching sites on the SWNT. The good agreement between simulation and experiment supports the simple description

of exciton diffusion and quenching at specific defect locations as introduced in chapter 6. For the case of PL quenching near an individual defect site, a quantitative analysis of the TENOM image is possible and the exciton diffusion range can be determined as 100 ± 20 nm. This is in good agreement with the value reported earlier and demonstrates that TENOM can directly visualize exciton propagation.

The following chapter 8 reports on the observation and experimental verification of exciton localization in SWNTs. In contrast to quenching defect sites, localization leads to a locally enhanced PL intensity caused by an increased exciton density at localization sites. The inhomogeneous exciton density is attributed to exciton energy variations along the SWNT that modify the diffusion process and add a driving force towards energy minima. Spectroscopic near-field PL imaging is used to correlate PL intensity and energy with nanoscale resolution. This shows that the localization sites are connected to narrow exciton energy minima with depths of more than 15 meV and lateral energy gradients exceeding 2 meV/nm. Accompanying numerical simulations accounting for the exciton energy variations further support this picture.

In chapter 9, localized defects are imaged by near-field Raman spectroscopy. The experiments were performed on metallic SWNTs where the resonance Raman process allows for a detailed investigation of the Raman spectrum reflecting the nanotube's structural properties. The spatial extent of the defect-induced Raman D-band scattering process in the vicinity of localized defects was imaged with nanoscale resolution and found to be about 2 nm only. In addition, localized defects were intentionally generated using the strong optical fields at the tip and the temporal evolution of the D-band intensity was recorded simultaneously. From these experiments, a relation between defect density and resulting D-band intensity could be derived, which is of high relevance for the characterization of SWNTs via Raman spectroscopy.

In the end, a brief summary of the most important results reported in this thesis will be given and a following outlook provides some ideas on future experiments and the application of TENOM to different nanoscale systems.

2 Single-walled carbon nanotubes

Single-walled carbon nanotubes have attracted great interest since their discovery in 1993, now almost two decades ago [15]. They consist of sp^2 hybridized carbon atoms only and are thus closely related to fullerenes (also known as "buckyballs"), graphite and the now famous graphene. The latter can be viewed as the "mother of all graphitic forms" with its highly symmetric 2D honeycomb lattice, from which the unique structures of the others can be derived [16]. In this description, carbon nanotubes are tiny cylinders made by rolling-up a narrow sheet of graphene. They exhibit exceptional mechanical, electronic and optical properties that arise from the strong bonding and the unique electron system of sp^2 carbon atoms. With diameters in the range of 0.4 to several nanometers and a possible length of centimeters, SWNTs can be described as one-dimensional system, which leads to very interesting physical properties as e.g. the structure-dependent opening of a band gap accompanied by photoluminescence in the near-infrared. This makes them promising candidates for integration into future optoelectronic and nano-electronic devices. So far, applications still lag behind the expectations, but nanotube research stays a very active field.

In the following, the fundamental structural and electronic properties of SWNTs will be described, starting from the "parent material" graphene. Based on this, the specific band-structure and the nature of optical excitations in SWNTs will be discussed. Afterwards, the basic photoluminescence properties are introduced. Then, the most important features of the Raman scattering process are presented which reflect the vibrational properties of SWNTs.

2.1 Structure

This section introduces the structural and geometrical properties of SWNTs and their derivation from the graphene lattice. It is based on refs. 1 and 2.

2.1.1 Real space lattice

Single-walled carbon nanotubes are commonly described as seamless cylinders made by rolling-up a single narrow ribbon of graphene. Based on the 2D honeycomb lattice of a graphene sheet, there are many different ways to roll this sheet into a cylinder, differing

in their direction with respect to the lattice and the resulting nanotube diameter. The specific structure of a certain SWNT type is defined by the chiral vector \mathbf{C}_h , which can be expressed in terms of the two graphene lattice vectors \mathbf{a}_1 and \mathbf{a}_2 . Figure 2.1a shows the real space lattice of graphene with these lattice vectors.

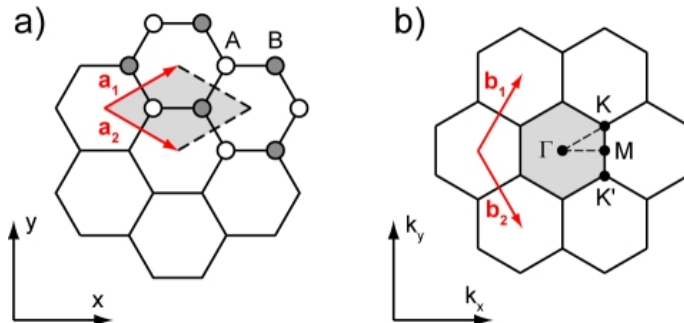


Figure 2.1: a) Real space lattice of graphene. The basis vectors \mathbf{a}_1 and \mathbf{a}_2 define the unit cell (gray shaded area). Each unit cell contains two non-equivalent carbon atoms, belonging to the sublattices A and B. b) Unit cell of graphene in reciprocal space. \mathbf{b}_1 and \mathbf{b}_2 are the reciprocal lattice vectors. The gray shaded area is the first Brillouin zone. Also shown are the high symmetry points Γ , K , K' and M .

The length of these lattice vectors is connected to the carbon-carbon bond length of 0.142 nm by $|\mathbf{a}_1| = |\mathbf{a}_2| = a_0 = \sqrt{3} \cdot 0.142 \text{ nm} = 0.246 \text{ nm}$. In x-y coordinates, the basis vectors can be expressed as

$$\mathbf{a}_1 = \left(\frac{\sqrt{3}}{2}, \frac{1}{2} \right) \cdot a_0, \quad \mathbf{a}_2 = \left(\frac{\sqrt{3}}{2}, -\frac{1}{2} \right) \cdot a_0. \quad (2.1)$$

The chiral vector \mathbf{C}_h is given by

$$\mathbf{C}_h = n \cdot \mathbf{a}_1 + m \cdot \mathbf{a}_2 \quad (2.2)$$

with the pair of positive integer numbers (n, m) that unambiguously define the specific SWNT structure, denoted as "chirality". The nanotube is formed by rolling the graphene sheet along this chiral vector, so that its origin and endpoint meet and it becomes the nanotube circumference. This is schematically shown in Fig. 2.2 for three different chiralities. The diameter d_t of the SWNTs is simply the length of \mathbf{C}_h divided by π .

$$d_t = \frac{|\mathbf{C}_h|}{\pi} = \frac{a_0}{\pi} \sqrt{n^2 + nm + m^2} \quad (2.3)$$

The direction of the chiral vector is given by the chiral angle θ , which is the angle between \mathbf{C}_h and \mathbf{a}_1 .

$$\cos \theta = \frac{\mathbf{a}_1 \cdot \mathbf{C}_h}{|\mathbf{a}_1| \cdot |\mathbf{C}_h|} = \frac{2n + m}{2\sqrt{n^2 + nm + m^2}} \quad (2.4)$$

Due to symmetry in the graphene lattice, all possible SWNT chiralities (n, m) can be described within the limit of $n \geq m \geq 0$ and thus $0^\circ \leq \theta \leq 30^\circ$. All other (n, m) have an equivalent in this range. Nanotubes of the type $(n, 0)$ and $\theta = 0^\circ$ are called zig-zag

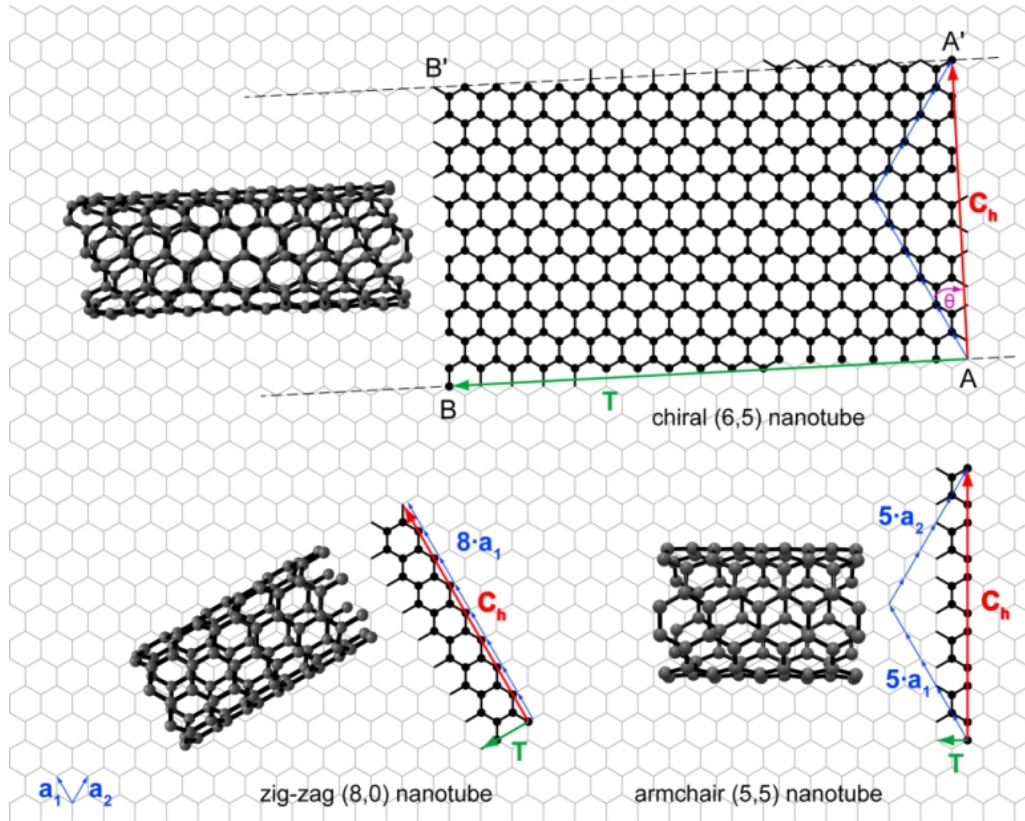


Figure 2.2: Schematic of the formation of SWNTs by rolling-up a graphene sheet, shown for three different chiralities together with the resulting nanotube structures. The rectangle $ABB'A'$ is the unit cell of the (6,5)-SWNT, which can be rolled-up along the chiral vector \mathbf{C}_h to form a seamless cylinder by connecting the lines AB and $A'B'$. The (8,0) and (5,5)-SWNT are formed accordingly, their unit cells are also highlighted. \mathbf{a}_1 and \mathbf{a}_2 are the lattice vectors of graphene, \mathbf{T} is the translational vector and θ is the chiral vector of the SWNTs.

tubes, because they exhibit a zig-zag pattern along the circumference. (n,n) -tubes with $\theta = 30^\circ$ are called armchair tubes. The characteristic patterns along \mathbf{C}_h can also be seen in Fig. 2.2. These both types are achiral. All other (n,m) -types are chiral SWNTs having a mirror image structure (m,n) with an opposite handedness.

The translational vector \mathbf{T} is the basis vector along the nanotube axis and is thus perpendicular to \mathbf{C}_h in the unrolled graphene lattice. Its length is the shortest distance between two equivalent carbon atoms in this direction. \mathbf{T} is given by

$$\mathbf{T} = \frac{2m+n}{d_r} \cdot \mathbf{a}_1 - \frac{2n+m}{d_r} \cdot \mathbf{a}_2 \quad (2.5)$$

where d_r is the greatest common divisor of $(2m+n)$ and $(2n+m)$. The SWNT unit cell is a cylinder with the diameter d_t and a length of $|\mathbf{T}| = \sqrt{3} \cdot |\mathbf{C}_h|/d_r$. The number of

hexagons per unit cell N can be calculated from the surface area $|\mathbf{C}_h| \cdot |\mathbf{T}|$ divided by the area of one hexagon, which is $\sqrt{3}a_0^2/2$. It is

$$N = \frac{2\sqrt{n^2 + nm + m^2}}{d_r}. \quad (2.6)$$

Since every hexagonal graphene unit cell contains two carbon atoms, the number of carbon atoms per SWNT unit cell is $2N$. For zig-zag $(n,0)$ and armchair (n,n) tubes, this number is $4n$ and thus relatively small. Chiral SWNTs can have very large unit cells. Comparing for example a $(6,5)$ and a $(5,5)$ tube with almost similar diameter, the number of carbon atoms per unit cell are 182 and 20, respectively.

2.1.2 Reciprocal space

In the previous section, the structure and geometry of the SWNT unit cell in real space was introduced. The counterpart in reciprocal space is the Brillouin zone. Starting point is the hexagonal Brillouin zone of graphene, shown as the grey shaded area in Fig. 2.1b. The basis vectors \mathbf{b}_1 and \mathbf{b}_2 of the reciprocal lattice are given by

$$\mathbf{b}_1 = \left(\frac{1}{\sqrt{3}}, 1 \right) \cdot \frac{2\pi}{a_0}, \quad \mathbf{b}_2 = \left(\frac{1}{\sqrt{3}}, -1 \right) \cdot \frac{2\pi}{a_0}. \quad (2.7)$$

For the two-dimensional graphene, the reciprocal wave vector \mathbf{k} can take any value in the two-dimensional Brillouin zone. For SWNTs however, the wave vector component k_\perp along their circumference, i.e. perpendicular to their axis, will be quantized due to the boundary condition of a fixed circumference. The wave function of an electron or phonon must have a phase shift of an integer multiple of 2π along the circumference, otherwise the wave function will vanish due to destructive interference. This leads to

$$k_{\perp,\mu} = \mu \cdot \frac{2\pi}{|\mathbf{C}_h|} \quad (2.8)$$

where μ is an integer in the range of $-N/2 + 1 \dots N/2$ and thus has N possible values. This constraint stems from the fact, that the maximum wave vector (minimum wavelength) of the wave function along the circumference is limited by the number of carbon atoms in the unit cell ($2N$). At least 4 carbon atoms are necessary to define a wavelength which requires $|\mu| \leq N/2$.

The wave vector component k_\parallel along the nanotube axis can have continuous values in the interval $[-\pi/|\mathbf{T}|, \pi/|\mathbf{T}|]$, because the nanotube can be treated as infinitely long in real space, with a translational period given by $|\mathbf{T}|$.

We can define the two reciprocal lattice vectors \mathbf{K}_1 and \mathbf{K}_2 which correspond to the real space basis vectors \mathbf{C}_h and \mathbf{T} , respectively. Then \mathbf{K}_1 relates to the nanotube circumference

and \mathbf{K}_2 is the maximum wave vector along the nanotube axis. The two vectors are defined by the relations

$$\begin{aligned} \mathbf{K}_1 \cdot \mathbf{C}_h &= 2\pi & \mathbf{K}_1 \cdot \mathbf{T} &= 0 \\ \mathbf{K}_2 \cdot \mathbf{C}_h &= 0 & \mathbf{K}_2 \cdot \mathbf{T} &= 2\pi \end{aligned} \quad (2.9)$$

which yields

$$\mathbf{K}_1 = \frac{2n+m}{Nd_r} \mathbf{b}_1 + \frac{2m+n}{Nd_r} \mathbf{b}_2 \quad (2.10)$$

$$\mathbf{K}_2 = \frac{m}{N} \mathbf{b}_1 - \frac{n}{N} \mathbf{b}_2. \quad (2.11)$$

The Brillouin zone of a SWNT is then defined by the wave vectors \mathbf{k} with

$$\mathbf{k} = k_{\parallel} \cdot \frac{\mathbf{K}_2}{|\mathbf{K}_2|} + \mu \cdot \mathbf{K}_1 \quad \text{with } k_{\parallel} \in \left[-\frac{\pi}{|\mathbf{T}|}, \frac{\pi}{|\mathbf{T}|} \right]. \quad (2.12)$$

It consists of N equidistant one-dimensional lines, with a length of $2\pi/|\mathbf{T}|$ and spaced by $2\pi/|\mathbf{C}_h|$. Examples for the first Brillouin zone of three different SWNTs are shown in Fig. 2.3 with respect to the graphene lattice.

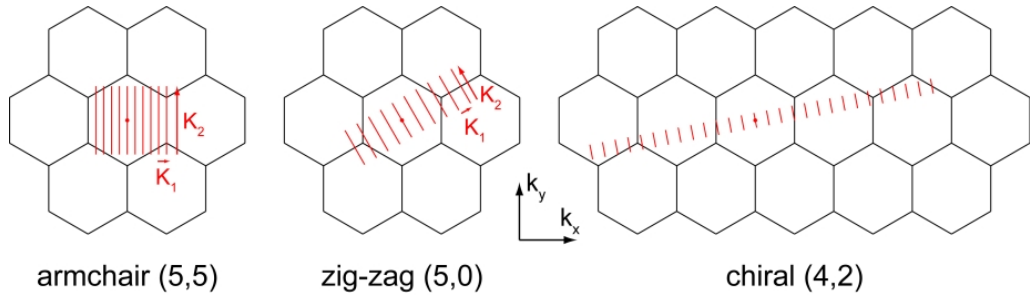


Figure 2.3: The Brillouin zones for the (5,5), (5,0) and (4,2)-SWNT (red lines) with respect to the reciprocal graphene lattice. In direction of the nanotube circumference, the possible wave vectors are quantized due to the boundary condition of the finite circumference. Only the wave vector component \mathbf{k}_{\parallel} along the nanotube axis is continuous. The SWNT Brillouin zone therefore consists of N equidistant one-dimensional lines.

For armchair tubes, the Brillouin zone always includes the K -point, whereas for zig-zag and chiral tubes this is only the case if $n - m$ is a multiple integer of 3. As will be discussed in the next section, this has fundamental consequences for their electronic band structures.

2.2 Band structure and excitons

The electronic properties of SWNTs are very closely related to those of graphene. To a good approximation, their band structure can be derived simply by taking line cuts from the 2D band structure of graphene which correspond to the nanotube's Brillouin zone. This commonly used approach is the so called *zone folding*. Though the curvature of the SWNT is neglected, this approach is very useful to understand the fundamental relations without any extensive calculations.

2.2.1 Derivation from graphene

In order to use the zone folding approach, the 2D band structure of graphene has to be calculated. Each of the carbon atoms has four valence electrons, 2s and 2p electrons. The s , p_x and p_y orbitals hybridize to three sp^2 orbitals which form the three in-plane σ -bonds. The three σ -electrons are strongly bound and can be neglected in the calculation of the electronic and optical properties. The fourth electron occupies the out-of-plane p_z orbital, forming the π -bonds which represent the electronic system of graphene. Since σ - and π -bonds are orthogonal, there is no wave function overlap and they can be treated independently. The bonding π and the anti-bonding π^* orbitals represent the valence and conduction band, respectively. Starting from the atomic p_z orbitals, these molecular orbitals can be derived by a tight-binding approach, based on a linear combination of the atomic orbitals (LCAO ansatz). For simplification, only interactions with the nearest neighboring atoms are taken into account. A detailed description of the calculation can be found in refs. 1,2,17 and the discussion here will be limited to the final solution. One obtains the following equation for the 2D electronic dispersion of graphene

$$E_G(\mathbf{k}) = \frac{\epsilon_{2p} \pm t \cdot w(\mathbf{k})}{1 \pm s \cdot w(\mathbf{k})} \quad (2.13)$$

where the + and the - sign correspond to the π valence band and the π^* conduction band, respectively. The function $w(\mathbf{k})$ is given by

$$w(\mathbf{k}) = \sqrt{1 + 4 \cos \frac{\sqrt{3}k_x a_0}{2} \cos \frac{k_y a_0}{2} + 4 \cos^2 \frac{k_y a_0}{2}}. \quad (2.14)$$

Commonly used parameters are $\epsilon_{2p} = 0$, $t = -3.033 \text{ eV}$ and $s = 0.129$. Fig. 2.4a shows the 2D band structure of graphene in the first Brillouin zone. Apparently, the valence and conduction bands cross at the K and K' points. The density of states (DOS) at these 6 points is zero, therefore graphene is a semimetal or zero-gap semiconductor. The dispersion relation near the K -points is linear and radially symmetric, similar to the surface of a cone. This is depicted in Fig. 2.4c. Due to this linear dispersion, the electrons and holes in graphene behave as massless Dirac fermions, which makes graphene such an interesting model system. It can be seen from the equipotential lines in Fig. 2.4a, that the cone-shaped dispersion becomes more triangular with increasing distance from the K -point. This deviation is usually referred to as *trigonal warping*. Owing to this trigonal warping effect, the deviation from the linear dispersion increases faster along the $K \rightarrow M$ direction than along the $K \rightarrow \Gamma$ direction, which is shown in Fig. 2.4d.

Using the zone-folding approximation, one can now derive the SWNT band structure from the graphene energy dispersion by simply using the energy values along the N lines of the SWNT Brillouin zone, projected onto the \mathbf{K}_2 -direction. This band structure is one-dimensional and plotted against k_{\parallel} , with N branches for each the valence and conduction band. Using the equations 2.12 and 2.13, it can be written as

$$E_{SWNT}(k_{\parallel}, \mu) = E_G(\mathbf{k}) = E_G \left(k_{\parallel} \cdot \frac{\mathbf{K}_2}{|\mathbf{K}_2|} + \mu \cdot \mathbf{K}_1 \right). \quad (2.15)$$

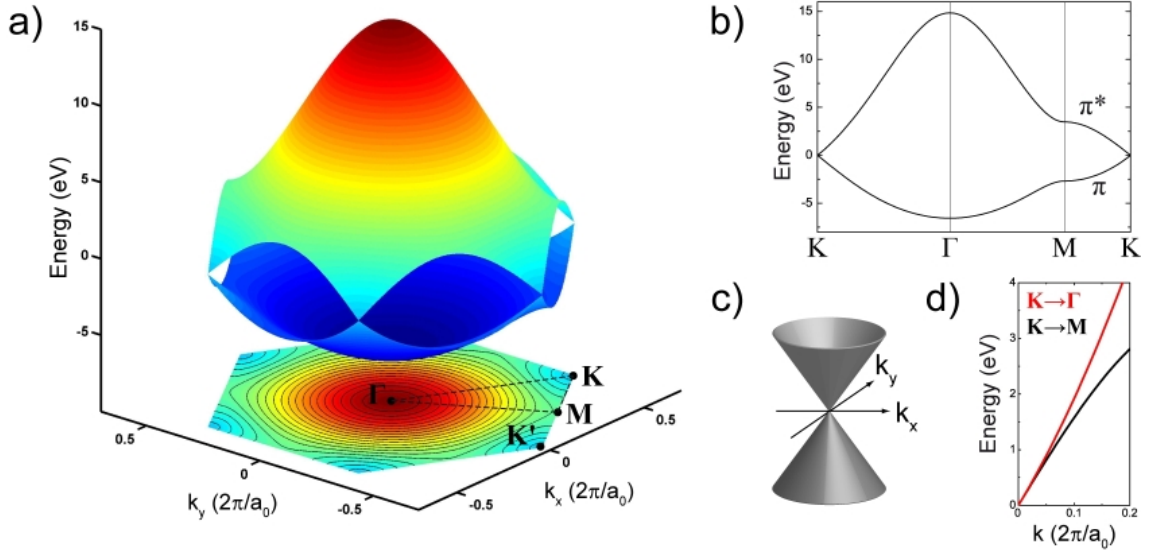


Figure 2.4: a) The two-dimensional electronic dispersion relation of graphene in the first Brillouin zone. Below is the projection of the π^* conduction band onto the reciprocal unit cell, including the equipotential lines. The high symmetry points Γ , K , K' and M are marked. b) Dispersion relation along the connecting lines between the high symmetry points (dashed lines in a). c) Illustration of the cone-shaped linear dispersion near the K -points. d) Energy dispersion of the π^* band near the K -point, comparing the directions $K \rightarrow \Gamma$ and $K \rightarrow M$. With increasing distance from the K -point, the $K \rightarrow M$ -direction deviates much stronger from the linear relation, which is the trigonal warping effect.

This zone-folding approach is illustrated in Fig. 2.5a, where the cutting lines for a (5,0)-SWNT are plotted onto the 2D electronic dispersion of graphene. The calculated band structures and density of states (DOS) for the (5,0), (5,5) and (6,0)-SWNT are plotted in Fig. 2.5b-d. For armchair and zig-zag tubes, all branches except the ones for $\mu = 0$ and $\mu = N/2$ are doubly degenerate and there are only $N/2 + 1$ branches for the valence and conduction band of these tubes.

For the discussion of optical transitions and transition probabilities, the density of states of a system is a fundamental property. The DOS specifies the number of available states in an energy interval $[E, E + \Delta E]$. For the one-dimensional band structure of SWNTs, it is given by

$$\text{DOS}(E) \propto \sum_{\mu} \frac{dk_{\parallel}(E)}{dE}. \quad (2.16)$$

The DOS is usually calculated numerically, since the inverse dispersion relation $k_{\parallel}(E)$ can often not be described analytically. The maxima and minima in the 1D band structure $E(k_{\parallel})$ give rise to singularities, where the DOS goes to infinity (see Fig. 2.5b-d). These are known as Van Hove singularities (vHS). In the simple free-particle picture, optical transitions in SWNTs occur predominantly between these vHSs due to the high transition probability, arising from the large DOS of initial and final state. As discussed later, charge-carrier Coulomb interactions can not be neglected in SWNTs which modifies the description

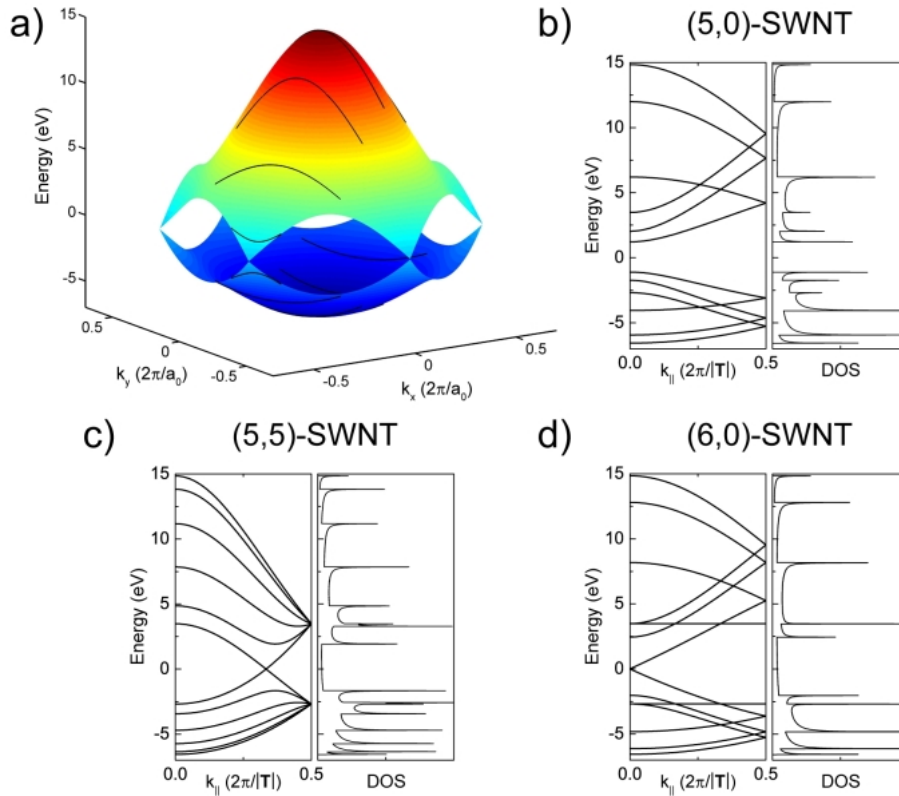


Figure 2.5: a) Illustration of the zone-folding approach for the (5,0)-SWNT. The band structure of the SWNT is derived by taking the values of the graphene energy dispersion (colored 3D surface) along the N lines corresponding to the Brillouin zone of the nanotube (black lines). These values are then plotted against k_{\parallel} , which is the wave vector along the SWNT axis. b - d) Band structure and density of states for the (5,0), (5,5) and (6,0)-SWNT.

of the optical transitions. The transitions are denoted as E_{ij} , where i and j are the indices of the involved vHSs of valence and conduction band, respectively. The vHSs closest to the Fermi level have the index 1 and the lowest transition is therefore E_{11} .

2.2.2 Metallic SWNTs

If the chirality (n,m) of a SWNT fulfills the condition $(n - m) \bmod 3 = 0$, the nanotube is metallic. The Brillouin zone of these SWNTs includes at least one $K(K')$ -point where the valence and conduction band touch (see Fig. 2.6b). Due to the cone-shaped energy dispersion of graphene near the K -point, the bands of the SWNT near this touching point are linear. This gives rise to a flat and finite DOS near the Fermi level and the absence of a band gap (see Fig. 2.5c-d). From all possible nanotube chiralities, one third is metallic. If curvature corrections beyond the simple zone folding approximation are taken into account, it can be shown that only armchair tubes are truly metallic, whereas the other types with $n - m = 3, 6, 9, \dots$ exhibit a small secondary band gap of a few meV that influences the

transport properties at low temperatures. The optical transitions in metallic SWNTs are denoted as E_{ij}^M .

2.2.3 Semiconducting SWNTs

The SWNTs with chiralities (n,m) where $(n-m) \bmod 3 \neq 0$ are semiconducting and exhibit a direct band gap. The cutting lines of the Brillouin zone do not include the K -point and the closest line is always $|\mathbf{K}_\perp|/3 = 2/3d_t$ away. As can be seen in Fig. 2.5b, the density of states between the first pair of vHSs is zero and the lowest possible transition is E_{11}^S , which is the band gap. Due to the linear dispersion near the K -point, the band gap energy scales linearly with the distance to the K -point and thus inversely with diameter. Using the linear approximation of eqs. 2.13 and 2.14 near the K -point ($k_x = 0, k_y = 4\pi/3a_0 + \Delta k$), it is

$$E_{11}^S \approx 2 \cdot \frac{dE_G}{dk} \cdot \Delta k = 2 \cdot \frac{\sqrt{3}a_0t}{2} \cdot \frac{2}{3d_t} = \frac{2a_0t}{\sqrt{3}d_t}. \quad (2.17)$$

This equation fits very well for diameters >1.5 nm where the distance from the K -point is small enough to be in the linear dispersion range. For smaller diameter tubes, the deviations increase and they are strongly influenced by the trigonal warping. For semiconducting SWNTs with $(2n+m) \bmod 3 = 1$, denoted S1, the minimum energy gap is at the intersection of the closest cutting line with the $K \rightarrow \Gamma$ direction, which can be seen in Fig. 2.6b. For semiconducting SWNTs with $(2n+m) \bmod 3 = 2$, denoted S2, the energy gap is on the $K \rightarrow M$ direction and thus smaller due to the trigonal warping (see Figs. 2.6b and 2.4d).

Figure 2.6a shows the so called Kataura-plot, where the transition energies E_{ii} of any nanotube chirality is plotted against its diameter. It was first introduced by Hiromishi Kataura in 1999 [19]. The inverse scaling with diameter and the deviations for smaller diameters can be clearly seen. The different systematic deviations for S1 and S2 nanotubes arise from the trigonal warping effect. It is also apparent, especially for the higher transitions, that groups of data points are close-by and form little patterns. These groups of chiralities have the same $(2n+m)$ value, but a different chiral angle and thus different influence of trigonal warping. These patterns are commonly referred to as family patterns.

The optical transitions in SWNTs have a strong polarization dependence. For E_{ii} -transitions that connect the valence and conduction band from the same line of the Brillouin zone, $\Delta\mu$ and hence Δk_\perp are zero. Δk_\parallel depends on the wave vector of the interacting light which is oriented along the nanotube axis and comparably small ($\Delta k_\parallel \approx 0$). These transitions are therefore polarized along the nanotube axis, i.e. they interact only with the field components parallel to the tube.

The E_{ij} -transitions with $i \neq j$ connect different lines of the Brillouin zone with $|\Delta\mu| \geq 1$ and $|\Delta k_\perp| \geq 2\pi/|\mathbf{C}_h|$, which is much larger than Δk_\parallel . These transitions are therefore polarized perpendicular to the tube axis. However, the absorption of light with perpendic-

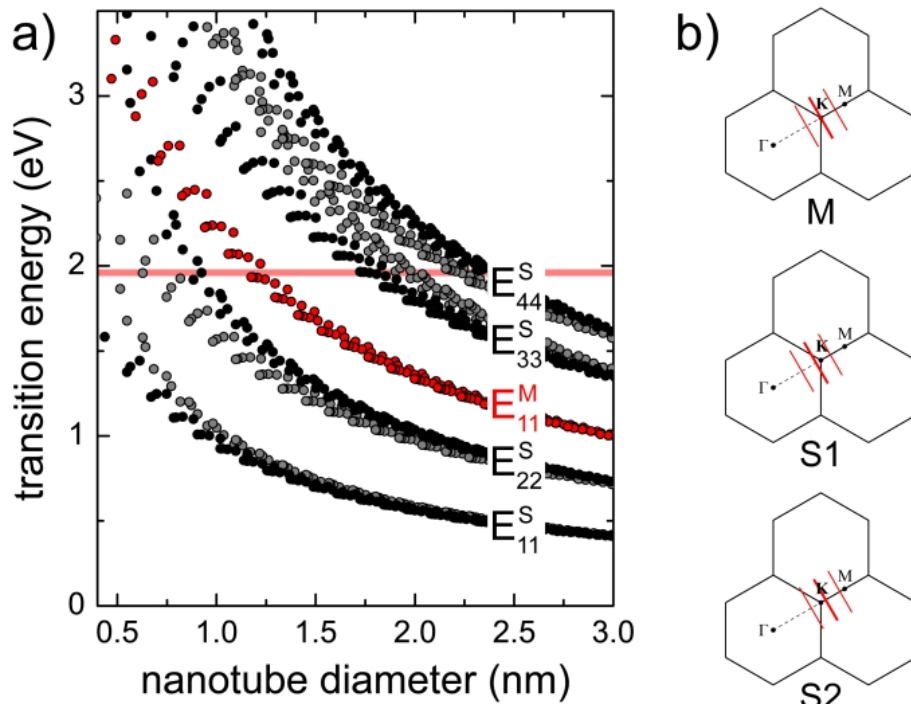


Figure 2.6: a) Kataura-plot showing the transition energies E_{ii} of any SWNT chirality plotted against its diameter. The data was calculated according to ref. 18. E_{ii}^M and E_{ii}^S denote the transition energies for metallic and semiconducting SWNTs, respectively. The gray (black) dots correspond to the S1(S2)-type semiconducting SWNTs, red dots belong to metallic SWNTs. The red line at an energy of 1.96 eV corresponds to the laser energy used for the optical excitation of SWNTs in this work. b) Illustration of the zone-folding approach for metallic (M), semiconducting S1 and S2 nanotubes. The Brillouin zone of metallic SWNT includes the K -point, they have no band gap. For semiconducting SWNTs, the K -point is always $|\mathbf{K}_1|/3$ away from the next cutting line. The minimum energy gap E_{11}^S is at the intersection of this nearest line with the $K \rightarrow \Gamma$ ($K \rightarrow M$) direction for S1(S2)-type tubes. Due to trigonal warping, the band gap energy differs for the two types.

ular polarization is strongly suppressed in SWNTs due to a depolarization effect [20–23]. The incident field generates opposite charges on either side of the nanotube circumference which then induce a reverse field that compensates the incident excitation. These cross-polarized transitions are therefore much weaker and do usually not contribute significantly to the nanotube excitation. They have been observed experimentally in cross-polarized PL excitation and absorption experiments and were found to be indeed much weaker than parallel transitions [24, 25]. Figure 2.7 shows examples for possible transitions and their polarization with respect to the nanotube.

For a more accurate description of the SWNT band structure beyond the zone-folding approximation, curvature effects need to be taken into account and the tight-binding calculations can be expanded to include 2^{nd} and 3^{rd} neighbor interactions. Strong curvature changes the overlap of π -orbitals and leads to a rehybridization of the σ - and π -states

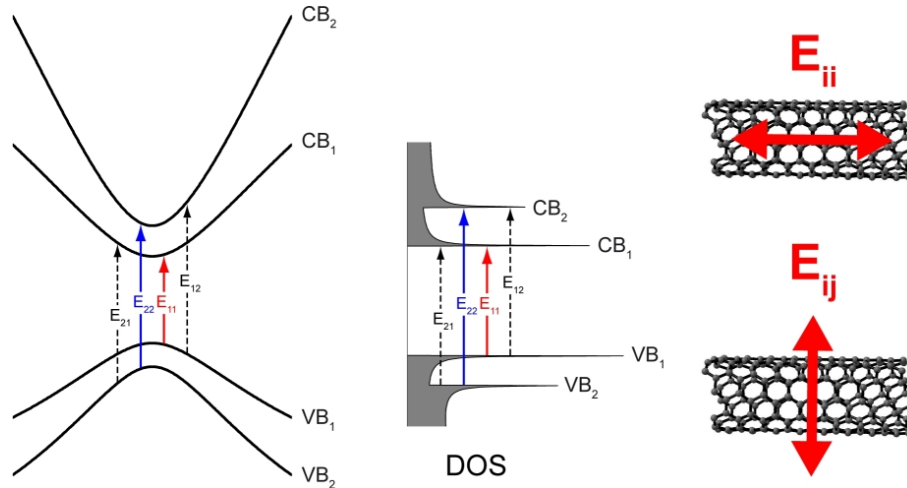


Figure 2.7: Transitions in semiconducting SWNTs in the free-particle picture. E_{ii} transitions between vHSs of the same index connect valence and conduction bands from the same line of the Brillouin zone. They are polarized along the nanotube axis since $\Delta k_{\perp} = 0$. E_{ij} transition between different lines of the Brillouin zone are polarized perpendicular to the nanotube, since $\Delta k_{\perp} \gg k_{\parallel}$. They are strongly suppressed due to a depolarization effect and do usually not contribute significantly to the SWNT excitation.

that are no longer orthogonal. However, for a basic understanding of the SWNT's optical properties, the discussed zone-folding approach should be sufficient.

What is much more important, is that the free-particle picture introduced so far does not hold for one-dimensional nanotubes. The optical excitations in SWNTs are strongly bound excitons, with an energy below the free-carrier band gap. The exciton picture is described in the following section.

2.2.4 Excitons

The Coulomb interaction between free charge carriers in metals and semiconductors is strongly suppressed with respect to free charge carriers in vacuum. The Coulomb force scales inversely with the dielectric constant ϵ of the surrounding medium, which can be very large. The dielectric constant expresses the polarizability of the medium, i.e. how strong charges respond to an electric field. The polarized medium compensates an external field, so that the internal field is much smaller. This is called dielectric screening. In 3D semiconductors with $\epsilon > 10$, the Coulomb interactions between the free charge carriers can be neglected at room temperature and the optical properties are dominated by free-particle excitations.

In SWNTs however, their one-dimensionality results in much stronger Coulomb interactions, mainly because of two factors. First, the reduced dimensionality increases the relative probability for two charge carriers to have a shorter separation. In 3D, the probability for

a specific distance r is proportional to the surface of a sphere and thus scales with a phase space factor r^2 . No such factor applies for the 1D case, which increases the relative importance of shorter separations and hence enhances the influence of Coulomb interactions [5].

Second, since most of the field lines between two charges are outside the 1D nanotube, the dielectric screening is reduced because the effective dielectric constant is dominated by the environment. Owing to these two reasons, the electron-electron-repulsion as well as the electron-hole-attraction are not negligible when discussing the excitations in SWNTs, and in 1D systems in general. The repulsive electron-electron interaction increases the energy of the free-particle band gap, which is known as band gap renormalization (BGR) [26]. Due to the attractive electron-hole interaction, the binding energy E_{bind} of excitons is enhanced and excitonic states with energies well below the free-particle band gap appear. Importantly, most of the transition oscillator strength is transferred from the free-particle to the lowest exciton state, which will therefore dominate the optical properties. This efficient transfer is again caused by the reduced dimensionality and the interatomic nature of the optical ($\pi - \pi^*$) transitions [27–29].

The importance of strongly bound excitons in carbon nanotubes has been first proposed by Tsuneya Ando [4] in 1997 and there have been many other theoretical investigations since [28, 30, 31]. The energy of the lowest optically allowed state gives rise to photoluminescence and is denoted as E_{PL} . Including the strong Coulomb interactions, it is given by

$$E_{PL} = E_{fp} + E_{BGR} - E_{bind} \quad (2.18)$$

where E_{fp} is the free-particle band gap energy neglecting charge carrier interactions as discussed in section 2.2.3. The exciton picture is illustrated in Fig. 2.8, where subfigure a shows the free-particle case and b is the realistic exciton picture for a SWNT in vacuum.

The band gap renormalization E_{BGR} is in the order of E_{fp} with hundreds of meV [30]. The exciton binding energy E_{bind} here refers to the lowest optically active exciton, which is the "bright" exciton. Theory predicts many more excitonic states that do not interact with light due to selection rules and are therefore called "dark" excitons. E_{bind} is also in the range of several hundreds of meV, but usually smaller than E_{BGR} [28, 30, 31]. The two shifts compensate to a large extent, so that E_{PL} is still close to E_{fp} . Also the scaling relation with respect to the diameter (Kataura-plot) is retained [30].

The exciton binding energy in SWNTs is orders of magnitude larger than in 3D semiconductors, where E_{bind} is only several meV and excitons are not stable at room temperature. In SWNTs however, the optical properties are dominated by the excitons, because most of the oscillator strength is transferred from the continuum transition E_{11}^∞ to the bright exciton E_{11}^{bright} . [28, 32].

Experimental verification of the exciton picture was reported in 2005 using two-photon photoluminescence [5, 33, 34]. By two-photon-excitation, a dark exciton near the continuum

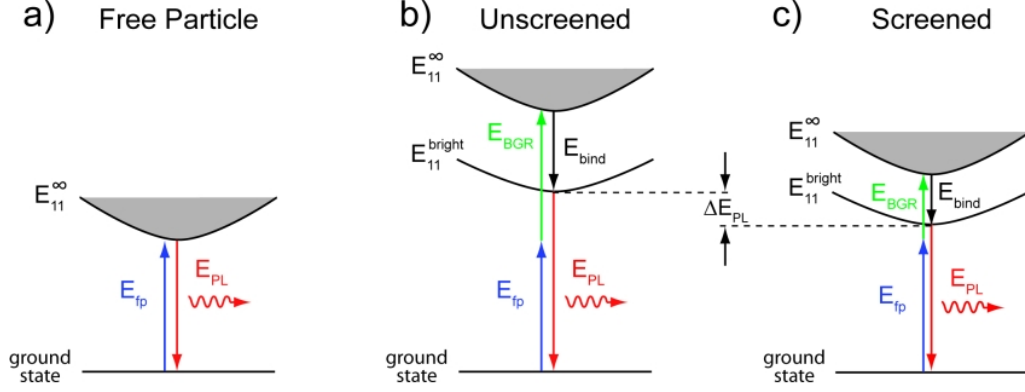


Figure 2.8: Schematic of the free-particle and excitonic states in SWNTs. a) Free-particle picture as discussed in section 2.2.3, neglecting free charge carrier Coulomb interactions. The photoluminescence energy E_{PL} corresponds to the free particle band gap E_{fp} . b) The strong Coulomb interactions in 1D SWNTs lead to a higher energy of the free-particle or continuum state E_{11}^{∞} and to strongly bound excitonic states E_{11}^{bright} below, with the binding energy E_{bind} . In the unscreened case, the surrounding of the SWNT has a dielectric constant $\epsilon = 1$. c) In the screened case, $\epsilon > 1$ leads to a smaller band gap renormalization E_{BGR} and smaller E_{bind} . The net change of the exciton energy is negative and leads to a red-shift of E_{PL} due to dielectric screening by the environment.

band gap can be excited, which decays to the lower bright exciton that finally emits photoluminescence. The two-photon excitation energy yielding the strongest PL is equal to the dark exciton energy, whereas the detected PL energy is the bright exciton energy. The measured energy differences for SWNTs with diameters of 0.7 – 0.9 nm were in the range of 300 meV and evidence the existence of different exciton states. From this, a binding energy E_{bind} of about 400 meV was estimated. Since then, the exciton picture is widely accepted. Although not explicitly discussed here, the higher transitions such as E_{22} , E_{33} and the E_{11} in metallic SWNTs have a strong excitonic character as well.

As discussed before, the Coulomb interactions in SWNTs are enhanced because most of the field lines between two interacting charges are outside the nanotube. If the dielectric constant ϵ of the surrounding medium changes, the Coulomb interaction is screened which reduces the band gap renormalization E_{BGR} and the binding energy E_{bind} . The scaling with ϵ is slightly different for both. E_{BGR} simply scales with ϵ^{-1} , whereas E_{bind} is predicted to scale with $\epsilon^{-1.2}$ for small ϵ [26] and with $\epsilon^{-1.4}$ for $\epsilon > 4$ [28]. The overall shift of E_{PL} is negative, because ΔE_{BGR} is slightly larger than ΔE_{bind} . This is illustrated in Fig. 2.8c.

The change of the exciton energy E_{PL} has been observed experimentally by comparing the optical properties of SWNTs in air with those in other environments, such as in aqueous solution and wrapped by a surfactant. The exciton energy is reduced by 10 – 55 meV due to environmental screening, strongly depending on the chiral angle, the diameter and the type of SWNT (S1 or S2) [35–37]. This shift is rather small since ΔE_{BGR} and ΔE_{bind} compensate each other. In ref. 37, the respective values at $\epsilon = 1$ are 730 meV and 580 meV. In

aqueous environment ($\varepsilon = 1.78$) they strongly decrease to 410 meV and 290 meV. However, the net PL red-shift is only 30 meV.

The excitons can be treated as neutral quasi-particles. Their size, i.e. the extension of their wave function along the SWNT axis, is 1 – 2 nm and they are delocalized along the circumference [28,31,38]. This means that the exciton wave function involves several hundred carbon atoms and they are therefore very sensitive to structural defects or doping in the nanotube. The exciton coherence length in SWNTs is rather small due to efficient exciton-phonon scattering and structural inhomogeneities. These factors lead to a fast dephasing on a time-scale below 200 fs at room temperature [39], which inhibits the coherent superposition of different exciton states along the SWNT. The resulting coherence length has been determined experimentally to around 10 nm [40], which justifies the treatment of excitons as independent, spatially defined particles in the case of low exciton densities.

In addition, excitons are highly mobile along the SWNT and their motion has been described as one-dimensional diffusion with a diffusion constant of about $0.4 \text{ cm}^2/\text{s}$ [41]. Experimental studies and a theoretical description of exciton mobility are the main part of this thesis and are discussed in detail in the chapters 5, 6 and 7.

2.3 Photoluminescence

Photoluminescence in semiconducting SWNTs arises from the radiative recombination of the bright E_{11} exciton after optical excitation of a higher state. The PL energy E_{PL} directly reflects the exciton energy, as can be seen in Fig. 2.8b and c. These energies are in the near infrared range starting at about 1.5 eV for the (5,4)-nanotube down to 0.5 eV for the very large tubes. Typical PL spectra for four different SWNTs chiralities are shown in Fig. 2.9. For individual SWNTs on substrates, the PL peaks can be as narrow as 20 meV, determined mainly by the fast exciton dephasing time [42], which would be about 70 fs in this case.

The strongest PL can be observed when the excitation energy is resonant to a higher transition as e.g. the E_{22} exciton, because then the absorption is maximized. Detection of PL upon direct E_{11} excitation is usually not possible due to the small Stokes-shift which makes it very difficult to suppress the exciting laser light in the experiment. When the E_{22} exciton is excited, it decays efficiently and very rapidly to the lower E_{11} exciton. This intersubband relaxation happens on a timescale of 40 fs and no direct radiative recombination, i.e. PL of the E_{22} state has been observed [43,44]. After the optical excitation to a higher exciton transition and fast intersubband relaxation to the E_{11} exciton, there are different pathways for the relaxation to the ground state. This is depicted in Fig. 2.10a.

First, the exciton can recombine radiatively and emit a photoluminescence photon. The radiative rate k_{rad} describing this process is expected to be in the range of $0.1 - 1 \text{ ns}^{-1}$ [45,

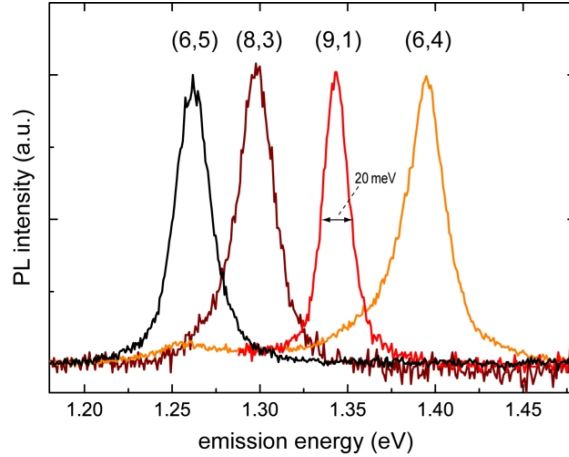


Figure 2.9: Typical photoluminescence spectra for single SWNTs on a glass substrate. The four different PL emission energies can be assigned to different chiralities (n,m) and correspond to the respective E_{11} exciton energy. The full-width-at-half-maximum for the PL peak of SWNTs on substrates is usually ≥ 20 meV.

46], which has been confirmed experimentally [40]. This rate is rather low which results from the ultrafast exciton dephasing and the respective short coherence length. Thereby, different parts of the SWNT do not emit coherently and each exciton gains its oscillator strength only from within the coherence length [40]. The radiative rate is proportional to the oscillator strength, which could be dramatically increased for coherently coupled emitters.

Second, the exciton can decay non-radiatively and the rate for this competing mechanism is k_{nr} , which was found to be dominating in SWNTs. The lifetime τ that can be measured in a time-resolved PL experiment is the inverse of the overall decay rate.

$$\tau = \frac{1}{k_{rad} + k_{nr}} \quad (2.19)$$

For SWNTs in solution and for individual SWNTs on substrates or immobilized in gels, the reported lifetimes are in the range of 5 – 50 ps at room temperature [42,47–49]. This means that k_{nr} is more than one order of magnitude larger than k_{rad} . The photoluminescence quantum yield QY is the fraction of absorbed photons that lead to an emitted photon. It can be written as

$$\text{QY} = \frac{k_{rad}}{k_{rad} + k_{nr}}. \quad (2.20)$$

Early reports of SWNT photoluminescence have reported a quantum yield of about 10^{-3} [50], recent advances in SWNT growth, separation and purification increased this number to the percent range [51–53]. The origin of the low QY is still under debate, but several mechanisms can be identified.

The first is energy transfer to other nanotubes. SWNTs have a strong tendency to form aggregates and bundles due to strong van der Waals interactions between the tubes. After the SWNT growth process, many different chiralities are present, including one third of

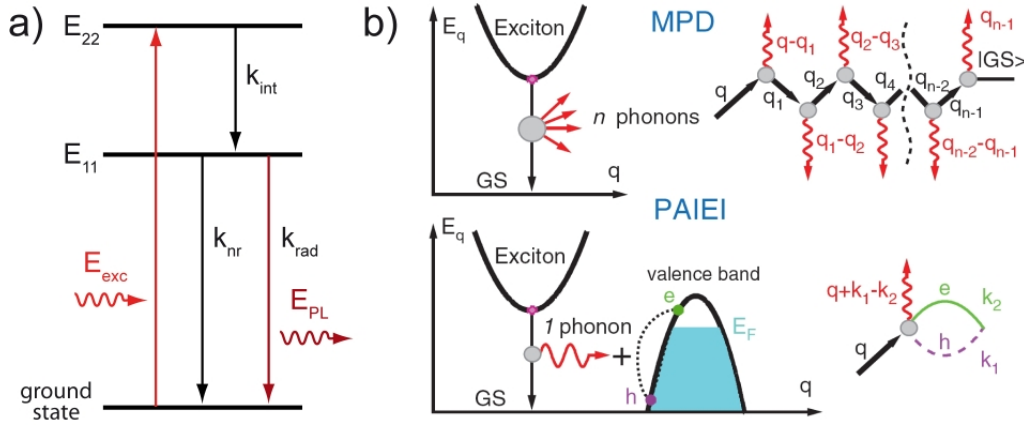


Figure 2.10: a) Schematic of the PL process showing the different decay pathways. After optical excitation into E_{22} , fast and efficient intersubband relaxation to the E_{11} state occurs, with a rate of $k_{int} \approx 1/40$ fs. The E_{11} exciton can decay radiatively, i.e. emit PL, or non-radiatively. In SWNTs, the radiative decay rate $k_{rad} \approx 0.1 - 1$ ns $^{-1}$ is much smaller than the non-radiative rate $k_{nr} \approx 0.01 - 1$ ps $^{-1}$ and the PL quantum yield is thus rather low. b) Two possible non-radiative decay mechanisms as proposed in ref. 54. These are multi-phonon decay (MPD) and phonon-assisted indirect exciton ionization (PAIEI).

metallic tubes. In SWNT bundles, efficient Förster type energy transfer between the tubes occurs [55]. If metallic SWNTs are present, energy transfer to those will quench the PL from the semiconducting SWNTs. Also energy transfer to semiconducting SWNTs with smaller band gaps that emit beyond the detectable energy strongly reduce the measured PL. Separation is the most important requirement to observe photoluminescence from SWNTs, which hindered its discovery until 2002 [50]. It is mainly achieved by wrapping the SWNTs with an amphiphilic surfactant or single-stranded DNA which make them soluble in water. The subsequent separation of residual small bundles from the nanotube solution using density gradient ultracentrifugation can further increase the effective QY significantly [52, 56]. Also polymer-wrapping and suspension in toluene has been very successfully applied with a recently reported QY of 20% [53].

The second mechanism is exciton quenching at defects and impurities in the SWNT. Early experiments showed that the PL is very sensitive to the pH of the SWNT solution. At low pH, the PL is strongly quenched which was attributed to a reversible protonation of the SWNT at adsorbed oxygen molecules on the sidewalls [57]. This creates a free hole on the nanotube which was believed to efficiently quench the excitons in a non-radiative Auger recombination [58, 59]. Due to the exciton mobility, only few holes are needed to quench the PL efficiently. However, according to Perebeinos *et al.* [54], this Auger recombination of exciton and hole is not possible due to missing angular momentum conservation. They propose a mechanism called phonon-assisted indirect exciton ionization (PAIEI) which is shown in Fig. 2.10b. This process is very efficient for doped SWNTs and involves the generation of a phonon to preserve momentum conservation. The exciton decays into a

phonon and an intraband electron-hole pair inside the valence band. P-doping lowers the Fermi energy and free states become available in the upper valence band, which allows the generation of the intraband e-h pair that subsequently recombines non-radiatively. Even for moderate p-doping as e.g. one hole per 5 nm, this process can account for the lifetimes in the range of tens of ps. Usually, SWNTs are unintentionally p-doped to some extent due to adsorbed oxygen or charges in the substrate. The process works accordingly for n-doping, which allows for the generation of an intraband e-h pair in the conduction band.

Perebeinos *et al.* [54] also propose multi-phonon decay (MPD) which is the decay of one exciton into n phonons as it is also shown in Fig. 2.10b. In an unperturbed SWNT, MPD is not very efficient with a rate of about 0.1 ns^{-1} . However, when the excitons are localized at impurities or defects, a phenomenon known from bulk semiconductors, the MPD rate is expected to increase by orders of magnitude to around 10 ns^{-1} due to stronger exciton-phonon coupling.

The experimentally observed lifetimes in the ps range [42, 47–49] are thus mainly ascribed to doping and heterogeneities that arise from the growth process, the purification steps and the separation procedure. A very recent publication from Hertel *et al.* [60] presents a consistent model, in which the short lifetimes and low quantum yields are ascribed to exciton quenching at distinct localized quenching sites only, neglecting any non-local non-radiative decay mechanisms such as MPD. The wide range of reported lifetimes and quantum yields can thus be explained in terms of a different quenching site density. However, it remains to be shown that defect-free SWNTs exhibit dramatically higher quantum yields.

At very high excitation densities, when several excitons are present at a time, exciton-exciton-annihilation becomes the most efficient decay mechanism, which limits the achievable exciton density [59, 61].

2.4 Raman scattering

Raman spectroscopy has since long played an important role for the study and characterization of graphitic materials. It is extensively used as a non-destructive tool to study their structural properties and provides information on e.g. nanotube chirality, doping and functionalization [6]. Especially the quantification of defect densities in SWNTs, graphene and graphite using Raman spectroscopy is very important.

Since the Raman process is very weak, this technique relies on the excitation with intense laser light, which is why it became particularly popular in the last two decades, when cheap and reliable laser sources were available. It is now one of the standard techniques for the characterization of crystalline materials, probing their vibrational properties. Nevertheless, the sensitivity is rather low and makes it difficult to record Raman spectra of single molecules or SWNTs. The easiest way to increase Raman scattering efficiencies is

resonant Raman scattering (RRS), described in the next section. Other approaches that can dramatically boost the sensitivity are surface-enhanced Raman scattering (SERS) and tip-enhanced Raman scattering (TERS), which will be discussed in Chapter 3.

Raman scattering is the inelastic scattering of an incident laser photon with one or more phonons. The case of a single interaction with one phonon is called first-order Raman scattering and is a three-step process as shown in Fig. 2.11a.

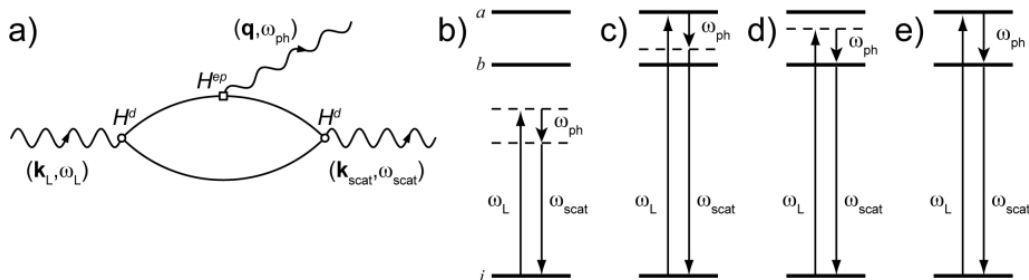


Figure 2.11: a) Feynman diagram of the first-order Raman process. An incoming laser photon with frequency ω_L excites an electron-hole pair. The electron is then scattered inelastically and emits a phonon with frequency ω_{ph} . The e-h pair finally recombines and emits a photon at frequency ω_{scat} . b - e) Different Raman scattering processes with respect to resonances with electronic states. Dashed lines are virtual states and solid lines indicate real electronic states. Depending on the incident laser frequency ω_L and the scattered light frequency $\omega_{scat} = \omega_L - \omega_{ph}$, the Raman process is non-resonant (b), has an incident (c) or scattered resonance (d) or it is double resonant (e).

An incoming laser photon with a wave vector \mathbf{k}_L and frequency ω_L excites an electron-hole pair. The electron is then scattered inelastically and emits a phonon with wave vector \mathbf{q} and frequency ω_{ph} . The e-h pair finally recombines and emits a photon with a wave vector \mathbf{k}_{scat} and frequency ω_{scat} . The energy difference of the scattered light with respect to the laser is $\hbar\omega_{ph}$ and denoted as Raman-Shift. It is usually expressed as the difference of wavenumbers $\lambda_L^{-1} - \lambda_{scat}^{-1}$ and measured in cm^{-1} . Energy and momentum must be conserved in the Raman process and thus

$$\omega_{scat} = \omega_L \mp \omega_{ph} \quad (2.21)$$

$$\mathbf{k}_{scat} = \mathbf{k}_L \mp \mathbf{q}. \quad (2.22)$$

The - and + signs corresponds to the Stokes- and Anti-Stokes process, where a phonon is either emitted or absorbed, respectively. The occupation of the excited phonon state with respect to the phonon ground state, i.e. the number of phonons available for the Anti-Stokes process, follows a Boltzmann distribution. In a first approximation, the probability for the Stokes and Anti-Stokes process, p_S and p_{AS} , are related by

$$\frac{p_S}{p_{AS}} \approx \exp\left(\frac{\hbar\omega_{ph}}{kT}\right) \quad (2.23)$$

with the Boltzmann constant k and the temperature T . At room temperature, the Stokes scattering is usually much stronger.

2.4.1 Resonance Raman scattering

If H^d is the Hamiltonian for the electron-photon or dipolar interaction and H^{ep} is the Hamiltonian for the electron-phonon interaction, the matrix element for the Raman scattering process \mathfrak{R} can be written as follows

$$\mathfrak{R} = \sum_{a,b} \frac{\langle \omega_{scat}, f, i | H^d | 0, f, b \rangle \langle 0, f, b | H^{ep} | 0, 0, a \rangle \langle 0, 0, a | H^d | \omega_L, 0, i \rangle}{(\hbar\omega_L - \Delta E_{ai} - i\gamma)(\hbar\omega_L - \hbar\omega_{ph} - \Delta E_{bi} - i\gamma)}. \quad (2.24)$$

Here, $|\omega_L, 0, i\rangle$ denotes the state with an incoming photon of frequency ω_L , the ground state of the phonon ("0" = no phonon excited) and the electronic ground state i . The initial and final state are both the electronic ground state i and the sum is over all possible intermediate electronic states a and b . The final excited phonon state is f . ΔE_{ai} and ΔE_{bi} are the energy differences between the electronic states a and b to the ground state i . γ is a broadening factor for the resonance to these electronic states. The Raman scattering intensity is proportional to $|\mathfrak{R}|^2$. The denominator in eq. 2.24 is minimized if $\hbar\omega_L = \Delta E_{ai}$ or $\hbar\omega_L - \hbar\omega_{ph} = \hbar\omega_{scat} = \Delta E_{bi}$ which leads to an enormous enhancement of the Raman intensity and is called resonant Raman scattering (RRS). These conditions are met when the incident or scattered photon energy (or both) match a real electronic transition in the system, as it is depicted in Figs. 2.11c-e. The probability for an incoming photon to be Raman scattered is usually very small, in the range of 10^{-6} . For RRS, this probability is enhanced by orders of magnitude, which allows for the detection of Raman scattering from individual SWNTs.

In case of semiconducting SWNTs, resonant Raman scattering occurs when the laser energy $\hbar\omega_L$ or the scattered photon energy $\hbar\omega_{scat}$ matches one of the electronic transition E_{ii} . For metallic SWNTs, the Raman scattering is in principle always resonant since there are states available also between the first pair of vHSs. Nevertheless, resonance to one of the E_{ii} transitions leads to the strongest RRS.

2.4.2 Raman scattering of graphene

The vibrational properties of SWNTs, which are probed by Raman scattering, are strongly related to those of graphene. They can be derived in a similar way as done for the electronic properties in section 2.2.1, using the vibrational properties of graphene and the zone-folding approach. This leads to very complex phonon band structures with dozens of distinct phonon branches, that are mostly not Raman active. The main Raman bands are similar to graphene and discussed in an analogue way. The most important Raman band which is unique for SWNTs is the radial breathing mode (RBM).

The phonon dispersion for graphene is shown in Fig. 2.12. The two inequivalent carbon atoms in the graphene unit cell with three degrees of freedom each, give rise to six phonon branches, namely the longitudinal optical (LO), the in-plane transverse optical (iTO or

TO), the out-of-plane transverse optical (oTO), the longitudinal acoustic (LA), the in-plane transverse acoustic (iTA) and the out-of-plane transverse acoustic (oTA) [62].

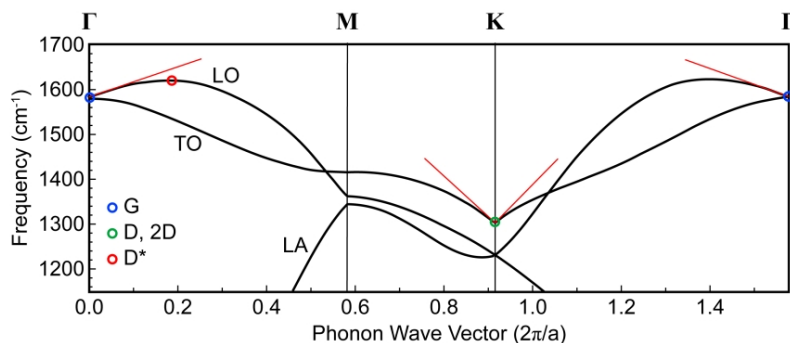


Figure 2.12: Phonon dispersion of graphene along $\Gamma \rightarrow M \rightarrow K \rightarrow \Gamma$ from ref. 63. The phonons corresponding to the main Raman bands are marked with colored circles. The red lines highlight the Kohn-anomalies, which is the anomalous slope of the dispersion near the high symmetry points K and Γ . TO, LO and LA denote the transverse optical, the longitudinal optical and the longitudinal acoustic phonon mode, respectively.

The LO and TO mode are responsible for the four prominent Raman bands in graphene, which are the G-, the D-, the 2D- and the D*-band. The strong electron-phonon coupling in graphene leads to an anomalous dispersion near the high symmetry points K and Γ , known as Kohn-anomaly. The phonon dispersion drops towards these points and has a slope, highlighted with the red lines in Fig. 2.12.

With respect to the first Brillouin zone of graphene, the exciting laser light and the scattered light have a very small wave vector. The laser wavelength is several hundred nanometers and thus orders of magnitude larger than the graphene lattice constant of 0.246 nm. Therefore, $|\mathbf{k}_L|$ can be considered as approximately zero. This is important regarding the required momentum conservation. In a first-order Raman process, only $\mathbf{q} \approx 0$ phonons can directly interact with light. The LO and TO mode are doubly degenerate at the Γ -point where $\mathbf{q} \approx 0$. This phonon gives rise to the G-band with a Raman-Shift of about 1580 cm^{-1} . The G-phonon corresponds to in-plane C=C stretching vibrations. This is the only first-order Raman band in defect-free graphene. The phonons with larger wave vector can only be excited in second-order processes, which can be classified as either intra-valley or inter-valley processes.

Fig. 2.13 shows the possible intra-valley processes in graphene. The electronic band structure is simplified by the linear bands near the K -point, where optical excitations take place. Intra-valley means, that the process happens within one of the dispersion cones. Since there are states available for every photon energy in the visible range, the processes are always resonant. The G-band scattering has either incident or scattered resonance.

The D*-band arises from the LO phonon branch at a wave vector that can connect the two sides of the dispersion cone. After excitation of the electron-hole pair, the electron emits

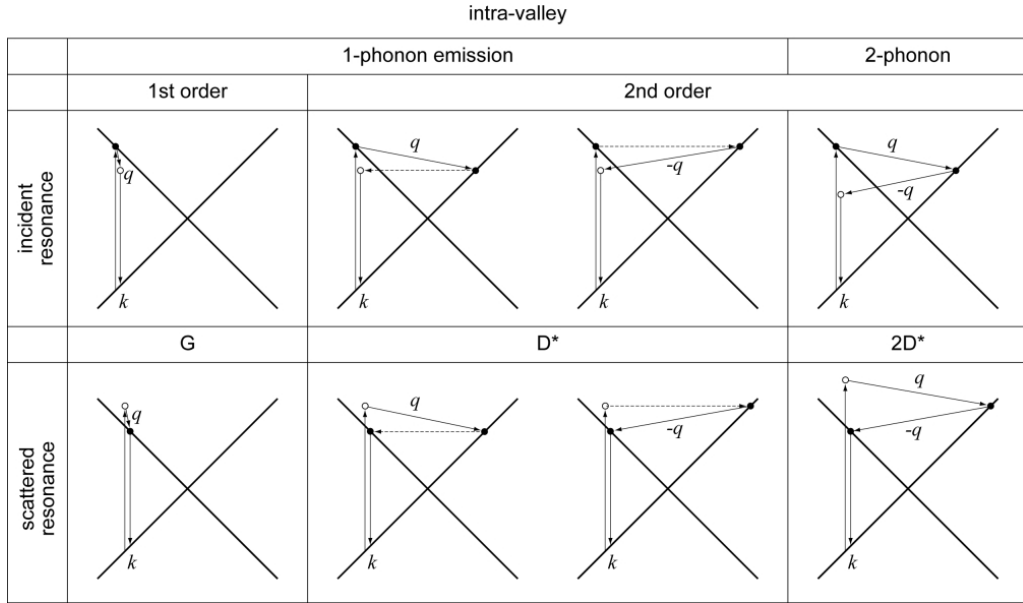


Figure 2.13: Intra-valley Raman scattering processes in graphene, that give rise to the G-, D*- and 2D*-band. The process takes place near one K -point. First-order processes involve one scattering event with a $\mathbf{q} \approx 0$ phonon, giving rise to the G-band. Second-order processes involve two scattering events. Emission of one phonon and elastic backscattering at a defect is possible, or two phonons with opposite momenta are emitted to preserve momentum conservation. The respective Raman-bands are the D* and 2D*.

this phonon and is scattered to the other side of the cone, where it cannot recombine with the hole due to momentum conservation. If defects are present, elastic scattering of the electron at the defect compensates the momentum mismatch and allows the process. The elastic defect scattering can also be the first step, followed by inelastic phonon emission. The process is double resonant, because the dispersion cone is touched on both sides. The D*-band requires defects and is forbidden for defect-free graphene. The Raman-Shift is about 1620 cm^{-1} .

The electron can also emit a second phonon of the same kind but with opposite momentum and will be scattered back to recombine with the hole. This two-phonon process does not need a defect and gives rise to the 2D*-band, an overtone of the D*-band at about 3240 cm^{-1} .

Fig. 2.14 shows the possible inter-valley processes in graphene. These are similar to the intra-valley processes, but they involve scattering between two inequivalent dispersion cones around K and K' , therefore termed inter-valley. All of them are double resonant processes. The phonon wave vector must connect the K - and K' -point, which is the same vector as from the Γ - to the K -point. This phonon can thus be found near the K -point in the phonon dispersion and is called the D-phonon. It corresponds to a breathing-like vibrational mode of the carbon six-rings. The one-phonon process is again only possible in the presence of defects and forbidden in defect-free graphene, except near the edge.

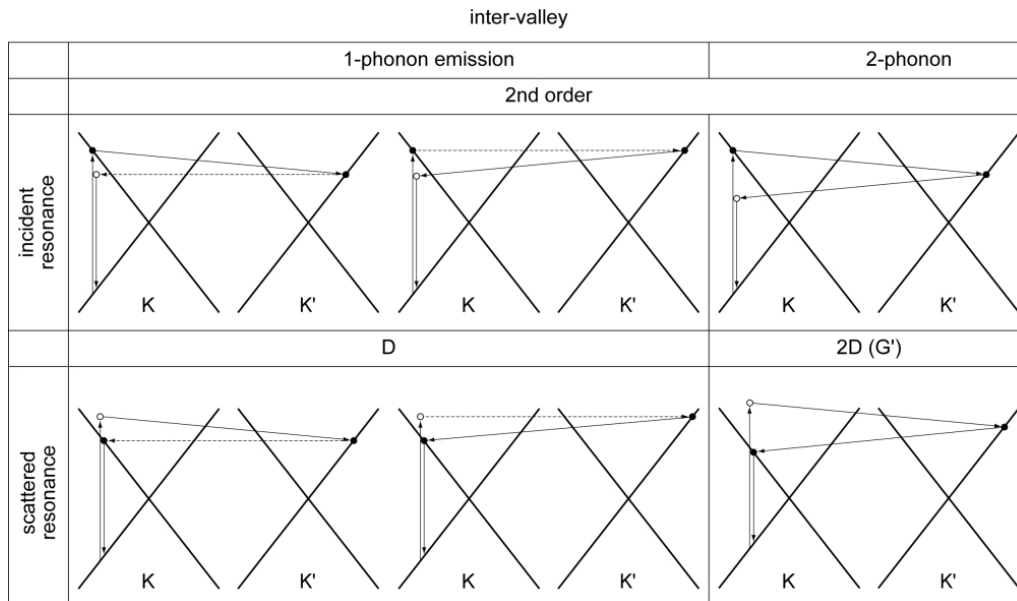


Figure 2.14: Intra-valley Raman scattering processes in graphene, that give rise to the D- and 2D-band. These processes connect two dispersion cones near the K - and K' -point and must be second-order processes. The emission of one phonon and elastic backscattering at a defect gives rise to the defect related D-band. The two-phonon process gives rise to the 2D-band, which is the strongest band in graphene.

There, the D-band scattering is also allowed, because the edge can be viewed as an extended one-dimensional defect [64]. The D-band appears at $1300\text{-}1350\text{ cm}^{-1}$, depending on the excitation wavelength. It is very sensitive to the defect density and used to quantify disorder. The two-phonon process gives rise to the 2D-band at around $2600\text{-}2700\text{ cm}^{-1}$, which is the strongest Raman band in graphene. A typical Raman spectrum for graphene is shown in Fig. 2.15. The spectrum was recorded near the edge of the graphene flake and therefore exhibits a weak D-band.

The Raman-Shift of the D- and 2D-band strongly depends on the exciting laser wavelength. This is due to the Kohn-anomaly, i.e. the slope near the K -point in the phonon dispersion (Fig. 2.12). For excitation with different laser energies, a slightly different phonon wave vector is required to touch the dispersion cone near the K' -point and fulfill the resonance conditions. Since the different wave vector is associated with a different phonon energy due to the pronounced Kohn-anomaly, the observed Raman-Shift changes with laser energy. The D-band dispersion is about $50\text{ cm}^{-1}/\text{eV}$ and for the 2D-band it is the double value of about $100\text{ cm}^{-1}/\text{eV}$ [63].

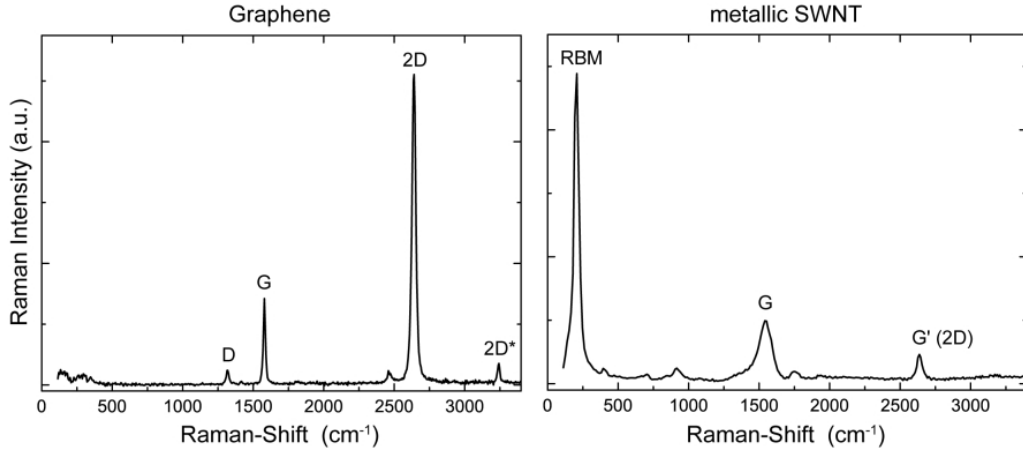


Figure 2.15: Typical Raman spectra for graphene and a metallic SWNT. The graphene spectrum was measured near the edge of a graphene flake, which is why some D-band scattering is visible. The metallic SWNT shows a very strong RBM-band, which indicates that the excitation energy is very close to E_{11}^M and thus resonant. The G-band splitting is not resolved, the G^+ -peak is overlaid by the much stronger and broader G^- -peak. A D-band is not detectable, showing that this SWNT is nearly defect-free.

2.4.3 Raman scattering of SWNTs

In the following, the four main Raman bands of SWNTs are discussed. Apart from the radial breathing mode which is unique to SWNTs, the bands are quite similar to graphene. There are many more modes discussed in literature, e.g. so called intermediate-frequency-modes that involve scattering with acoustic phonons [62]. These are not discussed here, since they are not studied in this work. A typical Raman spectrum for a metallic SWNT is shown in Fig. 2.15.

RBM-band

The radial breathing mode (RBM) is an out-of-plane vibration of the SWNT shell, i.e. an oscillation of the diameter. The corresponding phonon is near the Γ -point ($\mathbf{q} \approx 0$) and has a rather small energy. As the G-phonon, it can be excited in a first-order Raman process and is thus always allowed. The RBM-band intensity is very sensitive to the resonance Raman effect, since its energy is so low. The energy of laser photon and scattered phonon are close and can both be in resonance with the same transition. For off-resonance condition, the RBM-band is barely detectable, whereas it can be the most intense Raman band if the resonance is met (see Fig. 2.15). Its frequency is strongly diameter dependent following the relation

$$\omega_{RBM}(\text{cm}^{-1}) = \frac{227}{d_t(\text{nm})} \sqrt{1 - C_e d_t^2} \quad (2.25)$$

where C_e is a constant accounting for environmental interactions [65]. For SWNTs in solution, C_e has a value of 0.056 nm^{-2} . The RBM frequency is widely used for (n,m) as-

signment, because it allows the precise determination of the diameter. If this is combined with a RBM excitation spectrum, where the RBM intensity is measured while the laser energy is tuned through the resonance window, (n,m) can be rather unambiguously identified. Since the RBM intensity is very sensitive to the resonance condition, RBM excitation spectra display the position and the width of the resonant transition E_{ii} very clearly. This is used to map the E_{ii} transitions of metallic and semiconducting SWNTs from which an experimental Kataura-plot can be constructed [18].

G-band

The degeneracy of the TO and LO phonon at $\mathbf{q} = 0$ in graphene is lost in SWNTs due to symmetry breaking induced by the curvature. The LO phonon in SWNTs corresponds to C=C stretching vibrations along the nanotube axis, whereas the TO phonon describes vibrations along the circumference. The energy of these two modes is different and the G-band is therefore split into two components, usually referred to as G^+ and G^- for the higher and lower frequency component, respectively. The frequency and lineshape for both components is rather different for semiconducting and metallic SWNTs.

In semiconducting SWNTs, both components G^+ and G^- have a single Lorentzian lineshape with a width below 10 cm^{-1} . The G^+ peak corresponds to the LO phonon and thus to vibrations along the nanotube axis. Its frequency is about 1590 cm^{-1} and does not significantly depend on the diameter [66]. The lower frequency G^- component corresponds to the TO phonon with vibrations along the circumference. The force constants along this direction are slightly smaller, i.e. the SWNT is less stiff along the circumference. The downshift of the G^- component is diameter dependent following the relation $\omega_{G^-} = \omega_{G^+} - C/d_t^2$ with $C = 47.7 \text{ cm}^{-1}\text{nm}^2$ [67].

In metallic SWNTs, the Raman peak corresponding to the LO phonon behaves very different. Due to very strong electron-phonon coupling of this mode, the Raman peak is strongly shifted to lower frequencies and it is very broad. Furthermore it exhibits a Breit-Wigner-Fano lineshape and is therefore strongly asymmetric. It is shifted below the TO peak and the assignment of G^+ and G^- to TO and LO is opposite to the semiconducting SWNTs. The width is in the range of $40 - 80 \text{ cm}^{-1}$ [68] and the position follows the relation $\omega_{G^-} = 1590 \text{ cm}^{-1} - C/d_t^2$ with $C = 79.5 \text{ cm}^{-1}\text{nm}^2$ [67]. The Raman peak corresponding to the TO phonon, which is the G^+ component here, behaves similar as for semiconducting SWNTs, with a narrow lineshape and weaker diameter dependence of the position ($C = 12 \text{ cm}^{-1}\text{nm}^2$ [66]). However, it is often weak and hidden in the broad G^- component (see Fig. 2.15). Interestingly, the correct assignment of both components in metallic SWNTs has only recently been verified and published [69].

D-band

The D-band in SWNTs arises from a similar double resonance process as in graphene. Defect scattering is needed to preserve momentum conservation and the D-band intensity can thus be used as a measure for the defect concentration. It is for example correlated to the degree of covalent functionalization of the nanotube sidewall [70]. The position of the D-band is slightly diameter dependent and the dispersion with respect to the laser energy was found to depend on the chirality, leading to a somewhat different dispersion slope between 40 and 60 cm⁻¹/eV [2]. For an excitation with a green or red laser, it is usually found at around 1350 cm⁻¹. The D-band scattering resulting from defects in metallic SWNTs is discussed in more detail in chapter 9.

G'-band (2D-band)

The 2D-band in SWNTs is historically named G'-band. As for graphene, it arises from a two-photon double resonant Raman process. Its frequency dispersion with respect to the exciting laser energy has some diameter and chirality dependence, similar to the D-band. It can be composed of two sub-peaks in SWNTs, depending on the chirality (n,m) [62]. This can happen when two different higher E_{ii} transitions, e.g. E_{33} and E_{44} , are involved in the double resonant process. Then one peak could originate from an incident resonance on E_{44} and the other could have a scattered resonance on E_{33} . Both processes require slightly different phonon wave vectors, connected to a different phonon frequency due to the strong Kohn-anomaly. This is only possible if $E_{44} - E_{33} \approx 2\hbar\omega_D \approx 0.33$ eV.

Recently it could be demonstrated, that p- and n-type doping both lead to a second component of the G'-peak, that has a higher or lower frequency, respectively. It was attributed to electron and phonon renormalization near charged defects [71, 72]. The G'-band can therefore be used to identify and quantify doping in SWNTs.

3 High-resolution optical microscopy

Optical microscopy is one of the most widespread techniques for imaging and characterization of matter on small scales and is widely used in physics, chemistry, biology, medicine and materials science. It has a long history spanning centuries from the early microscopes of Galileo Galilei and Christiaan Huygens to the state-of-the-art STED microscopes of nowadays. In combination with spectroscopy of the detected light, optical microscopy provides insight into the chemical composition and the structural properties of the studied sample. In other words, the color of an object contains a wide range of information.

However, the diffraction of light sets a serious limit to the achievable spatial resolution. If the distance between two tiny objects is smaller than roughly half the wavelength of the light, they can not be resolved individually and appear as a single object. For wavelengths in the visible range corresponding to molecular electronic transitions in many interesting systems, the resolution is thus limited to a few hundred nanometers. The applicability of classical optical microscopy for the study of nanoscale systems as e.g. modern microelectronic devices or functional units in biology, is therefore limited.

The diffraction limit arises from the loss of spatial information during the propagation of light to the detector. In the near-field of the sample at sub-wavelength distance, this information is still available. Near-field microscopy exploits this fact by exciting and/or probing the sample in the near-field. In particular tip-enhanced near-field optical microscopy (TENOM) that is employed in this work, provides not only nanoscale spatial resolution but also high sensitivity down to the single molecule level.

This chapter starts with the theoretical background of light propagation and the associated resolution limit of far-field microscopy. Afterwards, different concepts to overcome the diffraction limit by exploiting the near-field are briefly discussed. The third section then provides a detailed description of tip-enhanced near-field optical microscopy from the physical concept to its experimental realization. Finally, the last section gives a short overview of far-field concepts that circumvent the diffraction limit and discusses these opposing approaches with respect to TENOM.

3.1 Propagation of light and the diffraction limit

3.1.1 Angular spectrum representation

The angular spectrum representation is a mathematical technique for the description of optical fields. Herein the optical fields are represented as a superposition of plane waves and evanescent waves, which are both fundamental solutions of Maxwell's equations. The angular spectrum representation is an efficient method for the description of light focusing which is the basis of optical microscopy. It also gives a very descriptive explanation for the diffraction limit. This section is based on the description in ref. 8.

The angular spectrum representation is the series expansion of an arbitrary field in terms of plane waves with variable amplitudes and wave vectors. Let $\mathbf{E}(x, y, z)$ be the field emanating from a scattering experiment as depicted schematically in Fig. 3.1.

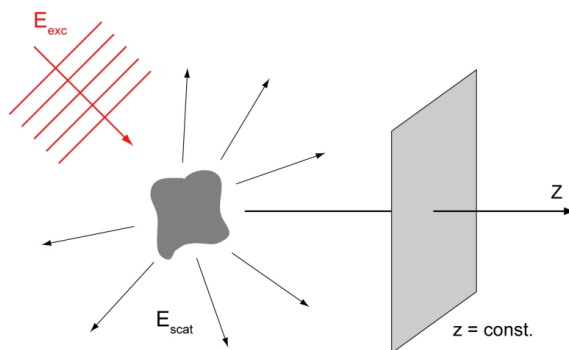


Figure 3.1: Schematic of the angular spectrum representation, where the fields that emanate e.g. from a scattering experiment are evaluated in planes perpendicular to an arbitrarily chosen axis z . The field $\mathbf{E}(x, y, z)$ is the sum of an exciting field \mathbf{E}_{exc} and the scattered field \mathbf{E}_{scat} .

Here, \mathbf{E} is the sum of an exciting field \mathbf{E}_{exc} and the scattered field \mathbf{E}_{scat} . In this picture, an arbitrary axis z is defined and the field \mathbf{E} is evaluated in a perpendicular plane ($z = \text{const.}$), where its Fourier transform $\hat{\mathbf{E}}$ is given by

$$\hat{\mathbf{E}}(k_x, k_y, z) = \frac{1}{4\pi^2} \iint_{-\infty}^{\infty} \mathbf{E}(x, y, z) e^{-i(k_x x + k_y y)} dx dy. \quad (3.1)$$

Here, x, y are the Cartesian coordinates in the plane and k_x, k_y are the corresponding spatial frequencies or reciprocal coordinates. The inverse Fourier transform is given by

$$\mathbf{E}(x, y, z) = \iint_{-\infty}^{\infty} \hat{\mathbf{E}}(k_x, k_y, z) e^{i(k_x x + k_y y)} dk_x dk_y. \quad (3.2)$$

If the medium is assumed to be homogeneous, linear and source-free, a time-harmonic optical field at a frequency ω has to fulfill the vector Helmholtz equation

$$(\nabla^2 + k^2)\mathbf{E}(x, y, z) = 0 \quad (3.3)$$

where $k = \omega n/c = 2\pi n/\lambda$ is the magnitude of the wave vector with the refractive index $n = \sqrt{\varepsilon\mu}$. The time-dependent field $\mathbf{E}(x, y, z, t)$ is given as $\text{Re}\{\mathbf{E}(x, y, z)e^{i\omega t}\}$. By defining

$$k_z \equiv \sqrt{k^2 - k_x^2 - k_y^2} \quad (3.4)$$

and inserting the Fourier representation of \mathbf{E} (eq. 3.2) into the Helmholtz equation, it can be shown that the Fourier spectrum $\hat{\mathbf{E}}$ evolves along the z-axis as

$$\hat{\mathbf{E}}(k_x, k_y, z) = \hat{\mathbf{E}}(k_x, k_y, 0)e^{\pm ik_z z}. \quad (3.5)$$

The \pm sign corresponds to waves traveling in forward and backward direction, respectively. Equation 3.5 means that the Fourier spectrum of \mathbf{E} in an image plane at $z = \text{const.} > 0$ can be derived from the spectrum in the object plane at $z = 0$ by multiplying with the factor $\exp(ik_z z)$, which is called the propagator factor in reciprocal space. Then, eq. 3.2 can be written as

$$\mathbf{E}(x, y, z) = \iint_{-\infty}^{\infty} \hat{\mathbf{E}}(k_x, k_y, 0)e^{i(k_x x + k_y y \pm k_z z)} dk_x dk_y \quad (3.6)$$

which is the angular spectrum representation of \mathbf{E} . For a purely dielectric medium, the refractive index n is a real and positive number. Then k_z is either real or imaginary, depending on the spatial frequencies k_x and k_y .

For $k_x^2 + k_y^2 \leq k^2$, k_z is real and the propagator factor $\exp(ik_z z)$ is a pure phase factor. These waves are propagating plane waves and represent the *far-field*.

For $k_x^2 + k_y^2 > k^2$ however, k_z becomes purely imaginary and the propagator factor is $\exp(-|k_z|z)$, which leads to a rapid exponential decay of these field components. The decaying waves are called *evanescent* and represent the *near-field*, which only exists in close proximity to the source.

The angular spectrum representation is the superposition of plane waves and evanescent waves, i.e. the sum of far-field and near-field components. The characteristics of both contributions can be summarized as follows.

$$\begin{array}{lll} \text{plane waves:} & k_x^2 + k_y^2 \leq k^2 & \text{propagator: } \exp(ik_z z) \\ \text{evanescent waves:} & k_x^2 + k_y^2 > k^2 & \text{propagator: } \exp(-|k_z|z) \end{array} \quad (3.7)$$

The angle θ under which the plane waves propagate with respect to the z-direction can be calculated as

$$\tan \theta = \frac{\sqrt{k_x^2 + k_y^2}}{k_z} \quad \text{or} \quad \sin \theta = \frac{\sqrt{k_x^2 + k_y^2}}{k}. \quad (3.8)$$

A plane wave traveling in z-direction with $\theta = 0^\circ$ and $k_x = k_y = 0$ has no oscillations in the transverse plane and carries no spatial information. In the other extreme, a plane wave with $\theta \rightarrow 90^\circ$ and $k_x^2 + k_y^2 = k^2$ has the highest spatial oscillations and carries the maximum of spatial information that can propagate. Evanescent waves with $k_x^2 + k_y^2 > k^2$

contain even higher spatial frequencies, but these waves decay and do not propagate. The higher the spatial frequencies are, the faster is the decay.

The propagation of the fields from nanoscale point sources is schematically depicted in Fig. 3.2. It shows the evolution of the optical field distribution emanating from a single point source (Fig. 3.2a) and four point sources spaced by 20 nm (Fig. 3.2b), together with the respective Fourier spectra.

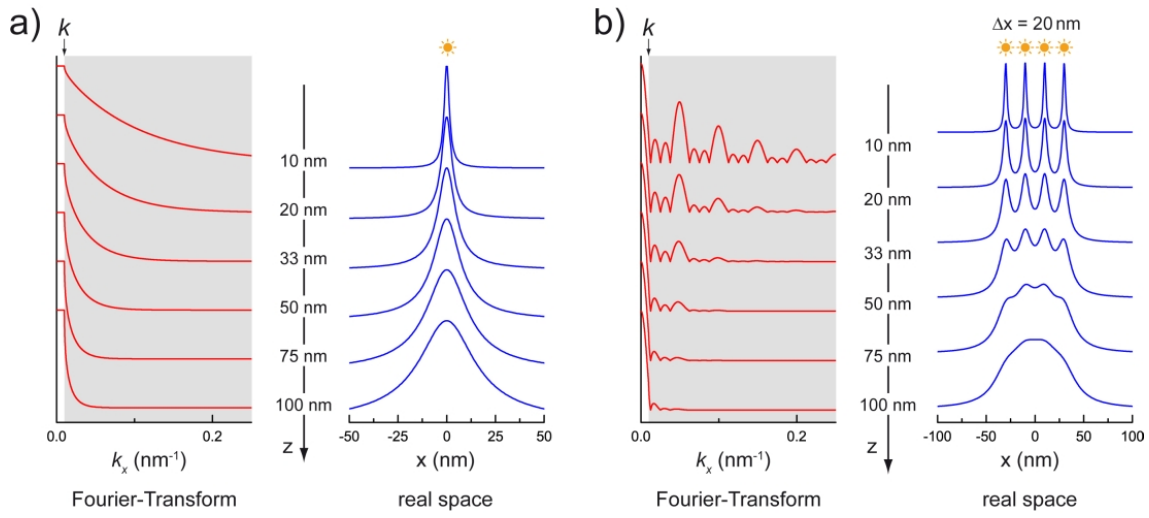


Figure 3.2: Schematic of the loss of spatial information upon propagation of optical fields from nanoscale point sources. Shown are the Fourier spectrum and the field distribution along the x -direction in real space for different distances z from the sources. The source is a single emitter in a) and four emitters separated by 20 nm in b). k_y is set to zero for simplicity. Contributions with $k_x > k$ in the Fourier spectrum (gray shaded parts) decay rapidly with increasing distance z . The field distributions broaden and make the four point sources in b) undistinguishable already at a distance of 75 – 100 nm. For the calculations, a refractive index $n = 1$ and $k = 2\pi n/\lambda$ with $\lambda = 633$ nm was used.

With increasing distance z from the source, the evanescent components in the Fourier spectra vanish rapidly which broadens the field distribution along the x -axis in real space. This broadening is the effect of diffraction. One can immediately see, that the spatial information about closely spaced nanoscale objects is still available within the near-field at distances of 10 – 30 nm. The spatial frequencies with $k_x > k$ are contained in the Fourier spectrum and the field distribution shows four different sources. However, already at a distance of 75 – 100 nm, the four point sources spaced equally by 20 nm are indistinguishable. This points out one route to break the diffraction limit: if the field distribution is detected in the near-field at a distance of few nanometers, nanoscale imaging with visible wavelengths is possible. Such approaches are introduced in section 3.2.

3.1.2 The resolution limit

The limited resolution in optical microscopy arises from the fact that the fields are detected in the far-field at $z \rightarrow \infty$. The evanescent field components are lost and only the propagating plane waves can be collected. Moreover, it is not feasible to collect plane waves at angles θ approaching 90° because the aperture and distance of the microscope objective set a limit. If θ_{max} is the maximum angle with respect to the z-axis under which a wave can propagate and still be detected, then the numerical aperture of the imaging lens or objective is defined as

$$\text{NA} = n \sin \theta \quad (3.9)$$

where n is the refractive index of the medium between source and lens. In the following, a single dipole in the object plane that is emitting light at a wavelength of λ is considered. The light is then collected by an objective and imaged onto the image plane. The dipole orientation is along the x-axis. The image that is formed in the image plane is the point-spread-function (PSF) of the system. Due to the limited spatial bandwidth of the far-field in the image plane, the field distribution is much broader than in the object plane (see also Fig. 3.2a), i.e. the PSF has a considerable width. In the paraxial limit, for $\theta \ll 90^\circ$, the PSF has the following form (evaluated along the x-direction):

$$I(x) \propto \left(2 \frac{J_1(p)}{p}\right)^2 \quad \text{with} \quad p = \frac{2\pi \text{NA}}{M\lambda} x \quad (3.10)$$

which is an Airy function. Although this function is only valid in the paraxial limit, it is a very good approximation also for high NA objectives with only minimal deviations. The width Δx of the Airy function is defined as the distance from the maximum to the first minimum.

$$\Delta x = 0.61 \frac{M\lambda}{\text{NA}} \quad (3.11)$$

where M is the magnification. The well-established resolution limit formulated by Ernst Abbe states that two point sources can be resolved when their PSFs are separated by more than the width Δx . That means that the maximum of one Airy function falls onto the first minimum of the other. If two point sources are spaced by a distance of Δr , their PSFs are displaced by $M\Delta r$ and they they can be resolved if

$$\Delta r \geq 0.61 \frac{\lambda}{\text{NA}}. \quad (3.12)$$

This resolution limit is illustrated in Fig. 3.3.

The definition of Abbe is somewhat arbitrary because the overlapping PSFs can still be distinguished and the orientation of the two dipoles is fixed as parallel. Nevertheless, it is a good estimation of what can be achieved with a diffraction limited optical microscope. A similar resolution limit for the z-direction, i.e. point sources in different object planes separated in z-direction by Δr_z is given by

$$\Delta r_z \geq 2 \frac{n\lambda}{\text{NA}^2}. \quad (3.13)$$

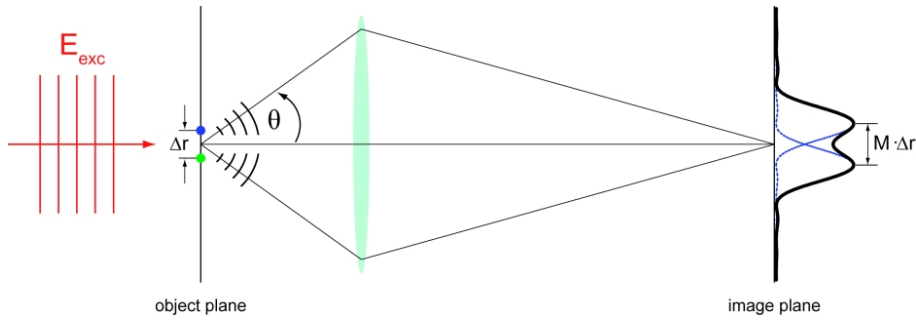


Figure 3.3: Illustration of the resolution limit in optical microscopy. The field of two point dipoles in the object plane spaced by Δr is collected by a lens and imaged onto the image plane. The image of each point dipole is the point-spread-function, which is an Airy function with a finite width due to diffraction (blue curves). If M is the magnification of the system, the two PSFs overlap with a distance of $M \cdot \Delta r$ (solid black curve). The two PSFs and thus the two dipoles can only be distinguished, i.e. resolved, when $\Delta r > 0.61 \cdot \lambda/\text{NA}$.

This value is much larger and depends quadratically on the NA. It results from the large extension of the point-spread-function in z -direction. For 3D imaging of thick specimen such as biological cells, this is a serious drawback.

3.2 Near-field concepts

The central idea behind near-field microscopy is the interaction with the sample in its near-field, where high spatial frequencies beyond the diffraction limit are available. Since the detection of light with photo-diodes or a CCD-camera is necessarily in the far-field, the simplest approach to attain sub-wavelength resolution is to avoid the overlap of the PSFs. This can be achieved by selective excitation of only one emitter at a time, using a nanoscale near-field light source.

Aperture SNOM

Already in 1928, E. H. Synge proposed the use of a sub-wavelength aperture close to the sample as a near-field nanoscale light source. This approach is illustrated in Fig. 3.4a. An opaque metal screen with a tiny hole of about 50 – 100 nm is brought close to the sample, where only a small area behind this hole will be illuminated. As the field behind the aperture is confined to the aperture size which is much smaller than the wavelength, it contains high spatial frequencies $k_x, k_y > k$ and is therefore evanescent and a near-field. Owing to its rapid decay with increasing distance, the aperture must be close to the sample, within several tens of nanometers.

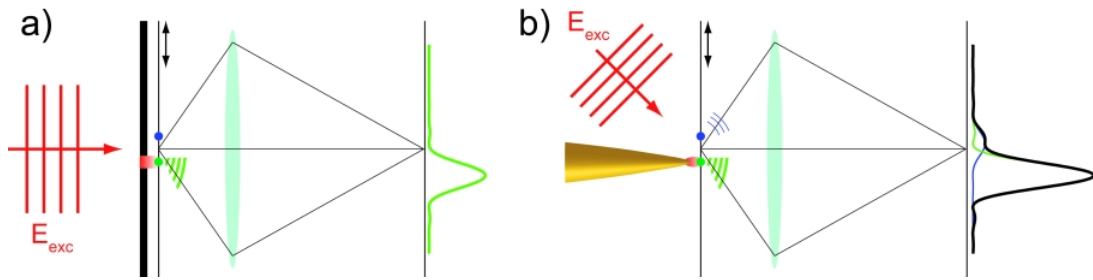


Figure 3.4: Different concepts of scanning near-field optical microscopy (SNOM). a) Aperture based SNOM based on the idea of Syngde, proposed already in 1928. The sample is illuminated through a tiny aperture with a diameter much smaller than the wavelength, which allows the selective excitation of only one emitter. The sample is then raster scanned under the aperture to form an image. b) Apertureless SNOM using the enhanced and confined near-fields at an illuminated metal tip for selective excitation of the sample. Though both emitters are still excited by the far-field, the emitter underneath the tip is excited much stronger by the enhanced near-field and its signal dominates the detected signal. Due to the field enhancement at the metal tip, this approach provides a much higher sensitivity compared to the aperture approach.

An image is formed by raster scanning the sample underneath the aperture and detecting the optical signal, which originates from an aperture-sized area, at each position. This technique was named scanning near-field optical microscopy (SNOM). The resolution that can be achieved is then only limited by the aperture size. The experimental realization of this technique requires the precise control of the aperture-sample distance and the sample position, which was possible in the 1980's using accurate piezo-positioners. The aperture is commonly realized by a glass fiber, tapered at the end and coated with a metal film. At the tip apex, the metal coating is opened to form the aperture. The illuminating laser light is sent through the fiber and a tiny fraction is transmitted by the aperture and illuminates the sample. Early demonstrations of sub-wavelength resolution with visible wavelengths were reported by Pohl *et al.* and Lewis *et al.* in 1984 in 1986 [9,73,74]. They performed line scans across grating structures with nanoscale periodicity. Further developments optimized the aperture probes with respect to light transmission and improved the probe-sample-distance control by using shear-force detection as a measure for the distance [75,76]. These improvements facilitated 2D scan images with nanoscale resolution down to 12 nm, showing single fluorescently labeled beads and cell tissue [10].

The concept can also be reversed by using the aperture probe as a near-field detector for a far-field illuminated sample. This is widely used for imaging of near-field distributions and can be combined with interferometric detection to image also the phase of the near-fields with nanoscale resolution. Thereby, surface plasmons traveling in plasmonic crystals could be visualized [11].

The main drawback of aperture SNOM is the very low throughput of light at the nanoscale aperture. It is in the range of 10^{-4} and far below for apertures smaller than 100 nm. This

limits the resolution to about 50 nm in a practical experiment. It also strongly hinders the detection of inherently weak signals such as Raman scattering. In general, spectroscopy is difficult when using aperture SNOM.

Apertureless SNOM

An alternative way to realize a nanoscale light source without the use of an aperture is to explore the strong local near-fields at metallic nanostructures. In the simplest case, a spherical metallic nanoparticle is illuminated by a laser field. The optical field can induce a collective oscillation of the electrons inside the particle, known as plasmon. The near-fields associated to this plasmon are highly confined and much stronger than the incident field, which is called field enhancement. The distinct polarizability of each metal, expressed in its wavelength dependent refractive index, and the particle shape give rise to plasmon resonances for specific wavelengths of the incident light. If the resonance is met, the plasmon excitation is very efficient and the field enhancement is very high. For gold nanoparticles, these resonances occur in the green to red visible range. The particle can be viewed as an optical antenna which is driven by the far-field and concentrates the excitation energy into a small near-field volume. Such a metallic nanostructure can be used for nanoscale optical imaging, when its highly confined near-field is scanned across the sample and selectively excites a sub-wavelength area. This approach was first proposed in 1985 by John Wessel and is known as apertureless or field-enhanced SNOM [12].

The principle is illustrated in Fig. 3.4b with a sharp gold tip as the optical antenna. The strong near-field at the tip end selectively increases the optical excitation of one emitter which then dominates the detected signal. In the experimental realization, usually the sample is scanned and the tip maintains its position with respect to the exciting laser.

Sharp metallic tips made of silver or gold are often used as probes for apertureless SNOM. The field enhancement of elongated metallic nanostructures can be much larger than for spheres because the sharp tip apex represents a spatial singularity where the field is concentrated even further, similar to the "lightning-rod-effect". The technique is known as tip-enhanced near-field optical microscopy (TENOM) and will be discussed in detail in section 3.3.

The main advantage of TENOM compared to aperture SNOM is its high sensitivity. Instead of blocking most of the excitation or detection, the signal is locally enhanced by orders of magnitude. As the antenna process is reciprocal, both excitation and detection are enhanced. This makes it possible to detect Raman spectra from single molecules [77]. The spatial resolution is given by the tip radius which can be as small as 10 nm.

A disadvantage is the far-field illumination of the sample outside the tip-enhanced area. The detected signal is the sum of the tip-enhanced signal from an area A_{tip} and the far-field background from the illuminated sample area A_{ff} . The latter is at least 100 times larger,

which means that the tip has to enhance the local signal by 100 in order to detect the same intensity of near-field and far-field contributions. Much higher signal enhancement is needed to have a dominating near-field contribution in the detection and negligible far-field background. For the imaging of 1D structures such as SWNTs, this problem is less severe since a length ratio and not an area ratio must be considered. Even higher contrast is found for sufficiently spaced single objects such as fluorescent molecules, which would be the 0D case.

A very interesting approach is the combination of tip-enhancement and an aperture SNOM probe. For this technique, called tip-on-aperture (TOA), a small metallic tip is placed next to the aperture of a SNOM probe [78–80]. The tip is excited through the aperture, which eliminates a far-field excitation and thus strongly suppresses the background. The low throughput of the aperture is compensated by the tip-enhancement, thus avoiding the main drawback of aperture SNOM. The tip-on-aperture approach combines the best of both techniques, but requires rather complex preparation of probes.

A further technique which is closely related to TENOM is scattering SNOM, which is mostly used in the infrared range. It does not rely on field enhancement to distinguish the signal from different emitters. The tip is used as a scatterer which is brought close to the sample and scatters the local near-fields into the detected far-field. This means the tip also acts as an antenna, converting the evanescent near-field into propagating far-field. Due to much weaker field enhancement and a very strong scattering background, the near-field signal can not easily be discriminated from the background. The background can be suppressed by oscillating the tip-sample distance at a frequency Ω and detecting only the signal variations at a higher harmonics $n\Omega$ by means of a lock-in amplifier. The constant background is thus rejected and the near-field detection can furthermore be phase-sensitive. This technique can be used to map the local complex refractive index, associated e.g. to carrier densities and mobilities in microelectronic devices [81–84].

3.3 Tip-enhanced near-field optical microscopy

The technique employed in this work for high-resolution optical imaging is tip-enhanced near-field optical microscopy. As mentioned before, it is the realization of an idea first proposed by John Wessel in 1985 [12]. In principle it can be viewed as a scannable version of surface-enhanced Raman scattering (SERS) which had been explored since 1974 [85]. For SERS, the strongly enhanced local near-fields of an illuminated rough silver film are used. In a random distribution of nanoscale metal grains, selected spots exhibit an enormous field enhancement. These so-called "hot-spots" are particle arrangements with a strong near-field coupling and a plasmon resonance matching the incident wavelength. In the gap between closely spaced particles, field enhancement factors of several orders of magnitude can be expected. If a Raman active analyte is put onto such a film, some molecules will be

placed within such hot-spots and their Raman intensity will be boosted. Single-molecule SERS and intensity enhancement factors of 10^{14} have been reported [86].

Wessel's idea is similar to taking such a hot-spot as a scannable probe for high-resolution and high-sensitivity Raman spectroscopy. This was termed tip-enhanced Raman spectroscopy (TERS) and was successfully implemented in 2000 by Stöckle *et al.* [87]. In recent years, TERS has drawn more and more attention and is being explored by many groups [13, 88–91]. TENOM is a generalization of TERS, including other optical processes such as fluorescence or photoluminescence, where tip-enhancement can be used in the same way [92, 93].

3.3.1 Field enhancement at a metal tip

The image resolution and contrast in a TENOM experiment depends critically on the strength and confinement of the tip-generated field. For a quantitative analysis and interpretation of experimental data, it is helpful to understand the field enhancement at the metal tip. The exact field distribution for a certain tip geometry can not be found analytically as for spherical or ellipsoidal nanoparticles. However, numerical simulations have shown that the fields in the vicinity of the tip apex can be quite accurately described by an effective dipole $\boldsymbol{\mu}(\omega)$ located at the center of the tip apex (see Fig. 3.5a and b) [8]. Its magnitude with respect to an exciting field $\mathbf{E}_{exc}(\omega)$ can be written as

$$\boldsymbol{\mu}(\omega) = \begin{bmatrix} \alpha_{\perp} & 0 & 0 \\ 0 & \alpha_{\perp} & 0 \\ 0 & 0 & \alpha_{\parallel} \end{bmatrix} \mathbf{E}_{exc}(\omega) \quad (3.14)$$

where the z-direction is set along the tip axis. The tip is assumed radially symmetric with the polarizability α_{\perp} perpendicular and α_{\parallel} parallel to its axis. These are defined by

$$\alpha_{\perp} = 4\pi\varepsilon_0 r_0^3 \frac{\varepsilon(\omega) - 1}{\varepsilon(\omega) + 2} \quad (3.15)$$

and

$$\alpha_{\parallel} = 2\pi\varepsilon_0 r_0^3 f(\omega) \quad (3.16)$$

where $\varepsilon(\omega)$ is the complex bulk dielectric constant of the tip material, r_0 is the tip radius and f is the field enhancement factor. α_{\perp} is equivalent to the polarizability of a small sphere with radius r_0 and α_{\parallel} is defined such that the field at the surface of the tip end is $f\mathbf{E}_{exc}$. With this definition of the tip dipole, the electrical field in the vicinity of the tip can be calculated as

$$\mathbf{E}(\mathbf{r}, \omega) = \mathbf{E}_{exc}(\omega) + \frac{\omega^2}{\varepsilon_0 c^2} \overset{\leftrightarrow}{\mathbf{G}}(\mathbf{r}, \mathbf{r}_0, \omega) \boldsymbol{\mu}(\omega) \mathbf{E}_{exc}(\mathbf{r}_0, \omega). \quad (3.17)$$

Here, \mathbf{r}_0 specifies the origin of $\boldsymbol{\mu}$ and $\overset{\leftrightarrow}{\mathbf{G}}$ is the free-space dyadic Green's function in the absence of the tip. The field enhancement factor f can be derived from numerical calculations and depends on the tip geometry and material.

For a gold tip with $r_0 = 10$ nm and an excitation wavelength of 830 nm, the dielectric constant is $\epsilon = -24.9 + 1.57i$ and a typical value would be $f = -2.9 + 11.8i$ [94]. These values lead to $|\alpha_{\parallel}| \gg |\alpha_{\perp}|$, which points out the big advantage of a sharp metal tip compared to a single sphere with the same radius. The polarizability of the tip is higher, since more material and thus electrons can be excited. For longitudinal excitation and oscillation, the charge density will be concentrated towards the tip end and yields the strong field enhancement, reminiscent of the lightning-rod-effect. The simulated field distribution for a tip and a particle are shown in Fig. 3.5a and b. They are indeed very similar, but the field intensity at the tip is 50 times stronger. The longitudinal polarization of the exciting field is crucial for high enhancement, which must be considered in the experimental realization. The enhanced field is confined within few nanometer near the tip apex. The probed sample area and thus the spatial resolution in a TENOM experiment is slightly smaller than the tip diameter $2r_0$.

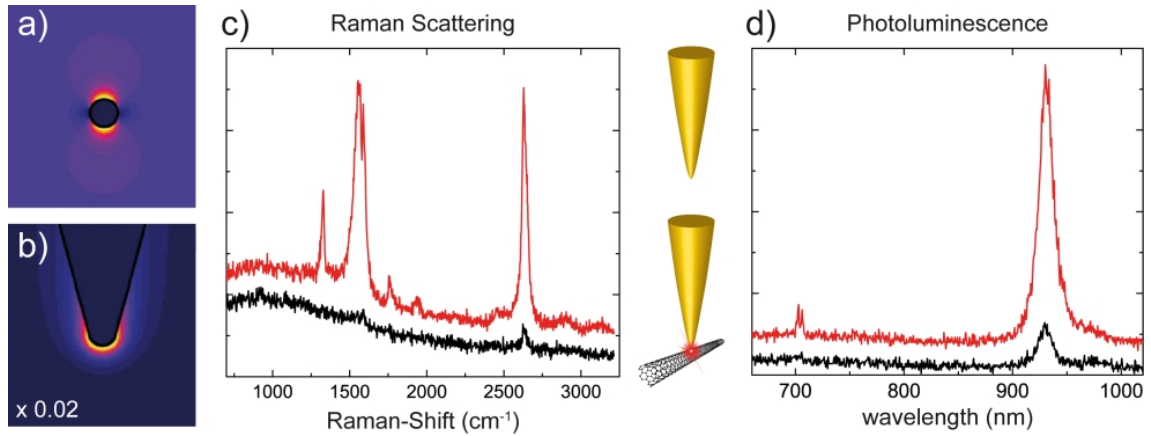


Figure 3.5: Field enhancement at a metal tip and signal enhancement of Raman Scattering and PL. a) and b) Optical field intensity $|\mathbf{E}|^2$ in the vicinity of a small spherical gold particle and a gold tip upon laser illumination with vertical polarization. The fields are calculated numerically based on the multiple multipole method. Tip and particle have a radius of 10 nm and the laser wavelength is 830 nm. The field in b is scaled by 0.02, i.e. 50 times stronger than for the particle in a. The field distributions are very similar, which means that the tip can be modeled as a particle with an enhanced longitudinal polarizability reflecting the tip’s field enhancement factor. The images were taken from ref. 95. c) and d) Tip-enhanced Raman scattering and photoluminescence spectra. Black lines show the far-field spectrum with retracted tip and the red lines are the spectra with the tip landed on the SWNT.

The best tip material for high enhancement factors in the visible range is gold. It has its plasmon resonance in the green, which is shifted to the red for a tip-shaped geometry. The plasmon damping is rather low and gold is chemically inert. Furthermore, sharp gold tips can be easily fabricated by electrochemical etching. Silver tips could provide even higher enhancement factors at blue wavelengths, but surface degradation due to the formation

of oxides and sulfides is critical and strongly limits the durability in ambient conditions. Silver tips can also not be fabricated as easily.

Many theoretical investigations have studied optimum parameters for the tip geometry as e.g. radius and opening angle. In general, the enhancement increases with smaller radius which is the most important parameter. It is limited by the mechanical stability of gold and can be around 5 – 10 nm in the best case. An optimum opening angle of 20 – 30° is predicted, but is not as relevant. A significant improvement can be expected for tips with a finite length, where an additional particle plasmon resonance could be achieved [96–98]. This would correspond to a resonant optical antenna [80,99]. However, the nano-fabrication of tips with a controlled geometry and a defined length is challenging. Gold nanorods as an optical antenna are promising, if they can be fixed in the right orientation at the end of a scannable probe. So far, electrochemically etched gold tips have been a good compromise for a reasonable TENOM experiment.

3.3.2 Signal enhancement

Raman scattering

The signal enhancement for Raman scattering due to field enhancement can be very large, as has been shown in SERS experiments. If k^{tip} and k^0 denote the transition rates with and without the tip, then the Raman intensity enhancement M_R can be written as

$$M_R = \frac{k_{ex}^{tip} k_{rad}^{tip}}{k_{ex}^0 k_{rad}^0} \quad (3.18)$$

where k_{ex} is the excitation rate and k_{rad} is the radiative rate. Both rates are proportional to the field intensity at the respective frequency and thus

$$M_R = \left[\frac{E^{tip}(\omega_L)}{E^0(\omega_L)} \right]^2 \left[\frac{E^{tip}(\omega_L - \omega_{ph})}{E^0(\omega_L - \omega_{ph})} \right]^2 \approx f^4. \quad (3.19)$$

Since the Raman-Shift ω_{ph} is rather small, the field enhancement factor at the scattered frequency can also be taken as f and $M_R \approx f^4$. This means, that even for moderate enhancement factors of 5 – 10, an enormous signal enhancement in the order of $10^3 - 10^4$ can be realized for the small area A_{tip} underneath the tip.

However, as mentioned earlier, the signal enhancement that is detected in the far-field is reduced by a factor of A_{ff}/A_{tip} , because an area of A_{ff} is always illuminated by the far-field and contributes to the detected signal. Fortunately, for the one-dimensional carbon nanotubes studied in this work, only a length ratio $L_{ff}/L_{tip} = \sqrt{A_{ff}/A_{tip}}$ has to be considered. Fig. 3.5c shows the Raman spectra of a metallic SWNT with the tip retracted (black line) and landed on the SWNT (red line). The overall signal enhancement is about 40. Assuming L_{ff}/L_{tip} to be ~ 15 (300 nm vs. 20 nm tip diameter), the field enhancement factor can be estimated as $f = \sqrt[4]{40 \cdot 15} \approx 5$.

The signal enhancement depends strongly on the tip-sample distance due to the rapid decay of the near-field. For the case of one-dimensional SWNTs, Cañado *et al.* [94] showed that the detected near-field signal is proportional to $(d + r_0)^{-10}$, where d is the tip-nanotube distance. This dependence can be measured by recording an approach curve, where the Raman intensity is detected during the controlled approach of the tip to the surface. A typical approach curve for the tip-enhanced Raman G-band intensity of a SWNT is shown in Fig. 3.6a.

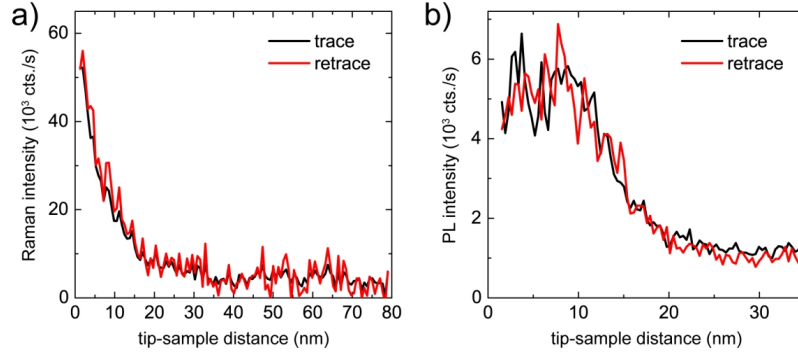


Figure 3.6: Typical approach curves for the tip-enhanced Raman scattering and PL intensity. a) Raman G-band intensity detected by APD (bandpass for $1580 \pm 100 \text{ cm}^{-1}$) plotted against tip-sample distance. The signal increases sharply in the last 20 nm, which reflects the extension of the enhanced near-field in z-direction. b) Photoluminescence intensity detected by APD (longpass 950 nm) plotted against tip-sample distance. As for the Raman signal, the intensity increases at near-field distances, but then saturates and eventually decreases due to PL quenching by the metal tip.

It can be clearly seen that the signal increases sharply for distances below 20 nm, when the near-field of the tip interacts with the nanotube. The steep slope reflects the small extension of the near-field in z-direction. This points out that the tip-sample distance must be kept stable at a few nanometers in a TERS experiment and that distance modulations lead to large signal variations. Approach curves are also important to verify a near-field effect, which is always characterized by clear changes within very small distances.

Photoluminescence

The signal enhancement for the photoluminescence process is described differently. The excitation process is the same and k_{ex} is also increased by f^2 . However, the radiative process should be treated differently. The presence of the tip opens up additional decay pathways for the excited E_{11} exciton. The radiative rate k_{rad} will be increased due to additional radiation via the tip as an optical antenna. Furthermore, the tip can also increase the non-radiative decay rate k_{nr} by means of energy transfer to the tip and non-

radiative dissipation in the metal. As the fraction of radiated PL photons per excitation events is given by the quantum yield QY, the PL signal enhancement can be written as

$$M_{PL} = \frac{k_{ex}^{tip}}{k_{ex}^0} \frac{QY^{tip}}{QY^0} = f^2 \frac{QY^{tip}}{QY^0} \quad (3.20)$$

where the different decay rates are summarized in the quantum yield with and without the tip. The equation shows, that the PL enhancement can be large for a low intrinsic quantum yield QY^0 which can be significantly increased by the tip. For high QY emitters such as fluorescent dyes, the possible signal enhancement is limited to about f^2 and can even decrease at very small distances due to efficient non-radiative energy transfer to the tip. This quenching effect entails an optimum distance for maximum enhancement [100].

A typical approach curve for the tip-enhanced photoluminescence intensity of a SWNT is shown in Fig. 3.6b. Similar as for the Raman enhancement, the intensity increases only at near-field distances. However, at very small tip-nanotube distances the signal tends to saturate and eventually decreases slightly. At such close distances, the non-radiative rate enhancement by the metal tip reduces the quantum yield and thus PL intensity. In a typical TENOM experiment, the tip-sample distance is kept at a few nanometers, where PL quenching does not yet influence the enhancement significantly.

For SWNTs from aqueous suspensions with an intrinsically low quantum yield of about 10^{-3} [50, 52, 101], the radiative rate enhancement can be substantial, whereas the high non-radiative rate k_{nr}^0 is not strongly affected. In this case, the PL enhancement can be estimated as

$$M_{PL} = f^2 \frac{k_{rad}^{tip}}{k_{rad}^0}. \quad (3.21)$$

Fig. 3.5d shows the spectra of a semiconducting (9,1)-SWNT with the tip retracted (black line) and landed on the SWNT (red line). The PL signal is enhanced by a factor of about 7, corresponding to $M_{PL} \approx 70$ (tip diameter ~ 30 nm here). Very recently, a radiative rate enhancement in the range of 6 – 14 has been determined for the PL of carbon nanotubes [102]. This value is considerably lower than f^2 , because the PL wavelengths in the near infrared are further away from the plasmon resonance of gold and the resonance of the optical antenna. The overall signal enhancement is again decreased by the far-field background and furthermore reduced by the effect of exciton mobility which will be discussed in chapter 6.

3.3.3 Illumination schemes

There are several different possibilities to implement a TENOM setup. In principle, an optical laser scanning microscope has to be combined with an atomic-force microscope (AFM) for the tip-sample distance control. The three common designs that are presented in the following differ in the arrangement of illumination with respect to the tip. These three different setup designs or illumination schemes are shown in Fig. 3.7.

In general, it is desirable to have a high detection efficiency, which means that most of the light emitted by the sample is collected. The solid angle under which radiation is detected is defined by the NA, which should be maximized. For dielectric substrates, most of the radiation from a dipole on the surface is emitted into the dielectric and not into free space. Collection through the sample can thus be very beneficial, particularly when oil-immersion objectives with $NA > 1$ can be used. To suppress the far-field background, a small excitation area A_{ff} is desirable which also requires a high NA. Regarding the samples that can be studied, it is very advantageous when opaque substrates are usable. Especially for ultra-high field enhancement, a flat metallic substrate is needed to form a gap configuration with the tip, similar as the "hot spots" in SERS.

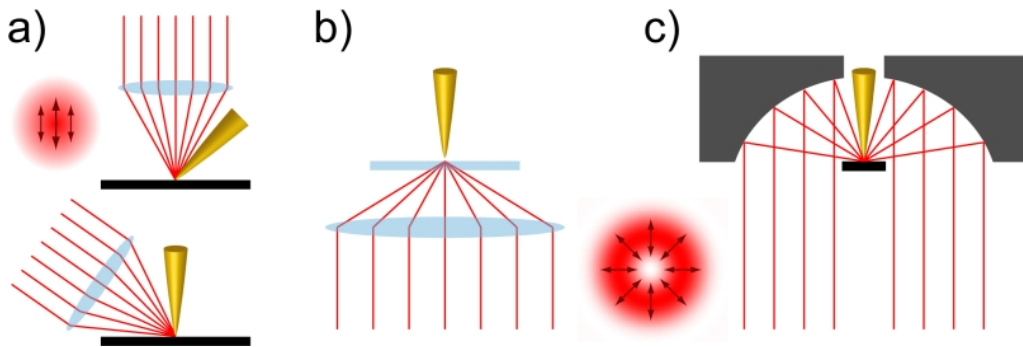


Figure 3.7: Three possible setup designs for a TENOM experiment differing in the arrangement of illumination with respect to the tip. They generally have to provide an excitation with a strong longitudinal polarization component for maximized enhancement. a) Side-illumination, where the tip is excited from the side with a focused linearly polarized laser. Here, only low NA objectives can be used, but this design is applicable to opaque samples. b) On-axis illumination through a transparent sample, where the tip is illuminated by a high NA oil-immersion objective from below. Higher-order laser modes as e.g. the shown radially polarized donut mode are necessary to generate a strong longitudinal field component. Opaque samples can not be studied, but the detection efficiency is maximized. c) On-axis illumination using a parabolic mirror. Here, a high NA (≈ 1) is combined with the possibility to study opaque samples. The laser must also be radially polarized.

Fig. 3.7a illustrates the side-illumination design. Here, the tip is illuminated from the side under an angle of about 60° and the focused laser is linearly polarized along the tip axis. The objective can either be tilted and the tip is perpendicular to the sample, or the tip is tilted and the objective is straight above the sample as in many standard optical microscopes. The main drawback is that objectives with a long working distance and therefore low NA have to be used, strongly reducing the detection efficiency and the near-field contrast.

Fig. 3.7b illustrates the on-axis illumination from below the sample. Here, the illumination direction is aligned along the tip axis and the exciting laser is transmitted through the sample. Oil-immersion objectives with a NA up to 1.49 can be used, which maximizes

the detection efficiency and near-field contrast. Detection is from the substrate side and most of the emitted radiation can be collected. To generate a strong longitudinal field component, higher-order laser modes as e.g. a radially polarized donut mode have to be used. The main disadvantage is, that only transparent substrates with a defined refractive index and thickness, usually glass cover slides, can be studied. This approach was employed for the experiments presented in this work.

An interesting compromise is the on-axis illumination using a parabolic mirror, as shown in Fig. 3.7c. The mirror offers a NA near unity and the far-field focus can be smaller than for conventional optics [103]. Strong longitudinal field components are generated using a radially polarized laser mode. Detection efficiency is comparably high, albeit detection is from above and emission into the substrate is lost. In this approach, opaque samples can be studied which also allows the use of a metal substrate for ultra-high field enhancement. Single-molecule TERS has been achieved in this configuration [77].

3.4 Far-field concepts

In the last decade, new concepts of sub-diffraction microscopy have emerged and became increasingly successful in nanoscale fluorescence imaging. They are based on far-field excitation and far-field detection using conventional optics. Nevertheless, fluorescence imaging with 20 nm resolution is possible, justifying the denotation as "far-field nanoscopy" [104]. Two different general concepts will be discussed in the following.

The first concept is based on the fundamental idea, that the position of a single emitter can be determined with almost arbitrary accuracy, even though its point-spread function has a width of several hundred nanometers. The detected image of the single emitter can be fitted with the known PSF of the system and position accuracy is only limited by the signal-to-noise-ratio. Few nanometer accuracy can be obtained. In order to use this idea for nanoscale imaging, closely spaced emitters must not emit at the same time to avoid the overlap of their PSF. If they emit separated in time, i.e. one after another, their positions can be sequentially determined with nanometer accuracy. For fluorescent molecules, this can be achieved using dark states where the molecules are "switched off" and do not emit.

Special fluorescent molecules that can be switched on and off with certain laser wavelengths are used for a technique called stochastic optical reconstruction microscopy (STORM) [105]. Two successive laser pulses of different wavelengths are used to activate and deactivate the molecules. The first pulse deactivates all molecules in the observation area and the following activation pulse, which is very weak, randomly activates few of them. If the power of the activation pulse is low enough, the average number of molecules in the on-state is such that their average distance is much larger than the width of their PSFs. A wide-field image is recorded and the positions of these few molecules are determined and saved. Afterwards, a new pair of pulses deactivates and activates again. This stochastic

process is often repeated until most of the molecules have been traced at least once and a high-resolution image is formed by displaying all the calculated positions. The technique photo-activated localization microscopy (PALM) [106] is very similar. Most molecules are in the off-state, some of them are activated by an activation pulse and then these are imaged until they are bleached.

A different concept is realized by stimulated emission depletion (STED) microscopy where the molecular ground state is used as the off-state and no fitting of the PSFs is necessary. Here, two strongly focused laser pulses are used which are overlapping on the sample. The first pulse excites the molecules within a diffraction limited focal area. The second pulse is red-shifted and has a ring-shaped intensity distribution with zero intensity in its center. It leads to stimulated emission of the irradiated molecules, thereby depletes their excited state and brings them back to the ground state. Only the molecules in the center of the second pulse are not affected and can still fluoresce, i.e. decay via spontaneous emission. The fluorescence is then detected by a photo diode. The resolution of STED is given by the area in the center of the focus, where molecules are not deactivated. It depends on the intensity ratio of the two pulses and can be as small as 20 nm.

Both concepts rely on the labeling with specific dye molecules. They are now widely used for biological applications and microscopes are commercially available. For very high resolution images, the labeling molecules must have a density of at least $1/(10\text{ nm})^3$ which might influence the studied biological system. 3D imaging of cells is possible, since these far-field techniques are not restricted to surfaces. However, high resolution spectroscopy of the intrinsic sample properties is not possible.

A far-field approach similar to STORM has also been employed for sub-diffraction PL imaging of single-walled carbon nanotubes [107]. These were not labeled, but kept in an acidic environment where their PL emission is blinking. Reversible single-molecule chemical reactions of the SWNTs create a localized single quenching site which switches off PL in its vicinity. The impact of a single quenching site is extracted from differential PL images and can be fitted to determine its location on the SWNT with nanoscale resolution. Thereby, the luminescent parts of the nanotube can be imaged. Though no near-field optics are needed in this approach, the information that can be gained from these experiments is limited. The luminescent parts of the SWNT and permanent quenching sites can be located with sub-diffraction resolution. However, along the nanotube axis, the resolution is limited by the exciton diffusion length in the range of 100 nm. Furthermore, spectral information that could reveal also exciton energies can not be obtained with nanoscale resolution due to the need for fast wide-field imaging. Above that, the SWNTs must be kept in a specific environment that drastically alters the PL properties and they can not be studied in a specific arrangement such as a device configuration.

Conclusion

It was shown that the resolution limit of conventional optical microscopy arises from the propagation of light to the detector. It can be circumvented by exciting and detecting the optical signals in the near-field of the sample, where sub-wavelength spatial information is still contained in the emanating fields. The simplest implementation of near-field microscopy is a tiny aperture that is scanned across the sample, but this approach suffers from the very low light throughput and thus very low sensitivity. Tip-enhanced near-field microscopy uses the field enhancement at a sharp metal tip to locally amplify the near-field signal, which offers a much higher sensitivity.

Far-field nanoscopy techniques have been discussed, but these can not be used to image the intrinsic optical properties of the sample. They require extensive labeling with specific fluorescent dyes or particular modifications of the sample environment, leading to characteristic blinking properties of its fluorescence. Only the location of single emitters can then be determined with nanometer resolution.

For high-resolution imaging of the intrinsic optical properties of SWNTs, such as Raman scattering and photoluminescence, TENOM is ideally suited. It offers very high sensitivity, additional topographic information and reasonable near-field to far-field contrast owing to the 1D nature of SWNTs. Their intrinsic low quantum yields allows for a strong tip-induced radiative rate enhancement, which increases the detected PL signal. The detection sensitivity can furthermore be optimized by using an oil-immersion objective in the on-axis illumination scheme (as illustrated in Fig. 3.7b). The high signal enhancement and detection efficiency is crucial for high-resolution PL imaging of SWNTs, because they tend to photo-bleach during the experiment and can only be excited at very low laser intensities.

4 Experimental details

This chapter provides an overview of the experimental setup. The TENOM setup consists of a standard inverted optical microscope combined with an atomic force microscope based on shear-force detection. Both parts will be described in individual sections. Then, some details on the sample preparation will be given. Finally, the general strategies to acquire near-field images are described.

4.1 TENOM setup

4.1.1 Confocal laser scanning microscope

The setup is based on the inverted confocal optical microscope Nikon Eclipse TE2000. The microscope is used in sample scanning mode, which means that the excitation laser is focused onto the sample and excites an optical response (e.g. Raman scattering or photoluminescence) within the focal area. This optical signal is then detected and an image is acquired by raster scanning the sample with respect to the fixed laser spot and recording the optical response at each image pixel. The x,y,z scan stage (Physik Instrumente PI - P-517.3) offers a scan range of $100\ \mu\text{m} \times 100\ \mu\text{m} \times 20\ \mu\text{m}$ with a resolution of about 1 nm. Coarse positioning is done by hand.

The laser used throughout this work is a red HeNe laser at a wavelength of 632.8 nm with an output power of approximately 20 mW. Two different oil-immersion objectives were utilized, one with a NA of 1.4 (Nikon CFI Plan Apo VC 60x NA 1.4) and in later experiments one with a NA of 1.49 (Nikon CFI Apo TIRF 60x NA 1.49), both highly corrected for chromatic aberrations and with reasonable transmission in the near-infrared. The objectives are infinity corrected, which means that a collimated laser beam entering the back aperture will be focused in the focal plane.

The schematic experimental setup is shown in Fig. 4.1. The laser passes a laser line filter (bandpass for $\lambda = 632.8\ \text{nm}$), is expanded by two lenses and then passes the mode converter, where its polarization is modified. A second beam expansion enlarges the diameter to fill the objective's back aperture. In this expansion, a pinhole at the focus position is used to provide a clean radially polarized mode. The mode conversion is discussed later in more detail. The laser is then reflected by a non-polarizing beam splitter and sent into the objective to be focused onto the sample. The sample response is collected by the same

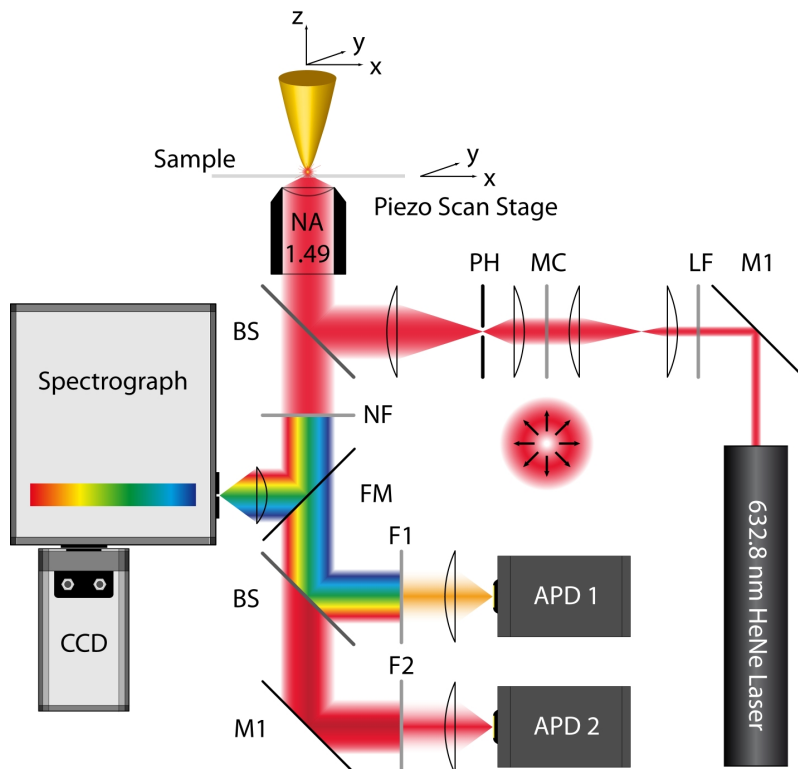


Figure 4.1: Schematic of the experimental setup. The laser passes a laser line filter (LF, bandpass for $\lambda = 632.8$ nm), is expanded by two lenses and then passes the mode converter (MC), where its polarization is modified. A second expansion enlarges the diameter to fill the objective's back aperture, a pinhole (PH) in the focus is needed to provide a clean radially polarized mode. The laser is then reflected by a beam splitter (BS) and sent into the objective. The sample response is collected by the same objective, transmitted by the beam splitter and separated from the reflected laser light by a notch filter (NF, bandstop for $\lambda = 632.8$ nm). This light can either be detected by the spectrograph and CCD, using the flip-mirror (FM) or it is passed to the avalanche photo diodes (APD). Another beam-splitter separates visible and near-infrared components for both APDs, where the light is detected after passing appropriate bandpass filters (F1, F2).

objective, transmitted by the beam splitter and separated from the reflected laser light by a notch filter (bandstop for $\lambda = 632.8$ nm). The light can then either be detected by the spectrograph (Andor shamrock 303i) and a charge-coupled device (CCD) camera (Andor iDus DU420-BR-DD) or it is passed to two avalanche photo diodes (APD). Another beam-splitter separates visible and near-infrared components for both APDs, where the light is detected after passing appropriate bandpass filters. Typically, the first APD detects the Raman G-band at 703 nm using a bandpass filter (HQ703/10m, Chroma) and the second APD detects the photoluminescence using a longpass filter (HQ863LP, Chroma). This allows simultaneous imaging of Raman scattering and photoluminescence. The APDs and CCD have a strongly decreasing detection efficiency towards the near-infrared and the maximum wavelength that can be detected is around 1030 nm. SWNT photoluminescence can therefore only be detected for nanotubes with diameters below 0.85 nm.

Mode Conversion

As mentioned earlier, it is crucial for TENOM to excite the tip with a strong longitudinal component. For the on-axis illumination used in this work, this requires the focusing of a higher-order laser mode. Focusing a linearly polarized laser mode yields only weak longitudinal components, in the following denoted as z-components.

The higher-order laser mode is generated by a mode converter as shown in Fig. 4.2a. It consists of four segments of $\lambda/2$ wave plates, each with a different orientation of their optical axis. The linearly polarized laser beam passes the mode converter and has an intermediate mode afterwards, with four regions of linear polarization oriented vertically and horizontally, where opposing regions have opposite polarization. Focusing this mode through a pinhole then yields a clean radially polarized mode, because deviations contained in the intermediate mode are rejected.

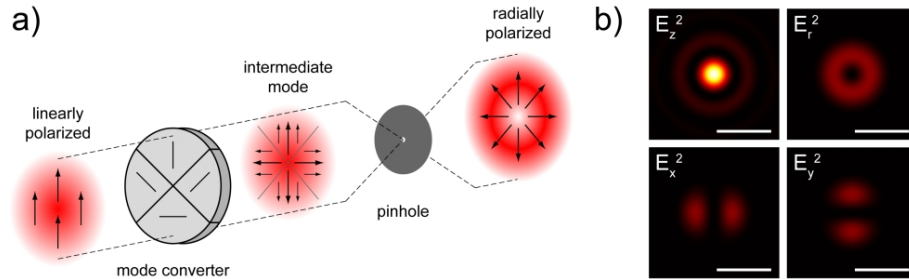


Figure 4.2: a) Generation of a radially polarized donut mode from a linearly polarized laser. The mode converter consists of four segments of $\lambda/2$ wave plates, each with a different orientation of their optical axis. After passing the mode converter, the laser has an intermediate mode with four regions of linear polarization oriented vertically and horizontally, respectively. To derive a clean radial polarization, higher-order deviations are rejected by focusing through a pin-hole, which is called spatial filtering. b) Distribution of the different polarization components after focusing the radially polarized laser ($\lambda = 632.8$ nm) with a 1.49 NA objective. E_z^2 and E_r^2 are the longitudinal and transverse components. E_x^2 and E_y^2 are the transverse in-plane components, separated by x- and y-direction. The scalebar is 500 nm.

When this radially polarized donut mode is used, the anti-parallel polarizations from opposing sides of the laser beam are turned into the z-direction by the strong focusing at large angles θ , which are provided by the high NA. In the center of the focus, constructive interference of the radial components leads to a strong z-component. The individual components in the focus are plotted in Fig. 4.2b. The z-component E_z^2 in the center is about 5 times stronger than the ring-shaped radial components E_r^2 , when the 1.49 NA objective is used. Lower NA strongly decreases this ratio and significant z-components can only be achieved for $NA > 1$. The separation of the in-plane radial components into x- and y-components yields a typical double-lobe pattern. The distance of these two lobes is about 350 – 400 nm and the width of the z-field distribution is about 250 nm, given a laser

wavelength of 632.8 nm. These numbers determine the optical resolution for the diffraction limited imaging without tip-enhancement.

4.1.2 Shear-force AFM

The sharp gold tips that are used in the TENOM experiment are rather soft and can not withstand strong forces. The feedback mechanism that controls the tip-sample distance to keep it at few nanometers must be very sensitive and apply only small forces. Contact mode and tapping mode AFM techniques are not applicable. The detection of distance dependent shear-forces that arise from a lateral vibration of the tip parallel to the sample surface has been established as a very gentle method for distance control. Monitoring a tunnel current from tip to sample, i.e. scanning tunneling microscopy (STM), is a good alternative but requires conductive samples.

Principle of shear-force detection

The measurement of very small forces in the pN range is challenging. A very practical solution is the conversion of this small force into a frequency variation of an electrical signal, which can be measured with outstanding accuracy. The common approach for the distance control of near-field probes is the use of tuning fork (TF) sensors [108]. The quartz tuning forks are the same as used in quartz watches. Their two prongs are covered by a pattern of electrodes that are used to connect them to an external electronic circuit. The mechanical oscillation generates an oscillating output voltage due to the piezoelectric effect. Vice versa, the TF oscillation can be driven by applying a harmonic signal. These tuning forks have a size of about $1 \times 2 \times 4$ mm and a resonance frequency of 32,768 Hz (2^{15} Hz). The oscillation with very small amplitudes can be described by a harmonic oscillator model, where the time and frequency dependent complex amplitude is given by

$$A(t) \propto \frac{e^{-i2\pi t}}{f_0^2 - f^2 - i \cdot f f_0 / \sqrt{3}Q}. \quad (4.1)$$

Here, f and f_0 are the actual oscillation and resonance frequency, respectively [8]. The quality factor Q reflects the damping and is defined as

$$Q = \frac{f_0}{\Delta f} \quad (4.2)$$

where Δf is the full-width-at-half-maximum (FWHM) of the resonance peak $|A(f)|$ which is a Lorentzian curve. The real part of the amplitude has the form

$$A(t) = |A(f)| \cdot \sin[2\pi f t + \varphi(f)] \quad (4.3)$$

where $\varphi(f)$ is the phase shift with respect to the harmonic driving force, which is 0° far below resonance, 90° at resonance and 180° far above resonance. The frequency dependent amplitude and phase are shown in Fig. 4.3b (black curves).

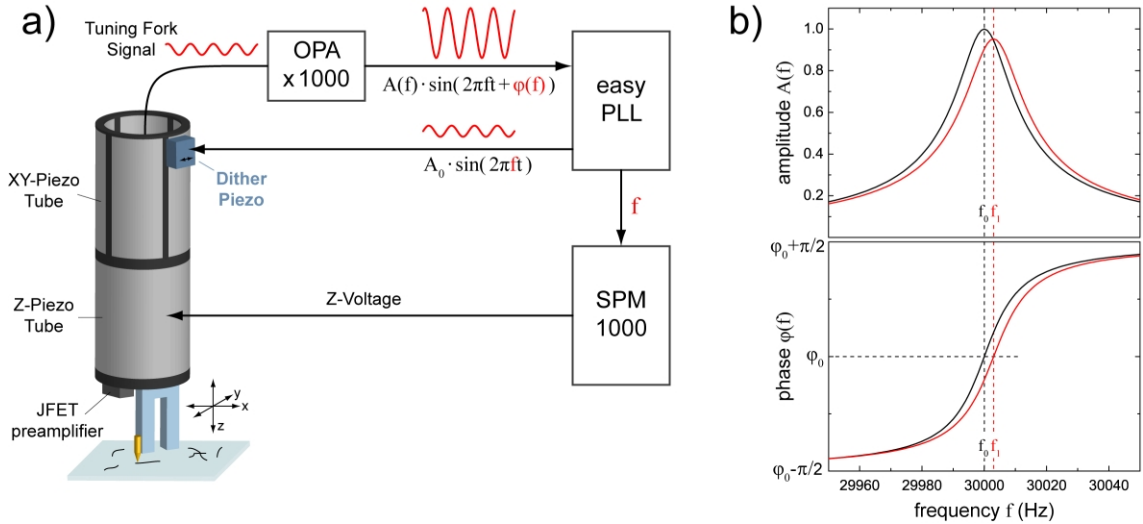


Figure 4.3: Schematic of the shear-force feedback for tip-sample distance control. a) The tuning fork is mechanically driven at a frequency f by a dither piezo. The output signal is amplified and then detected by a phase-locked loop (easyPLL). The output phase φ is kept constant at φ_0 by varying f , which then corresponds to the resonance frequency. The value of f is constantly handed on to the SPM controller, that varies the tip-sample distance in order to keep the frequency shift $f - f_0$ constant. b) Frequency dependent oscillation amplitude and phase of the tuning fork oscillation. Black and red curves depict the free-space oscillation and the case with tip-sample interaction, respectively. The shear-forces between tip and surface slightly shift the resonance frequency to f_1 and slightly reduce the quality factor and thus the amplitude. The phase φ_0 at the respective resonance frequency stays the same and is used to determine this frequency.

The gold tip is attached to one of the tuning fork prongs. Its mass changes the resonance frequency to values of 30,500 – 31,500 Hz and the quality factor is in the range of 1000. When the tip approaches the sample surface, shear forces will result from the lateral vibration of the tip with respect to the surface. These forces are strongly distance dependent and become significant at nanometer distances. They lead to a slight damping of the tuning fork oscillation resulting in a lower amplitude and a shift of the resonance frequency from f_0 to f_1 . This is also shown Fig. 4.3b (red curves).

Tip-sample distance control

In order to detect the shear-forces, one can monitor the amplitude at a constant driving frequency using a lock-in detector. The tuning fork is excited slightly off-resonance where $dA(f)/df$ is large. The shift of the resonance frequency due to the shear-force will then lead to changes in the amplitude. This approach has the big disadvantage of a fairly long response time. It takes approximately $2Q$ oscillation cycles for the system to respond to an interaction and reach the new steady-state [8]. This time is in the 100 ms range and too long for feedback purposes.

A faster and more sensitive approach is to detect the shift of the resonance frequency directly. In a first approximation, the resonance frequency responds instantaneously and it takes only several cycles for determination [8,109,110]. It is monitored using a phase-locked loop (PLL), similar to frequency modulators used in radios. As apparent in Fig. 4.3b, the phase curve is only shifting in f and the phase value at the new resonance frequency f_1 is the same as before.

The PLL system (easyPLL, Nanosurf[©]) drives the tuning fork at a variable frequency f , using an extra dither piezo that is mechanically coupled to the TF. The output voltage from the TF is amplified by a JFET preamplifier circuit (impedance conversion) and an operational amplifier (OPA, 1000 \times voltage gain). The PLL measures the phase of this output with respect to the driving and maintains its value at φ_0 by varying the driving frequency f . Then, f always corresponds to the actual resonance frequency f_1 and is handed on to the surface probe microscopy (SPM) controller (SPM1000, RHK Technology). This is the phase feedback which is illustrated in Fig. 4.3a. The oscillation amplitude of the tip parallel to the surface is in the picometer range, due to the high stiffness of the tuning fork. The force acting on the tip is some tens of pN, which is low enough to scan soft gold tips [8].

The SPM controller is generating the voltages that are applied to the piezo tubes with which the position of the tip can be controlled in x-,y- and z-direction (see Fig. 4.3a). The z-voltage which determines the tip-sample distance is varied in order to keep the frequency shift $f_1 - f_0$ constant. This is the z-feedback. Typically, a shift of about 1.5 Hz is used, corresponding to a tip-sample distance of few nanometer. The x- and y-voltages are used for precise positioning of the tip inside the laser focus. The SPM controller is furthermore controlling the scan stage and records the APD photon count rates. Optical images are generated by plotting these rates against the scan stage position. The topography of the surface, i.e. its height modulations, are reflected by the z-voltage at each sample position.

Fabrication of sharp gold tips

The fabrication of sharp gold tips for TENOM is based on electrochemical etching of a thin gold wire in hydrochloric acid as described in refs. 111–113. A quartz cuvette is filled with ultra-pure fuming hydrochloric acid and a ring electrode (\varnothing 5 mm) made of platinum wire is immersed about 4 mm below the acid surface. The gold wire (\varnothing 100 μ m, 99.995%, Chempur) is dipped \sim 0.5 mm into the acid above the center of the ring electrode. The etching voltage is supplied by a function generator and consists of square DC pulses with a length of 30 μ s and an amplitude of 8 V at 3 kHz repetition rate. The on/off-ratio of \sim 0.1 facilitates the constant supply of fresh chlorine ions to the gold surface, where they are consumed in the etching process. This generated voltage is applied between tip (+) and ring-electrode (-) by manual pulsing, while following the tip etching with a 40 \times stereo-microscope. The formation of the tip shape at the end of the immersed wire can be

influenced by the length of the applied manual pulses. These have to be shorter towards the end to avoid overetching. Afterwards the tips are rinsed in distilled water. All tips were briefly imaged with a scanning electron microscope (SEM) and only those with a symmetric tip shape and an apex diameter below 30 nm are used for TENOM. Fig. 4.4 shows some examples of electrochemically etched gold tips.

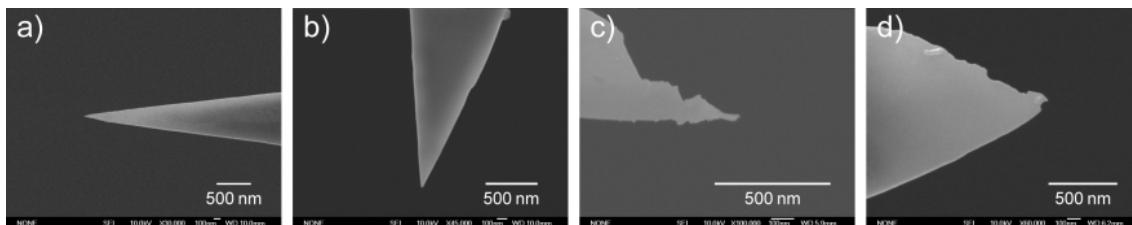


Figure 4.4: SEM images of electrochemically etched gold tips. a) and b) Tips suitable for TENOM, with a symmetric smooth shape and an apex diameter below 30 nm. c) and d) Irregularly shaped tips that will not be used.

4.2 Sample preparation

All samples are prepared on transparent glass cover slides with a size of $24 \times 24 \text{ mm}^2$, a thickness of 0.13 – 0.16 mm and a refractive index of ~ 1.52 (Marienfeld GmbH). These are index-matched with the immersion oil ($n = 1.518$) and thin enough for the limited working distance (0.2 mm) of the objectives.

Semiconducting SWNTs dispersed with sodium cholate

The semiconducting SWNTs used throughout this work were provided by the group of Prof. Mark C. Hersam (Northwestern University, Illinois). These are produced using the CoMoCat (cobalt-molybdenum catalyst) process, which yields a narrow distribution of small diameters of 0.7 – 1.1 nm. They were further sorted by diameter, using discriminating surfactants and density gradient ultracentrifugation [56, 114, 115], which isolates narrowly distributed, chirality enriched nanotubes. This enrichment allows measurements on numerous tubes with the same chirality and these SWNTs have their PL energy within the detection window of silicon based detectors ($< 1030 \text{ nm}$). The main chiralities are (6,4), (9,1), (8,3) and (6,5). The SWNTs were subsequently dialyzed to remove any density gradient medium (i.e. iodixanol) and then dispersed in aqueous solution using sodium cholate (1 wt%) as surfactant. The samples were prepared by spin-coating this nanotube solution onto a glass cover slide.

Semiconducting SWNTs wrapped with DNA

The SWNT preparation is the same, but instead of using sodium cholate, the nanotubes are dispersed in water using single-stranded DNA ([GT]₁₀) [116]. The binding of the DNA to SWNTs via π -stacking is stable and can separate nanotubes from bundles. The negatively charged DNA backbone makes the DNA-wrapped SWNTs soluble in water. No further surfactants or excess DNA is needed in the solution, which is beneficial for a defined sample topography without residuals.

Since the glass cover slides are rather hydrophobic, a freshly cleaved thin layer of mica (several μm thickness) was glued onto the surface. The mica was then positively charged by immersing the cover slide for about 20 min in a MgCl_2 solution (concentration 1 M). The Mg^{2+} ions compensate the negative surface charges of freshly cleaved mica. This drastically improves the adherence of the negatively charged DNA-wrapped SWNTs to the surface. The sample is again prepared by spin-coating the nanotube-solution onto the cover slide. An additional advantage of mica is the atomically flat surface, where SWNTs can be easily recognized in the topography.

Metallic SWNTs dispersed with surfactant

The metallic SWNTs used in this work were SWNTs produced in an arc discharge, dispersed with an ionic surfactant and sorted by density gradient ultracentrifugation to extract the metallic species (Nanointegris[©] IsoNanotubes-MTM, 99% purity). Their diameter is in the range of 1.2–1.7 nm with an average at 1.4 nm. According to the Kataura-plot (Fig. 2.6a), metallic nanotubes with a diameter around 1.25 nm have their E_{11}^M transition energy in resonance with the laser excitation at 632.8 nm. These yield a very strong resonance Raman scattering intensity. The samples were prepared by spin-coating the nanotube solution onto a glass cover slide and subsequent brief rinsing with distilled water to remove residual surfactant from the surface. This would otherwise cover the SWNTs and hinder the TENOM experiments.

4.3 Near-field imaging

4.3.1 APD based near-field imaging

The detection of the optical signals using the avalanche photo diodes is rather fast and efficient, but offers only limited spectral information. Usually, the Raman scattering and PL signal are recorded simultaneously using the two APDs (see Fig. 4.1) with a 703 ± 5 nm bandpass and a 863 nm longpass filter, respectively. First of all, a diffraction limited far-field image of a larger scan area (e.g. $20\times 20 \mu\text{m}^2$) is acquired to locate single SWNTs and

choose a position for the subsequent near-field scan. A typical far-field PL image is shown in Fig. 4.5a.

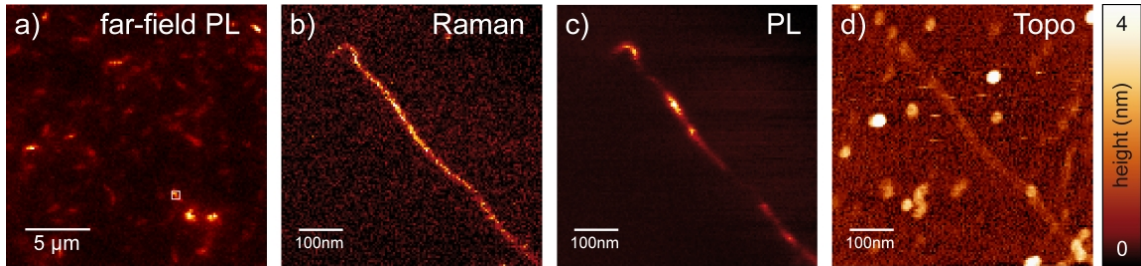


Figure 4.5: Simultaneous near-field Raman and PL imaging with APD detection. a) Diffraction limited far-field PL image ($20 \times 20 \mu\text{m}^2$, 128×128 pixel) to locate individual SWNTs. PL detected by APD using the 863 nm longpass filter. The white rectangle indicates the position of the subsequent near-field scan. b - d) Optical and topographical information recorded in the near-field scan ($600 \times 600 \text{ nm}^2$, 128×128 pixel). The Raman and PL signal were detected simultaneously with two APDs, using a $703 \pm 5 \text{ nm}$ band-pass and a 863 nm longpass filter, respectively. The optical resolution is 20 nm. The topography in d is rather blurred which is due to an irregular tip shape.

The acquisition time per pixel is 10 – 20 ms using a laser power of 5 – 10 μW on the sample. The spots mainly correspond to individual SWNTs but no detailed features can be studied due to the diffraction-limited resolution of 250 nm.

Afterwards, the shear-force scan head is placed onto the microscope, the tip will be approached to the surface and coarsely positioned inside the laser focus by observing it through the microscope eye-piece. The precise centering of the tip inside the laser focus for perfect alignment of the strongest z-component and the tip axis can be monitored by detecting the gold PL. The evanescent z-field in the focus can efficiently excite PL in the range of 650 – 750 nm arising from interband transitions in the gold, further enhanced by the plasmonic properties of the tip [117]. The gold PL is detected by the first APD using the same filter as for the Raman G-band. It is maximized by moving the tip in x- and y-direction using the SPM controller. Once the tip is centered, its position is maintained and the sample is scanned with respect to the fixed tip-laser configuration.

The range of a near-field scan is typically smaller than $1 \times 1 \mu\text{m}^2$ with a pixel size of only 5 – 10 nm. The scanning speed of the soft gold tip should be rather slow ($\sim 500 \text{ nm/s}$) to avoid damage. The optical and topographical information recorded in a typical near-field scan are shown in Fig. 4.5b-d. Simultaneous Raman scattering and PL signal can be obtained for resonant SWNTs as the (9,1). For sufficient tip enhancement as in this case, no far-field background is apparent in the images. Due to the spatial resolution of 20 nm, nanoscale variations of the signal intensities along the SWNT can be imaged. The PL is for example often very inhomogeneous for the DNA-wrapped SWNTs used here, which will be discussed in detail in the chapters 7 and 8.

The disadvantage of near-field images based on APD detection is the limited spectral information, which is only based on the utilized filters. These images are usually recorded to characterize an interesting sample position and optimize the enhancement before acquiring a time-consuming but much more informative spectroscopic image.

4.3.2 Spectroscopic imaging

For spectroscopic imaging, also denoted hyperspectral imaging, a complete spectrum is acquired at every image pixel using the spectrograph and the CCD camera. Thereby, any spectral information as e.g. peak intensities, peak positions and peak shapes are available at every pixel and individual images of these properties can be generated by subsequent data analysis. The acquisition time per spectrum is typically 0.5 – 2 s and thus much longer than for APD imaging. The maximum feasible number of pixels for a spectroscopic image is about 64×64 which takes more than one hour. Longer scans are hindered by tip drift leading to a gradual loss of the enhancement during the scan. The results from a spectroscopic image of a metallic SWNT are shown in Fig. 4.6.

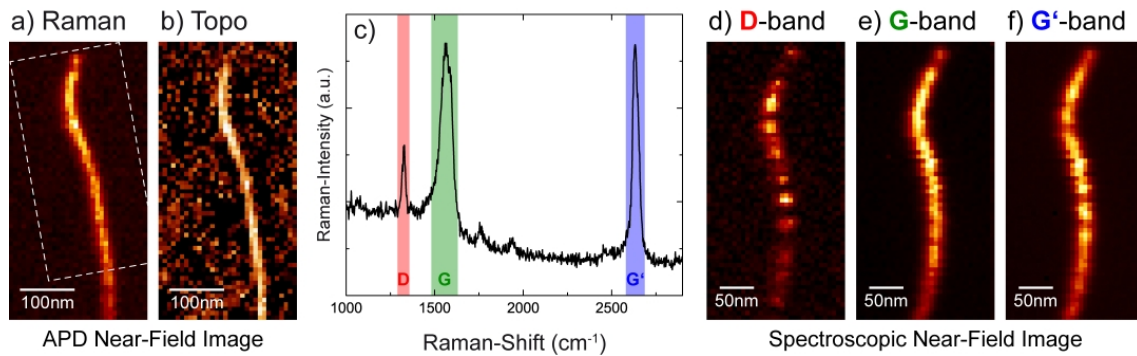


Figure 4.6: Spectroscopic near-field imaging using the spectrograph and CCD for detection of the optical signals. a) and b) Near-field PL and simultaneously recorded topography of a preceding scan with APD detection ($250 \times 500 \text{ nm}^2$, 32×64 pixel). The dashed white area indicates the position of the subsequent spectroscopic image. c - f) Spectrum and images from the spectroscopic near-field scan ($200 \times 400 \text{ nm}^2$, 32×64 pixel), where a spectrum was acquired at every image pixel. c) Representative spectrum from a specific pixel. d - f) Image of the D-, G- and G'-band intensity calculated by integrating the intensities within the spectral windows shown in c).

Three individual images for the Raman D-, G- and G'-band were generated by integrating the intensity within certain spectral windows as indicated in the spectrum in Fig. 4.6c. Apparently, the D-band is localized near defects, whereas G- and G'-band intensity are more homogeneous along the SWNT. A detailed study of these findings will be described in chapter 9.

Spectroscopic imaging of the PL properties can be done similarly. Thereby, the exciton energy variations along individual SWNTs can be imaged as reported in chapter 8.

5 Photo-induced photoluminescence bleaching and blinking

This chapter is based on the paper "*Photoinduced Luminescence Blinking and Bleaching in Individual Single-Walled Carbon Nanotubes*" that has been published in *ChemPhysChem* (Vol. 9, p. 1460–1464, 2008).

The temporal evolution of the photoluminescence from individual SWNTs under laser irradiation was studied. Generally, bleaching and pronounced blinking of the PL intensity was observed. The bleaching rate was investigated with respect to the incident laser power, the surrounding atmosphere (air or argon) and the substrate (bare glass or mica). It was found that the average bleaching rate increases with the laser power and is lower in argon atmosphere. The bleaching can be attributed to photo-induced oxidation of the SWNT, which introduces hole-doping leading to efficient exciton quenching.

Step-like changes in the PL time traces indicate single oxidation events generating a localized quenching site in a previously unperturbed luminescent SWNT segment. The strong PL decrease caused by a single quenching site reveals a high exciton mobility in SWNTs. The quenching affects a length corresponding to the exciton excursion range. The relative step-height of the PL change is connected to the ratio of excited SWNT length and the excursion range, which can thereby be determined.

5.1 Influence of excitation power and surrounding atmosphere

Since the discovery of PL from individual SWNTs [50,118], there has been extensive research towards their application as e.g. infrared markers [119,120] or sensors with single-molecule sensitivity [41,121]. For moderate excitation intensities up to 100 kW/cm^2 , stable PL has been reported for single SWNTs, making them ideal candidates for these applications [122–125]. However, PL blinking and bleaching was also frequently observed and can be mainly attributed to interactions of the nanotube with its local environment [41,57,123,124,126,127].

In general, hole-doping of SWNTs leads to efficient PL quenching. Regarding the responsible mechanism, an Auger recombination of excitons in the presence of doping and, more recently, a process called phonon-assisted indirect exciton ionization (PAIEI) have been

suggested as discussed in section 2.3 [54, 58, 59]. Hole-doping can result from several different processes such as protonation of adsorbed oxygen at the nanotube sidewall in acidic solutions [50, 57, 58] and electron transfer to electron accepting organic molecules [121, 128]. For SWNTs covered with surfactant and spun onto dielectric substrates, trapping of photo-excited charges from the nanotube in the surfactant layer is discussed [124, 127]. Furthermore the chemisorption of oxygen, initiated by irradiation or elevated temperature, leads to significant hole doping [129–131].

Applications in (opto-)electronics as well as studies of carbon nanotube PL properties widely utilize immobilized SWNTs on substrates and in ambient conditions. Here, bleaching and blinking of PL upon laser irradiation is often observed, yet the underlying mechanism is not fully understood. In order to provide insight in the underlying processes and identify ways to stabilize PL properties, this bleaching and blinking was studied with respect to the incident laser intensity, the surrounding atmosphere and the substrate.

The samples were prepared as described in section 4.2, using semiconducting SWNTs dispersed with sodium cholate. The substrate was either a bare glass cover slide or a cover slide with a thin layer of mica. They were prepared and stored at ambient conditions. To exclude chirality induced effects, only individual (6,5) SWNTs identified by their PL energy were investigated. They were illuminated by the laser while series of spectra were recorded to derive the temporal evolution of their PL properties. The PL spectra change drastically on a timescale of seconds to minutes upon irradiation. Time traces for the PL intensity were derived by fitting the PL spectra with a Lorentzian lineshape, yielding the temporal evolution of the PL peak parameters.

For these experiments, a circularly polarized Gaussian laser mode was used in order to have the same excitation efficiency for all SWNTs, independent of their orientation. Since the optical transitions in the SWNTs are polarized along their axis, only longitudinal polarization components are absorbed. For circularly polarized excitation, 50% of the overall intensity is polarized along an arbitrary direction. The mean power density of the laser excitation was calculated by relating 50% of the total laser intensity and a circular area with a diameter of 250 nm, corresponding to the FWHM of the laser focus using the 1.4 NA objective. This estimation gives a power density of 10^6 W/cm² for 1 mW incident laser power.

In general, a combination of PL blinking and bleaching was observed, with a bleaching rate strongly depending on the laser intensity. The PL intensity time traces show different kinds of behavior as displayed in Fig. 5.1. For moderate excitation intensities (<100 kW/cm²), pronounced blinking can often be observed (Fig. 5.1a), whereas for stronger excitation a quasi-exponential decay was typical (Fig. 5.1b). Combinations of both (Fig. 5.1c) appear at every intensity level. For the latter two cases, PL decay rates were deduced and correlated with laser intensity, substrate and atmosphere.

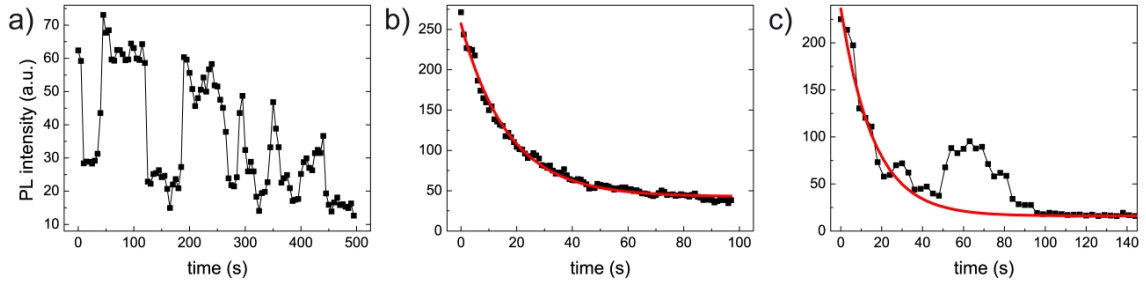


Figure 5.1: Typical time traces showing the temporal evolution of photoluminescence from individual SWNTs under laser irradiation. Very different bleaching dynamics were observed. a) Pronounced blinking behavior with step-like changes corresponding to reversible reactions, mainly at weaker excitation (here: 20 kW/cm^2). b) Pseudo first-order exponential decay without step-like events, usually at stronger excitation (here: 500 kW/cm^2). For this case, decay rates were derived from an exponential fit (red line). c) Combination of exponential decay and some blinking, seen for all excitation intensities (here: 20 kW/cm^2). Decay rates were estimated from exponential fits disregarding reversible changes.

Most of the SWNTs show an overall exponential decay, especially at more intense laser excitation. For each laser intensity ($5 - 2000 \text{ kW/cm}^2$), at least 20 individual SWNTs were probed and decay rates were determined for all cases where a reasonable first-order exponential fit was possible. These rates were finally averaged. The individual decay rates for single nanotubes vary by a factor of 2 for a given laser intensity, substrate and atmosphere, presumably due to the different local environment and defect properties for each nanotube. The averaged decay rates are displayed in Fig. 5.2.

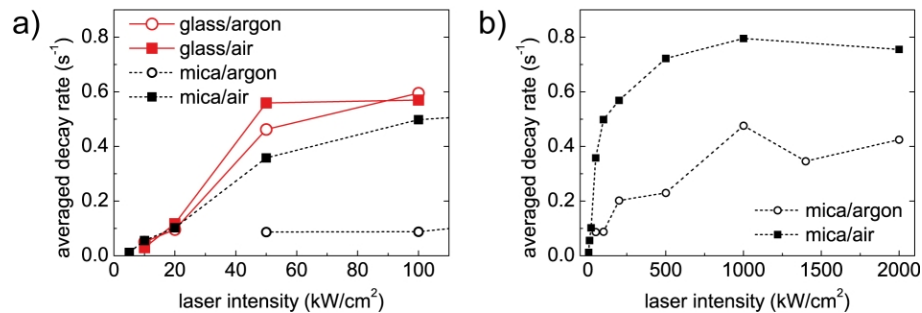


Figure 5.2: Averaged PL decay rates against incident laser intensity for different substrates (glass/mica) and atmospheres (air/argon). Rates were derived from pseudo-first order exponential fits of PL time traces. a) Decay rates for SWNTs on glass increase superlinearly with laser intensity, but are generally too high to be resolved. The depicted points rather display the maximum observable decay rate. Decay rates on mica increase linearly but start to saturate above 50 kW/cm^2 , which can be attributed to limited availability of further O_2 after oxidation of the nanotube by all initially adsorbed O_2 molecules. b) Data for mica in the complete intensity range. Saturation of the decay rate and the stabilizing effect of argon can clearly be seen.

Depending on the laser intensity, the acquisition time for each spectrum of a series which is necessary to obtain PL spectra with adequate signal to noise ratio was 0.5 to 10 seconds. This limits the temporal resolution when monitoring the PL decay, resulting in a maximum observable bleaching rate of about 1 s^{-1} for strongly luminescent nanotubes. At lower laser intensities and/or with weakly luminescent nanotubes, this maximum observable rate is lower.

For SWNTs on a glass substrate, the decay rates are generally too high to be accurately determined with the limited temporal resolution. Low PL intensity even at the beginning of the time traces for these nanotubes indicates an initial fast decay during the acquisition of the first spectrum which can not be monitored. The depicted curves for nanotubes on glass in Fig. 5.2a therefore rather display the maximum observable decay rate at a given laser intensity for weakly luminescent tubes due to fast initial bleaching. The apparent saturation of the rate above 50 kW/cm^2 does not display a nanotube property in this case. Nevertheless, a strong increase of the decay rates with rising laser intensity is evident and not invalidated by limited temporal resolution. A significant influence of argon atmosphere is not visible for samples on a glass substrate.

For SWNTs on a mica surface, higher PL intensities allow for shorter acquisition times and therefore higher temporal resolution leading to a more reliable determination of decay rates. Up to a laser intensity of 50 kW/cm^2 , the decay rate increases linearly, but tends to saturate at higher intensities and finally reaches its maximum at around 1000 kW/cm^2 (Fig. 5.2b). Argon atmosphere further reduces the rate by a factor of about 2, indicating that reduced availability from a reactant in the air, which is believed to be oxygen, limits the bleaching kinetics. The dependence of the bleaching rate on laser intensity shows that the underlying process is strongly photo-induced. The observed bleaching behavior is mainly attributed to irreversible photo-induced chemisorption of initially adsorbed oxygen, which causes hole doping of the nanotube and subsequent PL quenching.

Various bleaching mechanisms have been reported, but not all are relevant for this particular experiment. PL quenching by protonation of adsorbed oxygen in acidic environment [57, 58] is very unlikely, since it requires a pH well below 7 for (6,5)-nanotubes, which can not be induced by the sodium cholate [132]. Further on, the surfactant is not electron-accepting and therefore can not trap photo-excited charges from the nanotube, as it was reported for organic acceptor molecules [121, 128]. The observed PL bleaching in the reported experiments is rather due to a photo-induced oxidation of the nanotube, based on chemisorption of initially adsorbed oxygen [133]. The adsorption of oxygen upon exposure to air is a common phenomenon [129, 134], but physisorption induces only weak hole doping [130]. However, chemisorption of oxygen which is favorable for excited molecules in the singlet state can significantly dope the nanotube and quench PL [58, 130]. Savage *et al.* [133] suggested, that optically excited SWNTs could generate singlet oxygen as it was reported for C_{60} fullerenes. The activation barrier for chemisorption of singlet oxygen is then low enough ($\sim 0.6 \text{ eV}$) to be overcome at room temperature and the process is overall

exothermic [135]. Calculations suggest that the oxygen molecule is split and each atom takes an epoxy position at the nanotube [135]. This epoxy structure is very stable and involves a large charge transfer of about 0.5 electrons to each oxygen atom, thus doping the nanotube and efficiently quenching PL [131]. The high desorption barrier in the range of 1.7 eV makes this chemisorption rather irreversible [135].

For SWNTs on glass substrates, the PL bleaching rate for laser intensities up to 100 kW/cm² is limited by photo-excitation and not by oxygen availability in the surrounding atmosphere, a conclusion drawn from the similar results of the measurement in argon atmosphere. Since all the samples were prepared and stored in ambient conditions and are therefore exposed to oxygen, the SWNTs adsorb oxygen over time. This oxygen is then subsequently chemisorbed during laser irradiation.

For SWNTs on a mica surface, the decay rate increases similar as for glass up to 50 kW/cm², which corresponds to the nanotube oxidation by initially adsorbed oxygen. At higher laser intensities, the decay rate starts to saturate and finally reaches its limit. At high excitation intensity, most of the initial oxidation sites are rapidly used up to oxidize the nanotube at the very beginning of a measurement, so that a slower decay due to the decreasing probability of subsequent oxidation events is observed. The early onset of a limited decay rate indicates a smaller amount of initially adsorbed oxygen for SWNTs on mica compared to nanotubes on glass. Atomic force microscopy measurements reveal a significant surface roughness of the utilized glass cover slides whereas mica is atomically flat. Furthermore, mica is known to be covered by a pronounced water film of several nanometers at ambient conditions [136,137]. Therefore, the SWNTs should be closely attached to the mica surface, possibly also covered by a water layer and thus less exposed to the surrounding atmosphere.

Remarkably, even for strongest laser excitation no additional higher order photo-induced bleaching processes are observed and oxygen availability remains the limiting factor. Several SWNTs on mica together with argon atmosphere maintain a certain level of PL intensity even after very long illumination time. Here, the adsorbed oxygen is completely used up and no further oxygen is available, thus finishing PL decay.

Although all investigated SWNTs lose a substantial amount of their PL intensity upon continuous laser illumination, they nevertheless can be regarded as stable emitters compared to e.g. fluorescent dyes. At high laser intensities, the maximum cycling rate for excitation of the nanotube is roughly 10¹¹ s⁻¹, according to an exciton lifetime of about 10 ps [42,47], neglecting multiple excitation and exciton-exciton annihilation. Regarding the observed maximum PL decay rate of 0.8 s⁻¹, the probability for photo-induced oxidation is thus extremely low.

For SWNTs covered with immersion oil right after sample preparation, which are therefore not exposed to air, virtually no PL decay is observed upon laser irradiation. Here, the maximum number of emitted photons from a single nanotube reaches values of more than 10¹⁰, much higher than recently reported maximum values for luminescent dyes of

about 10^8 [138, 139]. In conclusion, the individual bleaching behavior of a nanotube is interpreted to depend on the oxygen availability in its local environment. Stable emission was e.g. observed for SWNTs grown and illuminated in oxygen-free atmosphere [124], for SWNTs isolated with sodium dodecyl sulfate [122], which are apparently embedded in the surfactant after spin-coating on the sample [48], or for the above mentioned SWNTs immersed in oil. In these cases, the nanotubes have only limited access to oxygen.

To verify that PL decay is due to a limited number of oxidation events and not caused by substantial photo-induced damage of the SWNT, the Raman scattering and PL intensity of a (9,1)-nanotube were simultaneously observed during laser irradiation. For this chirality, both signals can be detected with the excitation at 632.8 nm because the Raman scattered photon energy is resonant with the E_{22} transition. This is not the case for (6,5) SWNTs, where the Raman signal is therefore barely detectable. Selected spectra from a consecutive series and the corresponding intensity time traces of Raman G-Band (at 703 nm) and PL (at around 930 nm) are shown in Fig. 5.3.

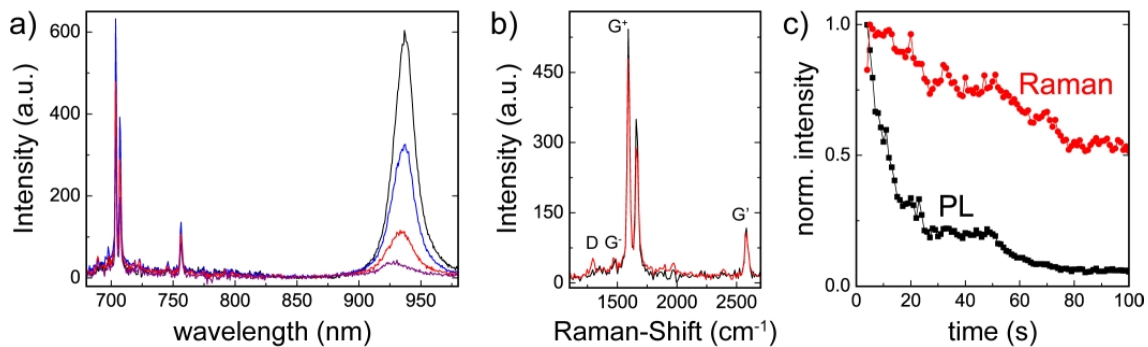


Figure 5.3: Evolution of the Raman and PL intensity during laser irradiation. a) Selected spectra from a series showing the temporal evolution of both Raman scattering (G-Band at 703 nm) and PL (at \sim 930 nm) from a single (9,1)-nanotube under laser irradiation with 1000 kW/cm^2 . b) Detailed view of the Raman bands for the black and red spectrum in a, plotted against Raman-Shift. Upon laser irradiation, a weak D-band appears which indicates the generation of few defect sites. c) Time trace for the Raman G-band and PL intensity. The much faster decay of PL compared to the Raman signal shows that PL is effectively quenched by a limited number of quenching sites without substantial structural damage of the SWNT that would strongly affect its Raman scattering intensity. The strong impact of only few quenching sites on the PL reveals a high exciton mobility.

Whereas PL intensity is strongly decreasing upon laser irradiation, the much slower decay of the Raman signal shows that the structural and electronic properties of the nanotube are altered more slowly and therefore the loss of PL is mainly due to few additional oxidation sites that cause efficient non-radiative recombination of excitons. The emerging Raman D-band (Fig. 5.3b) indicates structural changes of the SWNT, as e.g. covalent bonding of oxygen. The D-band intensity remains weak, which displays a very limited number of defects or quenching sites.

5.2 Evaluation of step-like PL bleaching and blinking

The strong impact of only few quenching sites on the PL intensity is caused by the exciton mobility. The quenching effect of a single hole is extended, because it can be reached by excitons that were generated further away. In a simple approximation, a single hole can "switch off" the PL from a nanotube segment having a length corresponding to the exciton excursion range. The generation of such a single quenching site in a previously unperturbed luminescent SWNT segment is the origin of the discrete steps in the PL time traces.

These steps are mainly observable at low laser intensities up to 100 kW/cm^2 and at the beginning of irradiation, where only few holes are present on the nanotube. When the mean distance of holes near the center of the illumination spot becomes shorter and finally comparable to this range during subsequent oxidation, the quenching impact of additional holes is reduced, giving smaller and finally unresolvable steps [41].

The step-height ΔI is proportional to the actual intensity I (before the step), since the quenching impact of a newly introduced hole scales with the fraction of the nanotube that is still emitting, represented by I . For a small proportionality factor, this relation leads to a first-order exponential PL decay as observed in Fig. 5.1b for high excitation intensity. Here, the initial bleaching process in the center of the nearly Gaussian illumination spot, accompanied by apparent steps and blinking, cannot be observed due to limited temporal resolution. Subsequent oxidation events outside the laser spot center will have much smaller impact, corresponding to a lower value of $\Delta I/I$ which then leads to a smooth exponential decay.

All pronounced steps in the PL time traces for excitation intensities up to 100 kW/cm^2 were evaluated and the absolute step-height $|\Delta I|$ was then correlated with the initial intensity I before or after the step, depending on whether the PL decreased or increased. Fig. 5.4 shows the correlation for SWNTs on either glass (Fig. 5.4a) or mica (Fig. 5.4b). A linear fit gives a proportionality factor $|\Delta I|/I$ of 0.38 for both substrates. Fig. 5.4c and d show histograms of the relative step height distribution, taking into account also the sign of the PL intensity change. The asymmetry in the number of steps decreasing or increasing the PL intensity (65%/35%) demonstrates that the observed oxidation process is preferentially irreversible, leading to a PL bleaching in the long term. The similarity of the data for glass and mica is evident and confirms that the PL decay mechanism is the same for both substrates at low laser intensity, namely the oxidation of the nanotube by initially adsorbed oxygen molecules.

From the proportionality factor, the exciton excursion range can be estimated since this factor corresponds to the quenched fraction of the nanotube segment in which PL is excited and detected. The weighted excitation area is described by a Gaussian profile with a full width at half maximum of 250 nm, according to the laser focus size. In order to observe

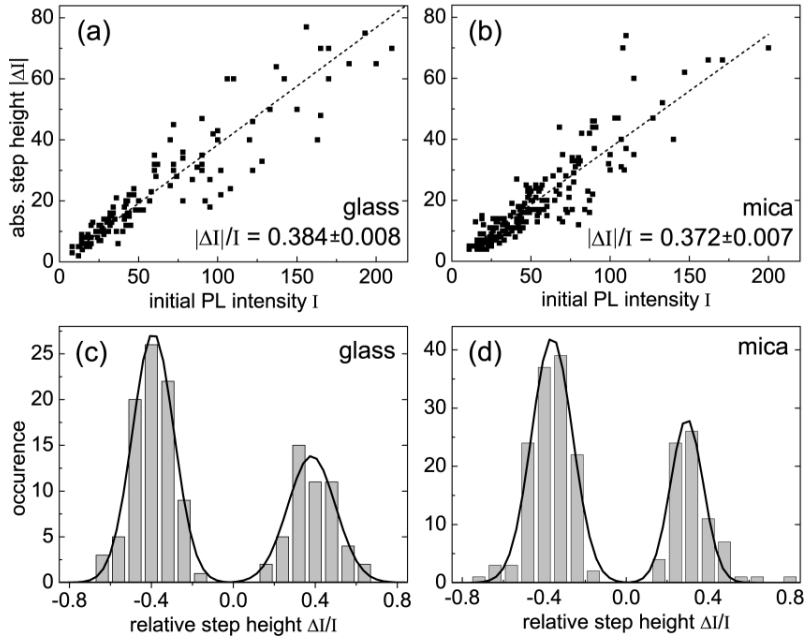


Figure 5.4: Evaluation of step-like changes in the PL time traces on glass and mica substrates. The correlation between absolute step-height and initial PL intensity (upper value before/after step) reveals the linear relation $|\Delta I|/I \approx 0.38 \pm 0.01$ for both glass (a) and mica (b). This supports the idea of individual quenching sites formed by holes switching off luminescence in a nanotube segment whose length corresponds to the exciton excursion range. From the observed slope of the linear fit, the excursion range is determined as 105 nm. c) and d) show the distribution of relative step height $\Delta I/I$ with an apparent asymmetry regarding the number of steps going down ($\sim 65\%$) or up ($\sim 35\%$). This demonstrates that the observed oxidation process is preferentially irreversible.

a 38% decrease in PL intensity, a section of 105 nm has to be quenched, which gives an estimation for the exciton excursion range. This derivation is very basic and neglects that the quenching efficiency strongly depends on the distance to the quenching site, i.e. is not a rectangular function as assumed here. A detailed discussion of exciton diffusion and a more accurate determination of the exciton diffusion length based on the $|\Delta I|/I$ ratio is given in the following chapter 6, yielding a value of 100 nm.

The value of 105 nm is in good agreement with the observation of Cognet *et al.* [41], who reported values of 90-100 nm for nanotube diameters of 0.7-0.8 nm, where (6,5)-SWNT are included. They also derived this value using the very simple picture of a segment which is "switched off" and defined its length as the exciton excursion range. Similar observations and conclusions have been reported for other extended one-dimensional systems, such as fluorescent conjugated polymer chains [140, 141]. Step-like blinking of fluorescence was attributed to localized quenching of mobile excitons with a migration length of about 400 nm [141].

Conclusion

This chapter presented results on the photo-induced blinking and PL decay from individual SWNTs on either glass or mica substrates. The PL decay can be attributed to photo-induced chemisorption of initially adsorbed oxygen at the nanotube which introduces free holes that subsequently quench mobile excitons. The PL decay rate on glass strongly increases with laser intensity, but is generally too fast to be resolved. The process is limited by excitation and the probability for photo-induced oxidation. For mica substrates, the decay rate increases similarly at low laser intensities, but above 50 kW/cm^2 saturates and reaches a maximum value at 1000 kW/cm^2 . This saturation is attributed to a smaller amount of initially adsorbed oxygen caused by the different surface properties of mica and glass. At the beginning of laser irradiation, this oxygen is quickly consumed to oxidize the nanotube, resulting in slower decay due to limited availability of further oxidation sites.

When oxygen adsorption is avoided during sample preparation and storage, SWNTs are very stable PL emitters compared to e.g. fluorescent dyes. For SWNTs surrounded with immersion oil and therefore not exposed to air, virtually no PL bleaching occurs and the number of emitted photons from a single nanotube can easily exceed 10^{10} .

The simultaneous detection of Raman scattering during the PL bleaching process shows that only few structural defects are introduced, which nevertheless dramatically reduce the PL. The strong impact of only few quenching sites on the PL intensity reveals a high exciton mobility in SWNT. The quenching effect of a single hole is extended, because it can be reached by excitons that were generated further away. The evaluation of step-like changes in the PL time traces, related to single oxidation events, allowed for a determination of the exciton excursion range, which was estimated to be 105 nm.

Since the publication of these results in 2008, several other groups have also studied exciton mobility in different SWNT samples [38, 60, 142–145]. The reported exciton excursion ranges vary from 6 nm to 860 nm, strongly depending on the sample properties, which is discussed in more detail in section 7.4. The values of $L = 100 - 170 \text{ nm}$ for nanotubes dispersed with different surfactants and spun onto a substrate [142], similar to the samples studied in this work, agree very well to the 105 nm determined here.

6 Exciton diffusion - analytical and numerical treatment

The photoluminescence bleaching experiments in the previous chapter have shown that excitons in SWNTs are highly mobile and that this mobility has important consequences for the PL properties. For the understanding of PL experiments and the analysis of near-field images, an adequate description of exciton mobility is needed. This chapter introduces the analytical and numerical calculation of the exciton distribution in SWNTs, resulting from their mobility and the interaction with quenching defects. The numerical calculations are used to evaluate the PL blinking results from chapter 5 and derive the exciton excursion range in a more accurate way. Afterwards, it is shown how the numerical model can be extended to simulate the TENOM imaging process, which is necessary to describe and understand near-field PL images. The following section then introduces a modification to the model, which accounts for exciton energy variations along the SWNT leading to an additional driving force. Thereby, exciton localization as observed in chapter 8 can be explained. The last two sections show that the model can also be used to describe time-resolved PL experiments and study the influence of quantum yield and exciton mobility on the signal enhancement in a TENOM experiment.

In the following, excitons are treated as rigid quasi-particles that move along the one-dimensional SWNT. The small exciton size and their short coherence length discussed in section 2.2.4 can be neglected with respect to the much larger nanotube length and excursion range. Hence, their position is described by the center-of-mass. Excitons are completely delocalized along the SWNT circumference and their mobility is thus purely one-dimensional along the SWNT axis. It was suggested that exciton mobility can be described as simple 1D diffusion [41, 146], which is the basis of the following analytical and numerical treatment.

6.1 Analytical description

Diffusion can be generally described by Fick's second law. If $N(x, t)$ is the exciton density at time t with the position along the SWNT denoted as x , this has the form

$$\frac{\partial N(x, t)}{\partial t} = D \frac{\partial^2 N(x, t)}{\partial x^2}. \quad (6.1)$$

Here, D is the diffusion coefficient. This equation does not yet take into account exciton decay. This is a first order process with a rate $k = 1/\tau$ including the radiative and non-radiative decay rates as introduced in section 2.3. Then, τ is the effective exciton lifetime. The diffusion equation is extended to

$$\frac{\partial N(x, t)}{\partial t} = D \frac{\partial^2 N(x, t)}{\partial x^2} - \frac{N(x, t)}{\tau}. \quad (6.2)$$

If a single exciton is considered at position $x = 0$ and time $t = 0$, the probability to find the exciton at a position x evolves with time as

$$N(x, t) = \frac{1}{\sqrt{2\pi\sqrt{2Dt}}} \exp\left(-\frac{x^2}{4Dt}\right) \exp\left(-\frac{t}{\tau}\right) \quad (6.3)$$

which is a Gaussian distribution with a standard deviation of $\sqrt{2Dt}$. The probability to find the exciton somewhere is $\int N(x, t) dx = \exp(-t/\tau)$ which is the overall mono-exponential decay observed for the integrated exciton population in SWNTs [42, 147].

At $t = \tau$, the distribution has a standard deviation of $\sqrt{2D\tau}$, which is defined as the exciton diffusion length L hereafter.

$$L = \sqrt{2D\tau} \quad (6.4)$$

The FWHM of the distribution at $t = \tau$ is $2\sqrt{2\ln 2} \cdot L \approx 2.355 \cdot L$. One can say that a single exciton can probe a length of about $\pm L$ during its lifetime, which explains the extreme sensitivity of SWNT photoluminescence to only few quenching defect sites.

In an experiment where the nanotube is excited with a continuous laser, the system is described by a steady-state solution with $\partial N/\partial t = 0$. The continuous excitation by a laser is included as a source term $\sigma(x)$ related to its intensity distribution. In this case, eq. 6.2 transforms to

$$0 = D \frac{\partial^2 N(x, t)}{\partial x^2} - \frac{N(x, t)}{\tau} + \sigma(x). \quad (6.5)$$

Considering the simple case of a single quenching site at $x = 0$ and an excitation $\sigma(x)$ which is constant along the SWNT, e.g. if the laser focus is much larger than L , this steady-state ansatz can be analytically solved. It is $N(0, t) = 0$ at all times due to the quenching site and $\sigma(x) = \sigma$. The solution is then

$$N(x) = \sigma\tau \left[1 - \exp\left(-\frac{|x|}{L/\sqrt{2}}\right) \right]. \quad (6.6)$$

The fraction of excitons ΔN that are quenched by the defect with respect to the unperturbed exciton density $N = \sigma\tau$ is

$$\Delta N = \int (N(x) - \sigma\tau) dx = -\sqrt{2}L\sigma\tau. \quad (6.7)$$

Assuming that a nanotube length l is excited by a laser with constant intensity along this length, the detected PL intensity without the defect would be $I_0 \propto l\sigma\tau$. When a single

quenching site is introduced, the PL intensity is reduced by $\Delta I \propto \sqrt{2}L\sigma\tau$. If the PL reduction upon generation of a single quenching site is measured in an experiment and the illuminated length of the SWNT is known and spatially homogeneous, then L can be determined from $\Delta I/I_0 = \sqrt{2}L/l$.

This could be applied to the results obtained from the blinking experiments in chapter 5, where $\Delta I/I_0 = 0.38$ was found, and $l = 250$ nm could be used based on the laser focus size. In this case, the exciton diffusion length would be determined as 70 nm. However, the tightly focused laser excitation is spatially very inhomogeneous on a length scale of L , since the focus size is small. Therefore, a more accurate calculation must include the laser intensity distribution $\sigma(x)$ as e.g. a Gaussian function with a FWHM of 250 nm. The steady-state ansatz would then be modified to

$$0 = D \frac{\partial^2 N(x, t)}{\partial x^2} - \frac{N(x, t)}{\tau} + \sigma \exp\left(-\frac{x^2}{w^2}\right) \quad \text{with} \quad w = \frac{\text{FWHM}}{2\sqrt{\ln 2}}. \quad (6.8)$$

This equation however has no simple analytical solution that could be easily calculated. A numerical treatment of this problem is more feasible and can then be used for arbitrary excitation profiles such as the donut mode and tip-enhanced excitation in the TENOM experiments.

6.2 Numerical simulation

For the numerical treatment of the diffusion equation 6.2, x and t are discretized using step widths of Δx and Δt , and the derivatives $\partial N/\partial t$ and $\partial^2 N/\partial x^2$ are expressed as differential quotients.

$$\frac{\partial N(x, t)}{\partial t} = \frac{N(x, t + \Delta t) - N(x, t)}{\Delta t} \quad (6.9)$$

$$\frac{\partial^2 N(x, t)}{\partial x^2} = \frac{N(x - \Delta x, t) - 2N(x, t) + N(x + \Delta x, t)}{\Delta x^2} \quad (6.10)$$

The relation between the step widths Δx and Δt is defined as

$$\Delta x = \sqrt{2D\Delta t}, \quad (6.11)$$

similar to eq. 6.4. The diffusion equation including the exciton decay term can then be written in the following discrete form

$$N(x, t + \Delta t) = \frac{1}{2}[N(x - \Delta x, t) + N(x + \Delta x, t)] - \frac{\Delta t}{\tau} N(x, t). \quad (6.12)$$

This means that the exciton population at $t + \Delta t$ is generated by half of the population from its left and right neighboring positions at time t , reduced by the exciton decay. In other words, during each time step Δt half of the exciton population at each position is transferred to the left and right neighboring position, respectively. This resembles a 1D random walk where the probability for a particle to hop one step left or right is 50%

each. In the numerical calculations described here, the probability distribution for a single exciton and its evolution with time is evaluated, corresponding to the statistical average of all possible paths in a 1D random walk. The diffusion constant defines the displacement Δx during each time step according to eq. 6.11. To reduce the input parameters, the diffusion length L is used instead of the diffusion constant D and the effective exciton lifetime τ . Combining eqs. 6.4 and 6.11, the step widths can be related as

$$\frac{\Delta x}{L} = \sqrt{\frac{\Delta t}{\tau}}. \quad (6.13)$$

Instead of using the steady-state ansatz with $\partial N/\partial t = 0$, a single excitation cycle is calculated, i.e. the evolving probability distribution for a single exciton. The excitation profile $\sigma(x)$ gives the initial exciton distribution $N(x,0)$ and the temporal evolution is then calculated until $t \approx 2.5\tau$, when N has nearly vanished due to the decay term. The steady-state exciton distribution $N_{ss}(x)$ that is relevant for the experiment with continuous excitation and time-integrated PL detection, is simply the sum of $N(x,t)$ over all time steps.

$$N_{ss}(x) = \sum_t N(x,t) \quad (6.14)$$

The equivalence of this approach to a steady-state ansatz can be shown as follows. A time integration of the diffusion equation 6.2 yields

$$\int_{t=0}^{\infty} \frac{\partial N(x,t)}{\partial t} dt = \int_{t=0}^{\infty} \left(D \frac{\partial^2 N(x,t)}{\partial x^2} - \frac{N(x,t)}{\tau} \right) dt. \quad (6.15)$$

Using the Leibniz integral rule, this can be written as

$$N(x, \infty) - N(x, 0) = D \frac{\partial^2}{\partial x^2} \int_{t=0}^{\infty} N(x,t) dt - \frac{1}{\tau} \int_{t=0}^{\infty} N(x,t) dt. \quad (6.16)$$

With $N(x, \infty) = 0$, $N(x, 0) = \sigma(x)$ and $N_{ss}(x) = \int N(x,t) dt$, the equation transforms to

$$0 = D \frac{\partial^2 N_{ss}(x)}{\partial x^2} - \frac{1}{\tau} N_{ss}(x) + \sigma(x), \quad (6.17)$$

which is equivalent to the steady-state ansatz in eq. 6.5.

It is important to note that exciton-exciton annihilation is not considered here. It is assumed that only one exciton is present at a time, which validates the equivalence of steady-state and time-integrated approach. For the excitation powers used in the experiments, exciton-exciton annihilation can be neglected. It becomes only relevant at high power pulsed excitation.

Using the eqs. 6.12, 6.13 and 6.14, the steady-state exciton distribution for any excitation profile $\sigma(x)$ and a given diffusion length L can be calculated. The PL intensity measured in the experiment is

$$I_{PL} = k_{rad} \Delta t \sum_x \sum_t N(x,t) = k_{rad} \Delta t \sum_x N_{ss}(x) = QY \frac{\Delta t}{\tau} \sum_x N_{ss}(x) \quad (6.18)$$

because the detection is time integrated (acquisition times >10 ms) and also spatially integrated due to the detection area being much larger than the excitation spot. In the experimental setup, there is no confocal pin-hole which limits the detection area. Instead of defining k_{rad} and τ , the quantum yield QY is used as a further input parameter. It is usually set to 10^{-3} , a typical value for SWNTs from aqueous suspensions [50, 52, 101]. Its value has no direct influence on the exciton and PL distribution and only scales the simulated PL intensity.

Connection to the far-field PL bleaching experiments

The numerical calculations can now be used to determine the exciton diffusion length from the results of the observed blinking in chapter 5. The actual excitation profile can be used and the diffusional process is accurately described. The laser spot size of 250 nm was determined from the resolution in the PL images. It is the FWHM of the PL distribution across an individual SWNT, i.e. the width of the SWNT in the image. For the excitation profile $\sigma(x)$ used in the simulation, the width of the laser spot along the SWNT is relevant, which is slightly larger. The longitudinal polarization component exciting the SWNT has a similar distribution as the focused linearly polarized laser mode, which is elongated in polarization direction [8]. Based on ref. 8, the FWHM of the laser excitation along the SWNT is calculated as 275 nm. The detected PL intensity using a Gaussian excitation profile with this FWHM can then be simulated with and without a single quenching site at $x = 0$ where $N(0, t) = 0$ for all times. The relative PL decrease $\Delta I/I_0$ depends on the diffusion length L which is the only variable parameter in the simulation. For the step width Δx , a value of 3 nm is used which then determines the ratio $\Delta t/\tau$ via eq. 6.13 and the number of simulated time steps ($\approx 2.5\tau/\Delta t$).

In order to reproduce the experimental value of $\Delta I/I_0 = -0.38$, a diffusion length of $L = 100$ nm is necessary. This value is very close to the simple estimation in chapter 5, which neglected the actual exciton diffusion process. The value is much larger than the 70 nm determined by the analytical steady-state solution and assuming a rectangular excitation profile. This shows that for tightly focused excitation, its spatial distribution has to be considered.

In summary, a numerical model has been developed which allows for the accurate description of the exciton diffusion process taking also into account the spatial distribution of the strongly focused laser excitation. Based on this model, a diffusion length $L = 100$ nm can be derived from the far-field PL bleaching experiments reported in chapter 5.

This diffusion length can then be used as an input parameter for the numerical simulation of near-field PL images. The following section describes the further development of the numerical model, that allows for the simulation of TENOM experiments and a quantitative evaluation of experimental near-field PL images.

6.3 Numerical simulation of the TENOM imaging process

The numerical calculation described so far can be used to calculate the detected PL intensity for a particular excitation profile with a fixed position relative to the SWNT. This corresponds to the acquisition of the PL signal at one pixel in the experiment. An image is formed by raster scanning the sample, i.e. the SWNT, with respect to the exciting laser focus. The same can be done in the simulation. If the spatial distribution of the laser excitation is $I_{exc}(x, y)$ and x', y' are the coordinates describing the offset between the excitation spot and the SWNT center for each image pixel, the initial exciton distribution $\sigma(x)$ is given by

$$\sigma(x) = I_{exc}(x - x', -y'). \quad (6.19)$$

The PL intensity at each pixel is then

$$I_{PL}(x', y') = QY \frac{\Delta t}{\tau} \sum_x N_{ss}(x, x', y') \quad (6.20)$$

with a different steady-state exciton distribution $N_{ss}(x, x', y')$ for each x', y' .

In the TENOM experiments, the tip strongly modifies the excitation but also the detection and the exciton decay. The enhanced excitation underneath the tip is included as an additional component in the intensity distribution $I_{exc}(x, y)$. It is modeled as a narrow Gaussian with a FWHM according to the tip diameter of 15 – 35 nm, and an amplitude which is increased by a factor of f^2 compared to the far-field excitation, according to the definition in section 3.3.2.

$$I_{exc}^{tip}(x, y) = I_{exc}(x, y) + f^2 \exp\left(-4 \ln 2 \frac{x^2 + y^2}{FWHM^2}\right) \quad (6.21)$$

The detection and exciton decay is modified by the tip due to its influence on the decay rates k_{rad} and k_{nr} . Since the non-radiative rate is intrinsically very high for SWNTs, it is not substantially increased by the tip. This is very different for single dye molecules with a high quantum yield, where significant quenching at nanometer tip-sample distances occurs [100, 148].

The radiative rate can be strongly increased underneath the tip and thus varies along the SWNT. The spatial dependence of k_{rad} is modeled similar to the excitation. It is enhanced by a factor of f_{rad}^2 with a narrow Gaussian distribution underneath the tip.

$$k_{rad}(x, x', y') = k_{rad}^0 \left[1 + f_{rad}^2 \exp\left(-4 \ln 2 \frac{(x - x')^2 + y'^2}{FWHM^2}\right) \right] \quad (6.22)$$

This spatial dependence leads to relative changes of $\tau = (k_{rad} + k_{nr})^{-1}$ and $QY = k_{rad}\tau$ which are calculated as a function of x, x' and y' . The detected PL intensity at each pixel including the tip enhanced rates in a TENOM experiment is then

$$I_{PL}(x', y') = \sum_x QY(x, x', y') \frac{\Delta t}{\tau(x, x', y')} N_{ss}(x, x', y'). \quad (6.23)$$

The SWNTs in the simulations are always straight and oriented along the x-direction. Their finite length l leads to $0 \leq x \leq l$ and the two SWNT ends are regarded as efficient quenching sites, i.e. $N(0, t) = N(l, t) = 0$ for all time steps. This quenching is due to localized states within the bandgap arising from dramatic band modifications related and confined to the ends [149–152]. The far-field excitation $I_{exc}(x, y)$ is given by the x-polarized component E_x^2 of the focused radially polarized donut mode as shown earlier in Fig. 4.2b and calculated according to ref. 8. Its amplitude is normalized to 1.

Fig. 6.1 shows an experimental near-field PL image for a 200 nm long SWNT and the respective simulated image. The excitation and radiative rate enhancement f^2 and f_{rad}^2 underneath the tip were both set to a moderate value of 4 to reproduce the experimental image contrast with clearly visible far-field contributions. The two weak side-lobes correspond to the field components of the laser focus polarized along the nanotube axis, convoluted with a short luminescent nanotube. The tip diameter used for the calculation was taken as the FWHM of the near-field signal across the SWNT, here 20 nm. The near-field signal induced by the tip is shifted by about 70 nm from the center, because the tip was not ideally centered in the focus. Taking this into account for the excitation intensity distribution $I_{exc}^{tip}(x, y)$, the image can be well reproduced.

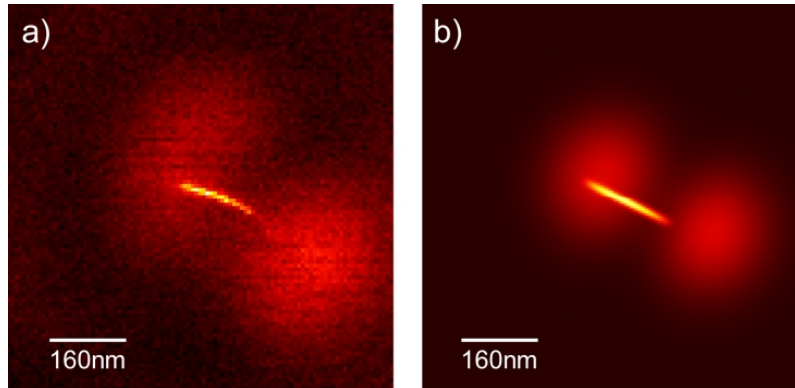


Figure 6.1: a) Experimental and b) simulated near-field PL image of a short luminescent nanotube with 200 nm length. Due to the moderate field enhancement of this tip, the two side-lobes from the far-field background are clearly visible. This pattern arises from the polarization components parallel to the nanotube in the radially polarized laser focus (compare Fig. 4.2b). The near-field is slightly off-center, because the tip was not perfectly centered in the focus but shifted by about 70 nm. The experimental image can be well reproduced by the simulation, including the fade-out of PL towards the end which is a direct consequence of exciton mobility.

The fade-out of the near-field PL towards the ends is an indication of exciton mobility. A fraction of the excitons generated near the ends at a distance below their diffusion length can reach the ends and get quenched. This significantly reduces the detected PL intensity already for an excitation 50 nm away from the end. The gradual decrease towards the

ends is apparent in the images and is in good agreement with the simulation based on a diffusion length of 100 nm.

As can be seen from the images in Fig. 6.1, signal enhancement factors derived from far-field to near-field ratios at a single sample position are not well defined. In particular for short 1D structures (<700 nm), the effects of far-field excitation pattern and exciton mobility strongly affect the local ratios. Simulating the imaging process allows to determine more reliable values.

6.4 Simulation of exciton diffusion in an inhomogeneous environment

It has been previously observed, that the PL energy and thus exciton energy can be strongly inhomogeneous along an individual SWNT [153]. These variations can result from an inhomogeneous DNA-wrapping which only locally lowers the exciton energy by the screening effect. It can be expected that these energy gradients modify the exciton diffusion as they introduce a directed driving force towards energy minima, similar to electric fields acting on charge carriers. To account for this effect, the diffusion equation 6.2 is extended by a drift term which leads to

$$\frac{\partial N(x, t)}{\partial t} = D \frac{\partial^2 N(x, t)}{\partial x^2} - \frac{\partial [A(x)N(x, t)]}{\partial x} - \frac{N(x, t)}{\tau} \quad (6.24)$$

with a position dependent drift coefficient $A(x)$ that is connected to the local energy gradients. This equation is known as Fokker-Planck equation, apart from the decay term. It is a common ansatz to describe the distribution of particles following a combined diffusion and drift.

In the numerical model developed in this work, the case of a non-uniform exciton energy E_{exc} along the nanotube is implemented by a modified branching ratio. As discussed earlier, the exciton motion is modeled similar to a 1D random walk, where the probability for the particle to move one step left or right during one timestep is 50% each. In the calculation of the exciton distribution according to eq. 6.12, the exciton population is transferred equally to its left and right neighboring positions. For non-uniform exciton energy, this ratio is modified and the probability for the exciton to move towards lower energy is increased. The probabilities $\overleftarrow{p}(x)$ and $\overrightarrow{p}(x)$ with $\overrightarrow{p}(x) + \overleftarrow{p}(x) = 1$ are introduced, describing the fraction of exciton population at position x that is transferred to left or right, respectively. Since the diffusion is temperature driven, the ratio of both probabilities is given by the Boltzmann factor

$$\frac{\overrightarrow{p}(x)}{\overleftarrow{p}(x)} = \exp\left(-\frac{\Delta E_{exc}(x)}{kT}\right) \quad (6.25)$$

with $\Delta E_{exc}(x)$ being the exciton energy difference between the right and left vicinity of position x . Using these definitions, the exciton population is then calculated by

$$N(x, t + \Delta t) = \vec{p}(x - \Delta x)N(x - \Delta x, t) + \overleftarrow{p}(x + \Delta x)N(x + \Delta x, t) - \frac{\Delta t}{\tau}N(x, t). \quad (6.26)$$

It can be shown that this ansatz corresponds to the Fokker-Planck ansatz in eq. 6.24. For sufficiently small Δx , discretizing this equation yields

$$N(x, t + \Delta t) = \left(\frac{1}{2} + \frac{1}{2} \frac{\Delta t}{\Delta x} A(x - \Delta x) \right) N(x - \Delta x, t) + \left(\frac{1}{2} - \frac{1}{2} \frac{\Delta t}{\Delta x} A(x + \Delta x) \right) N(x + \Delta x, t) - \frac{\Delta t}{\tau} N(x, t). \quad (6.27)$$

This is equivalent to eq. 6.26 if

$$A(x) = \frac{\Delta x}{\Delta t} \left[\frac{1 - \exp(\Delta E_{exc}/kT)}{1 + \exp(\Delta E_{exc}/kT)} \right] = \frac{D}{\Delta x} [\vec{p}(x) - \overleftarrow{p}(x)] \quad (6.28)$$

which links the drift coefficient to the exciton energy variations and the diffusion coefficient. Sufficient exciton energy gradients thus create a significant driving force which influences the diffusion and leads to directed exciton transport.

Fig. 6.2 illustrates the numerical calculation of directed exciton diffusion due to spatial exciton energy variations. The exciton population, represented by bars, is increased at the energy minima because of enhanced diffusion towards lower energy.

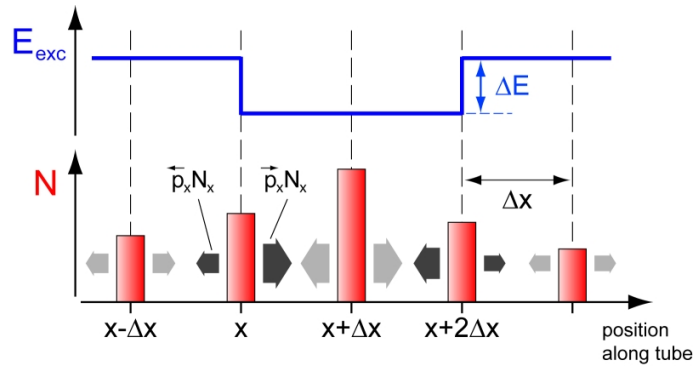


Figure 6.2: Illustration of the numerical calculation of exciton diffusion in an inhomogeneous environment. At each discrete position along the nanotube ($x, x + \Delta x, \dots$) the local exciton population N is represented by a bar. The non-uniform exciton energy E_{exc} is shown above. At each simulation timestep, the population at a position is transferred to its left and right neighbor according to eq. 6.25, indicated by broad arrows. If E_{exc} is different for the two neighboring positions, a higher fraction is transferred to the lower energy side.

This modified model accounting for exciton energy variations will be used in chapter 8 to simulate the exciton distribution near energy minima and support the experimental observation of exciton localization.

6.5 Modeling of time-resolved experiments

The numerical modeling presented so far is based on calculating the temporal evolution of the exciton distribution. For the simulation of time-integrated experiments with continuous excitation this is then integrated over time. Considering the description of time-resolved experiments with pulsed excitation, the model can be readily used by just skipping the temporal integration. In the following, it will be shown that the influence of nanotube ends and defects on the effective overall lifetime τ can be described and that time-resolved TENOM experiments will be strongly affected by exciton diffusion, relying on modeling to evaluate experimental results.

Fig. 6.3a plots the temporal evolution of the exciton distribution $N(x, t)$ in a 400 nm long SWNT after homogeneous excitation ($N(x, 0) = 1$). A diffusion length $L = 100$ nm was used. It can be seen that the exciton decay is much faster near the ends due to the quenching. Furthermore, the influence of the ends propagates towards the center as time evolves. This is a result of diffusion, which transports excitons to the quenching ends. The intrinsic lifetime τ can only be expected to dominate the decay in the center of the SWNT. In a far-field time-resolved PL experiment, used to measure PL lifetimes of individual SWNTs, the detected PL is spatially averaged [42]. For the example in Fig. 6.3a, the overall PL decay time then would be about 0.75τ , significantly smaller than the intrinsic lifetime.

The influence of the ends on the effective lifetime increases for shorter SWNTs, because a larger fraction of the nanotube is then affected by the ends. The numerical simulation can be used to calculate this dependence of PL lifetime and SWNT length, taking also the spatially inhomogeneous excitation by a tight laser focus into account. For the case of uniform excitation, an analytical solution can also be found [60, 154]. The results are plotted in Fig. 6.3b for constant excitation along the whole SWNT (dashed line) and the case of a Gaussian laser focus with a FWHM of 275 nm centered on the SWNT (black line). The latter is more realistic for experiments on individual SWNTs using a confocal laser scanning microscope. For nanotubes shorter than 600 nm, the measured effective lifetime is strongly decreased and the intrinsic lifetime can only be measured for very long SWNTs which are excited in the center. This effect of reduced exciton lifetime for short nanotubes has been observed experimentally using length-fractionated SWNTs [60, 154–156]. From this data, the diffusion length L can be determined by calculating and fitting the length dependence with a variable L . Additional defects besides the ends could also be included in the simulation. They effectively separate SWNT segments and the PL decay is then similar to that from a SWNT with the same length as the defect distance.

It would be interesting to image the local exciton decay time with higher spatial resolution and directly visualize the faster decay near ends and defects. For long SWNTs, some difference can already be expected for diffraction limited excitation in the center and near the ends. However, the effect will be rather small due to the spatial averaging. Collecting

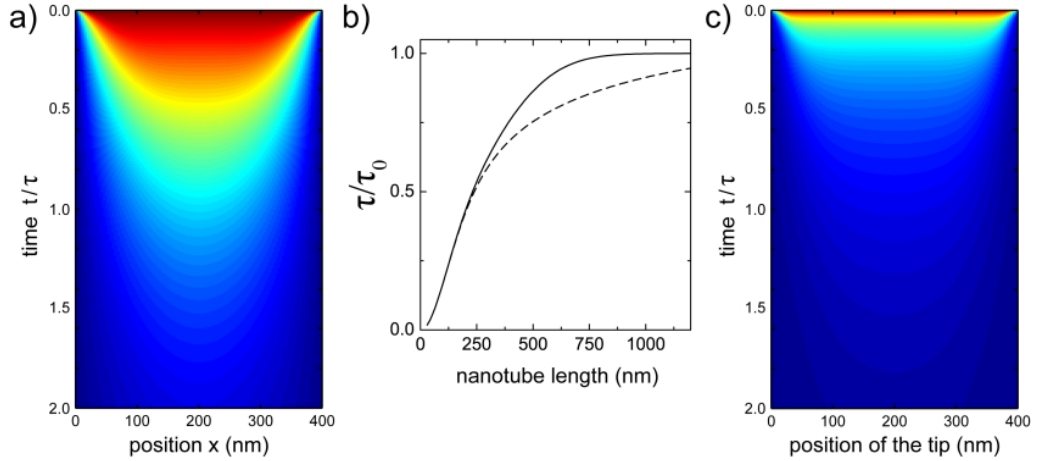


Figure 6.3: Simulation of the time-resolved exciton distribution and PL in a 400 nm long SWNT with a diffusion length $L = 100$ nm. a) Evolution of the exciton distribution after homogeneous excitation with $N(x, 0) = 1$. The decay is faster near the nanotube ends due to quenching and the influence of the ends propagates towards the center. b) Calculated dependence of the averaged effective lifetime τ on the SWNT length. The excitation was either homogeneous (dashed line) or a Gaussian laser focus (FWHM = 275 nm) centered on the tube (black line). The effective lifetime is strongly decreased for tubes shorter than 600 nm and the intrinsic lifetime τ_0 can only be measured for very long SWNTs. c) Evolution of the detected PL in a time-resolved TENOM experiment. The time dependent PL intensity is plotted as a function of the tip position on the nanotube. The observed PL decay is very fast, but this does not reflect the effective lifetime τ . It is dominated by exciton diffusion. The high exciton density gradients near the tip are quickly reduced by diffusion, thereby depleting the exciton population at the tip and decreasing the tip enhanced PL. Time-resolved TENOM experiments can therefore not be evaluated without considering diffusion.

the PL spatially selective by using an aperture SNOM probe could be feasible, but will be hampered by low detection efficiency and thus signal-to-noise problems. The realization of time-resolved TENOM experiments seems very promising, but numerical simulations show some interesting consequences of the tip-enhanced excitation and probing.

Fig. 6.3c plots the temporal evolution of the detected photoluminescence $I_{PL}(x', t)$ as a function of the tip position on the 400 nm long nanotube. It can be seen that the initial PL decay in the first few ps is much faster than the intrinsic lifetime τ , but this does not display such a fast exciton decay. For the low quantum yield of 10^{-3} assumed here, the lifetime is not significantly reduced by the tip-induced rate enhancements. The observed PL decay is dominated by exciton diffusion. The high exciton density gradients near the tip arising from the local excitation are quickly reduced by diffusion, which drives the excitons away from the tip. Thereby the population is depleted at the tip and decreases the tip enhanced PL rapidly. It is thus very difficult to deduce the intrinsic decay rate at a certain SWNT position when using such a tip-enhanced approach. It becomes clear that time-resolved TENOM experiments can not be evaluated without considering diffusion and

rely on numerical simulations of the measurements to extract meaningful results. Apart from that, the fast PL decay times predicted by the modeling require a higher temporal resolution compared to the far-field experiments, which might be problematic.

6.6 Influence of quantum yield and exciton mobility on the near-field PL enhancement

The numerical modeling of TENOM experiments introduced in section 6.3 can also be used to study the interplay of near-field enhancement, quantum yield and exciton mobility. This has important consequences for the applicability of TENOM for other nanoscale emitters than SWNTs.

As it was already discussed in section 3.3.2, the PL intensity enhancement is more efficient for low quantum yield emitters, because the ratio of radiative to non-radiative rate can be significantly increased by the tip. This is different for an intrinsic QY close to unity, which can not be enhanced further. In this case, only the increased excitation rate gives rise to an enhanced PL intensity. Moreover, modifications of the non-radiative rate by the tip can even efficiently reduce the QY and thus quench the PL at close tip-emitter distances [100, 148].

On the other side, the mobility of the excited states allows them to leave the tip interaction range and they are thus not affected by enhanced decay rates. In case of low QY systems, exciton diffusion lowers the effective PL enhancement, since many of the excitons generated by the tip diffuse away and will not encounter an increased radiative rate. This is not the case for high QY systems, where the PL enhancement can benefit from diffusion because the leaving excitons do not undergo quenching by the tip.

The influence of diffusion and quantum yield on the PL enhancement was simulated for two infinite 1D systems with a QY of 0.001 and 0.95, respectively. A 1D system with high QY could for example be J-aggregates [157]. The excitation rate enhancement was set to $f^2 = [5, 10, 20, 50]$ and the radiative rate enhancement was $\frac{1}{2}f^2$ as it is typically lower for emission in the near-infrared [102]. The non-radiative rate was increased by the same value, i.e. $\Delta k_{nr} = \Delta k_{rad} = \frac{1}{2}f^2 k_{rad}^0$ and has the same spatial distribution. The ratio of detected near-field PL signal I_{PL}^{tip} to far-field signal I_{PL}^{ff} without tip was calculated and the results are plotted in Fig 6.4.

It is apparent that the overall enhancement for low QY systems is much larger due to the efficient radiative rate enhancement. The diffusion has a strong influence in this case and significantly lowers the enhancement by up to 70% for $L = 100$ nm.

For the system with a quantum yield near unity, the influence of the tip decreases the QY and the overall enhancement is rather small. The influence of diffusion is not very

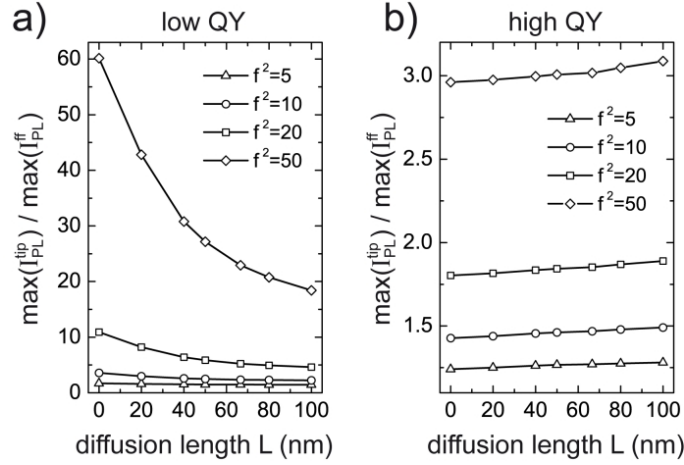


Figure 6.4: Calculated PL signal enhancement for 1D systems with low (a) and high QY (b) depending on the exciton diffusion length and the field enhancement factor f at the tip. The excitation and radiative rate enhancement are f^2 and $f^2/2$, respectively. The enhancement is generally higher for low QY (here $\text{QY} = 0.001$), because the radiative rate can be significantly enhanced. Diffusion lowers the enhancement since excitons can move away from the tip and their radiative decay will not be enhanced. For high QY (here $\text{QY} = 0.95$), the tip rather reduces the QY due to quenching. Diffusion slightly increases the enhancement, because it preserves some excitons from tip quenching.

significant, but a slight increase of the enhancement is predicted. In summary, TENOM works best for low QY emitters, but excited state diffusion strongly affects the enhancement in this case.

Conclusion

In this chapter, a flexible and versatile numerical model for the calculation of the exciton density in SWNTs has been developed. It accounts for exciton diffusion, the tip-induced rate enhancements and simulates the imaging process. Exciton energy gradients leading to a directed diffusion can be easily implemented by modifying the diffusion probabilities depending on the direction. Steady-state experiments with continuous excitation as well as time-resolved PL measurements with pulsed excitation can be described and analyzed. It was shown, that the evaluation of such experiments relies on complementary numerical modeling.

In the following two chapters, experimental TENOM images showing the interplay of excitons with defects and exciton energy minima are presented. The numerical model is used to understand the underlying SWNT properties and deduce e.g. the diffusion length from a near-field image.

7 Exciton mobility and quenching studied with TENOM

This chapter is based on the paper "*Probing exciton propagation and quenching in carbon nanotubes with near-field optical microscopy*" that has been published in *physica status solidi (b)* (Vol. 246, p. 2683–2688, 2009).

In the previous chapter, a theoretical model describing the exciton diffusion in SWNTs has been introduced. In the following, it will be shown how this can be applied to understand experimental TENOM images. Nanoscale PL imaging allows for direct visualization of the local exciton distribution and its connection to quenching ends and defects, thereby revealing the exciton diffusion process. For DNA-wrapped SWNTs on a substrate, it is very often found that the PL intensity varies strongly along the SWNT, showing alternating bright and dark sections on length scales below 100 nm. Furthermore, the PL always fades out towards the ends. By employing the numerical model, these observations can be interpreted by few distinct quenching sites on the SWNT, including the ends. The comparison of simulation and experiments shows a good agreement which confirms the simple description of 1D diffusion and quenching at specific defects locations. An evaluation and simulation of the PL distribution near a localized single quenching site can even be used to determine the exciton diffusion length from a TENOM image. Thus, near-field PL imaging can directly visualize and quantify exciton mobility, when combined with numerical modeling. In the final section, the diffusion properties reported here are compared to recent publications from other groups showing a significant dependence on the type of SWNT material and the sample preparation.

7.1 PL intensity variations along individual SWNTs

The experimental data presented and discussed in the following was measured on samples with DNA-wrapped SWNTs on a mica surface, prepared as described in section 4.2. Near-field PL imaging on these samples commonly shows strong intensity variations along individual nanotubes. Some typical examples are presented in Fig. 7.1. Despite the uniform appearance of the nanotubes in the topography images, the PL distribution is characterized by alternating bright and dark sections. This observation can be interpreted as the interaction of excitons with individual quenching sites, as already discussed in chapter 5.

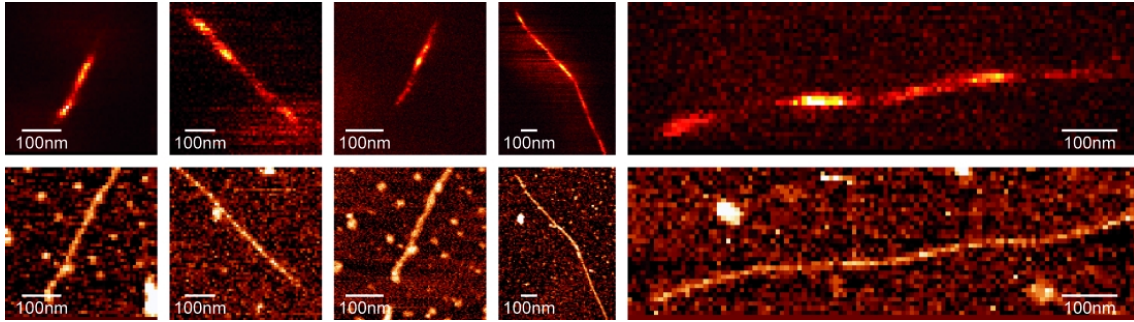


Figure 7.1: Examples for near-field PL images showing strong intensity variations along individual SWNTs. The images in the upper row present the photoluminescence intensity detected by the APD, the lower row shows the respective topography (height range 3 nm). Despite the uniform appearance of the SWNTs in the topography, the PL intensity is often very non-uniform. This can be attributed to quenching at specific defect sites. The spatial gradient of the variations is connected to the exciton mobility.

There, discrete temporal PL intensity changes have been analyzed and were attributed to the introduction of an additional quenching site on the SWNT. The PL is thereby quenched in the vicinity of such a defect, within a range connected to the exciton diffusion length. In the TENOM measurements presented in Fig. 7.1, this effect is imaged with nanoscale spatial resolution by directly visualizing the exciton distribution along the nanotubes. Furthermore, the quenching at the nanotube ends is always visible as a fade-out of the PL towards the ends, whose location is apparent in the topography. Generally, the nanotubes appear always shorter in the near-field PL image than in the corresponding topography. The numerical simulation of the exciton distribution and the near-field imaging process presented in chapter 6 can now be used to reproduce the experimental observations and confirm the theoretical description of exciton mobility and quenching.

7.2 Exciton quenching near ends and defects - experiment and simulation

At first, the PL distribution along short nanotubes will be analyzed. Figs. 7.2a and c show the near-field PL image of a 120 nm and 190 nm long SWNT, with the strongest PL in the middle and quenching towards the ends. These act as the only distinct quenching sites and the configuration is thus very simple and can be easily simulated. The nanotube length was determined independently from the corresponding topography image.

For the numerical simulations, an exciton diffusion length of 100 nm was used and the tip diameter was set equal to the FWHM of the PL distribution across the SWNT, defining the spatial resolution. The experimental cross section for the first data set is displayed in Fig. 7.2b and has a FWHM of 30 nm. The simulated PL distribution along the two nanotubes is plotted in Figs. 7.2b and d, together with the experimental profiles. Though

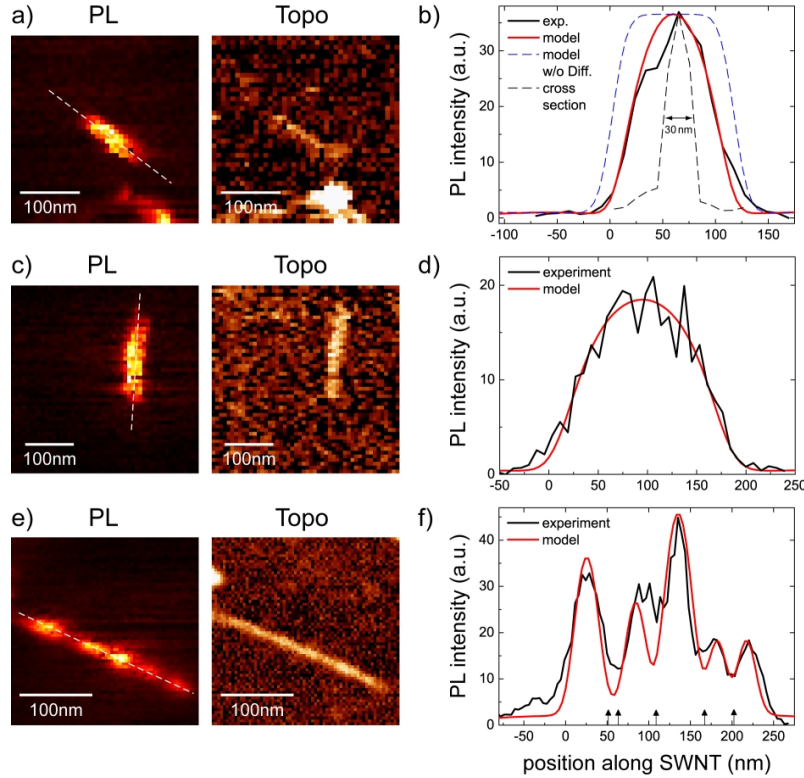


Figure 7.2: PL quenching at ends and defects imaged with TENOM and simulated using the numerical model. a) and c) Near-field PL image and topography of short SWNTs with a length of 120 and 190 nm, respectively. The PL gradually drops off towards the ends. b) and d) PL intensity along the SWNTs taken from the experiment (black lines) and compared to the simulated distribution for complete quenching at the ends and $L = 100$ nm (red lines). The experimental data are profiles along the white dashed lines in a and c. For the first SWNT in b, the simulated profile for non-mobile excitons (without diffusion) and the experimental PL cross-section, defining the spatial resolution, are also shown. e) Near-field PL image and topography of a 240 nm long nanotube showing distinct PL variations. f) PL intensity along this SWNT plotted together with the simulated PL distribution. Complete quenching was assumed at the ends and at 5 additional defects (positions marked by black arrows). Apparently, the simulations are in reasonable agreement with the experimental data, despite the rather simple description.

the limited signal-to-noise ratio does not allow for a perfect match between simulation and experiment, the simple model with quenching only at the ends and a diffusion length of 100 nm can reproduce the PL profile.

For comparison, a simulated profile for non-mobile excitons ($L = 0$ nm) is also plotted in Fig. 7.2b, which deviates strongly from the experimental profile. The gradual PL decrease towards the ends becomes much steeper and results only from the limited spatial resolution of 30 nm in this case. This comparison shows that the effect of exciton diffusion can be clearly distinguished in the experiment.

Fig. 7.2e presents the TENOM image of a nanotube with a length of 240 nm, characterized by several PL maxima and minima along the tube. Here, quenching apparently occurs also at additional defect sites in-between. Indeed, the PL profile along the tube as shown in Fig. 7.2f can be reproduced by assuming five additional defects in the simulation, located at the positions marked with the black arrows. This simple assumption of complete quenching at five defects and the ends can reasonably explain the dot-like PL, although the match between simulation and experiment is not perfect. Nevertheless, the theoretical description of exciton mobility and quenching used for the simulation appears to be consistent with experimental observations.

It is conceivable that some defects might not quench excitons with an efficiency of 100% and it is also discussed that defects could localize excitons which would then in turn lead to enhanced PL from the defects [71]. A strong indication of localized excitons should be a bright PL spot with a strong spectral red-shift due to the local state being lower in energy. Experiments visualizing exciton localization are reported in chapter 8, but the localization is attributed to environmental effects and not to defects on the SWNT.

In the following section, the PL intensity near an individual quenching site is analyzed, which allows for a quantitative evaluation of the exciton diffusion length from a TENOM image.

7.3 Exciton quenching near a localized single defect - evaluation of the diffusion length

The evaluation of the PL properties near a single localized quenching site reveals its individual impact, separated from other perturbations. It is thereby suitable for a more quantitative analysis. The data shown in Fig. 7.3 is based upon a spectroscopic image. In the example spectrum in Fig. 7.3e, the Raman G-band at 703 nm and the PL peaks of two nanotubes with different chiralities can be seen.

The peak at 930 nm originates from a DNA-wrapped (9,1) nanotube whereas the peak at 975 nm is characteristic for a DNA-wrapped (8,3) nanotube [7, 158]. The respective peak intensities derived from the spectra are mapped in Fig. 7.3b-d. The topography in Fig. 7.3a shows a long and a short SWNT and some particles, probably excess DNA or some undefined dirt. The spectral information in Fig. 7.3b and c reveals that the long nanotube consists of two SWNTs with different chirality. The lower section is the (8,3)-SWNT and the upper section is the (9,1)-SWNT, that additionally exhibits a detectable Raman signal depicted in Fig. 7.3d. The short nanotube on the bottom left side is not visible in the optical images, because it is either metallic or emits beyond the detection window above 1030 nm.

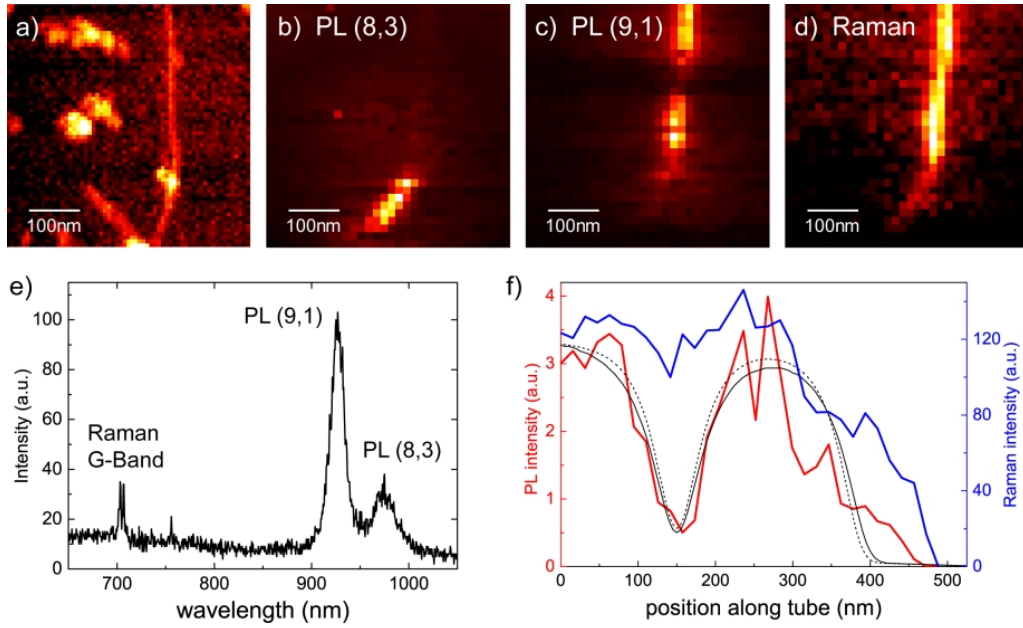


Figure 7.3: Spectroscopic image of the PL and Raman scattering signal near a localized quenching site. The example spectrum in e clearly shows the Raman G-band and two PL peaks from a (8,3) and a (9,1)-SWNT, respectively. a) Topography. b) PL intensity from the (8,3) nanotube at $\lambda = 975$ nm. c) PL intensity from the (9,1) nanotube at $\lambda = 930$ nm. In the middle of this tube, the PL is quenched due to a localized defect. d) Intensity of the Raman G-band. f) Cross-section of PL and Raman intensity along the (9,1)-tube and the simulated PL profile due to a single defect for a diffusion length L of 100 nm (solid black line) or 80 nm (dashed line). The defect quenches the PL on a length of ~ 100 nm while the Raman signal remains unchanged, indicating no substantial damage of the nanotube and uniform signal enhancement by the tip. Near the defect, the simulation fits best for $L = 100$ nm, whereas a value of 80 nm results in a significantly narrower PL dip.

The PL and Raman signal intensities along the (9,1)-SWNT are plotted together in Fig. 7.3f. From this and the Figs. 7.3c and d, it is apparent that the PL is quenched in the middle of this nanotube, while the Raman signal remains unchanged, confirming that the nanotube is not substantially damaged and the tip-enhancement is stable. One can assume a localized quenching defect at this location. The PL intensity distribution near this individual quenching site can be simulated, assuming complete quenching and a diffusion length of 100 nm. The tip diameter was set to 35 nm, according to the spatial resolution determined from the images. The simulation result is also plotted in Fig. 7.3f and is in very good agreement regarding the length scale and relative amplitude of the PL reduction near the quenching site. Using different diffusion length (e.g. 80 nm, 120 nm), the agreement is significantly reduced and a value of $L = 100 \pm 20$ nm can be extracted based on the comparison between experiment and simulation.

The lower end of the (9,1)-SWNT is not well defined due to the big particle visible in the topography. The PL reduction towards this end does not agree with the simulation,

because the particle decreases PL enhancement due to an increased tip-sample distance, while the actual position of the end is also not clear from the optical data due to some crosstalk from the optical signal of the (8,3)-SWNT.

This measurement shows, that the exciton diffusion length can be directly derived from near-field PL images when combined with numerical simulations. The simulations are essential to interpret the experimental data resulting from the complex near-field imaging process. The value of $L = 100 \pm 20$ nm is in very good agreement to the value derived earlier based on the far-field bleaching experiments reported in chapter 5 and 6. Using an exciton lifetime τ in the range of 5 – 20 ps [42], the diffusion coefficient D can be estimated as 2.5 – 10 cm²/s. This demonstrates, that TENOM can directly visualize and measure the exciton mobility for SWNTs on substrates.

The microscopic origin of the quenching site discussed here, as e.g. chemisorbed oxygen, can not be identified. The signal-to-noise ratio of the G'-band does not allow for analysis of its band shape in analogy to ref. 71 in order to identify the possible defect type.

7.4 Exciton diffusion length and the SWNT environment

Recent publications from other groups show, that the exciton diffusion length depends on the environment of the nanotube. Substrate interaction and doping modify the exciton lifetime τ which defines the diffusion length for a fixed diffusion constant.

Siitonen *et al.* [142] studied the step-wise quenching upon single chemical modifications of (7,5)-SWNTs dispersed with different surfactants and immobilized in agarose gel. They report values of $L = 100 - 170$ nm, slightly depending on the surfactant. They also studied the dependence on the SWNT chirality and found an increased diffusion length for larger diameter SWNTs, up to $L = 260$ nm for a (12,5)-SWNT [143].

Yoshikawa *et al.* [144] studied suspended SWNTs in vacuum where step-like PL bleaching occurred upon oxygen adsorption. They determined $L = 200$ nm. Another report on the diffusion length for freely-suspended SWNTs states $L = 860$ nm, which is attributed to the highly defect-free growth of their SWNTs and the absence of substrate interactions [145]. On the other hand, $L = 6$ nm was published for highly defective (6,5)-SWNTs [38].

It becomes clear that the effective diffusion length strongly depends on the SWNT material and its environment. For isolated, defect-free SWNTs, values up to 1 μ m are plausible. Structural defects arising from the growth process and further steps of purification and suspension, which do not quench excitons directly might decrease the diffusion constant as they reduce the SWNT crystallinity. Lifetime reduction expected for (unintentional) doping and substrate interaction will further reduce L . Thus, the diffusion lengths for thin nanotubes on substrates and dispersed with surfactants are in the range of 100 – 200 nm.

Conclusion

In this chapter, high-resolution near-field PL images of DNA-wrapped nanotubes on mica have been presented. The PL intensity is often highly non-uniform along the SWNT, characterized by bright and dark segments. These spatial variations reflect the impact of localized quenching sites which have already been observed in the PL blinking experiments in chapter 5. The nanoscale imaging of the PL distribution combined with numerical simulations reveals the underlying exciton properties. The experimental data can be well reproduced which validates the theoretical description of exciton diffusion and quenching introduced in chapter 6. For the case of PL quenching near an individual defect site, a quantitative analysis of the TENOM image is possible, from which the exciton diffusion range can be determined as $L = 100 \pm 20$ nm. This is in good agreement with the value reported earlier and demonstrates that TENOM can directly visualize exciton propagation.

8 Exciton localization visualized using near-field spectroscopic imaging

The following chapter is based on the paper "*Probing Exciton Localization in Single-Walled Carbon Nanotubes Using High-resolution Near-field Microscopy*" that has been published in *ACS Nano* (Vol. 4, p. 5914–5920, 2010).

This chapter reports on the observation and experimental verification of exciton localization in SWNTs. In contrast to quenching defect sites, localization leads to locally enhanced PL intensity caused by an increased exciton density at localization sites. The inhomogeneous exciton density is here attributed to exciton energy variations along the SWNT that modify the diffusion process and facilitate diffusion towards energy minima. The variations arise from an inhomogeneous DNA-wrapping and possible charges in the mica substrate. The localization sites are connected to narrow exciton energy minima with depths of more than 15 meV and lateral energy gradients exceeding 2 meV/nm. Spectroscopic near-field PL imaging is used to correlate PL intensity and energy with nanoscale resolution, which evidences the introduced explanation. Accompanying numerical simulations of exciton diffusion in an inhomogeneous environment further support this picture.

The localization of intrinsically mobile excitons strongly affects the optical properties of SWNTs and will be relevant for applications relying on energy transfer such as excitonic solar cells [159]. Localized excitons show increased exciton-phonon coupling and are thus subject to faster phonon-induced non-radiative loss channels [54]. The inhomogeneous exciton distribution that arises from localization will affect the exciton-exciton annihilation dynamics and the PL saturation behavior at increased excitation levels. Additionally, quantum emission in terms of photon-antibunching has been attributed to strong localization combined with efficient exciton-exciton annihilation which inhibits simultaneous emission [160,161]. SWNTs could thus be used as single photon sources with spatially confined emission sites in novel nano-photonic devices that could also be driven electrically.

Exciton localization has been observed at low temperatures where its spectral and temporal characteristics become apparent in diffraction limited PL experiments [123,160–162]. All of these observations of exciton localization were indirect in the sense that the spatially confined distribution of excitons was not probed by direct imaging. The relevant length scales below 100 nm are not accessible by conventional diffraction limited microscopy, but can be investigated using TENOM.

8.1 Observation of strongly localized PL

High-resolution PL images of DNA-wrapped SWNTs on mica substrates often show a strongly varying PL intensity along the nanotube. As discussed in chapter 7, this can be attributed to randomly distributed defects that quench the excitons in their vicinity, leading to a strong PL reduction on a length of about 100 nm due to exciton mobility. However, for about 5 – 10% of the investigated nanotubes, highly localized PL emission spots are observed which appear very bright and are therefore unlikely to be caused by quenching defects. Three examples are shown in Fig. 8.1, where bright PL spots are localized within 30 nm.

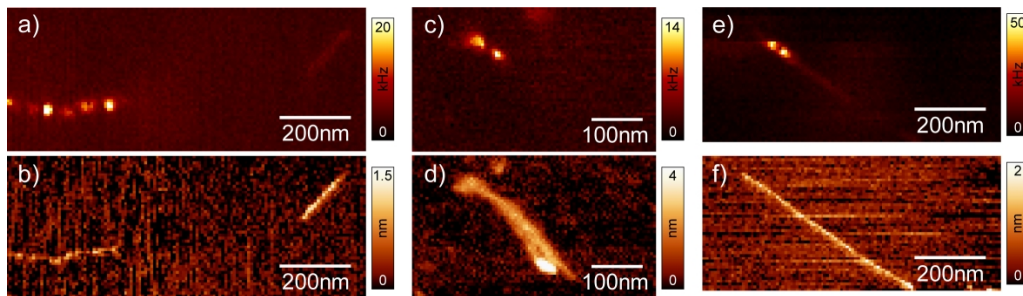


Figure 8.1: Near-Field PL images of SWNTs showing strongly localized and bright PL. a), c) and e) Near-Field PL intensity (photon count rates). b), d) and f) Corresponding topography image. The strong PL in these cases is localized within regions smaller than 30 nm, which can not be explained by quenching defects in between. Instead, the strong PL at these spots is attributed to an increased exciton density due to localization.

When assuming quenching sites in between these spots as origin of the PL variations, one would expect that the PL almost vanishes. For quenching sites with distances below 50 nm, most of the excitons generated in between will most certainly reach the defects due to their mobility and thus get quenched.

8.2 Experimental evidence for exciton energy gradients at localization sites

An alternative explanation is that the localized bright PL originates from an increased exciton density due to exciton localization in terms of trapping. It is known from earlier experiments that the DNA-wrapping is non-uniform along the nanotubes and can locally decrease the exciton energy [153]. If the effect occurs very localized and exciton energy gradients along the nanotube become large enough, this is expected to affect the exciton diffusion and lead to an increased exciton density at these local exciton energy minima. The bright and localized PL emanating from these minima will in turn be lower in energy,

i.e. red-shifted. Near-field spectroscopic imaging can be used to map the emission energy with nanoscale resolution and verify this concept of localization.

Figs. 8.2a and b show a near-field PL image of several luminescent SWNTs and the corresponding topography.

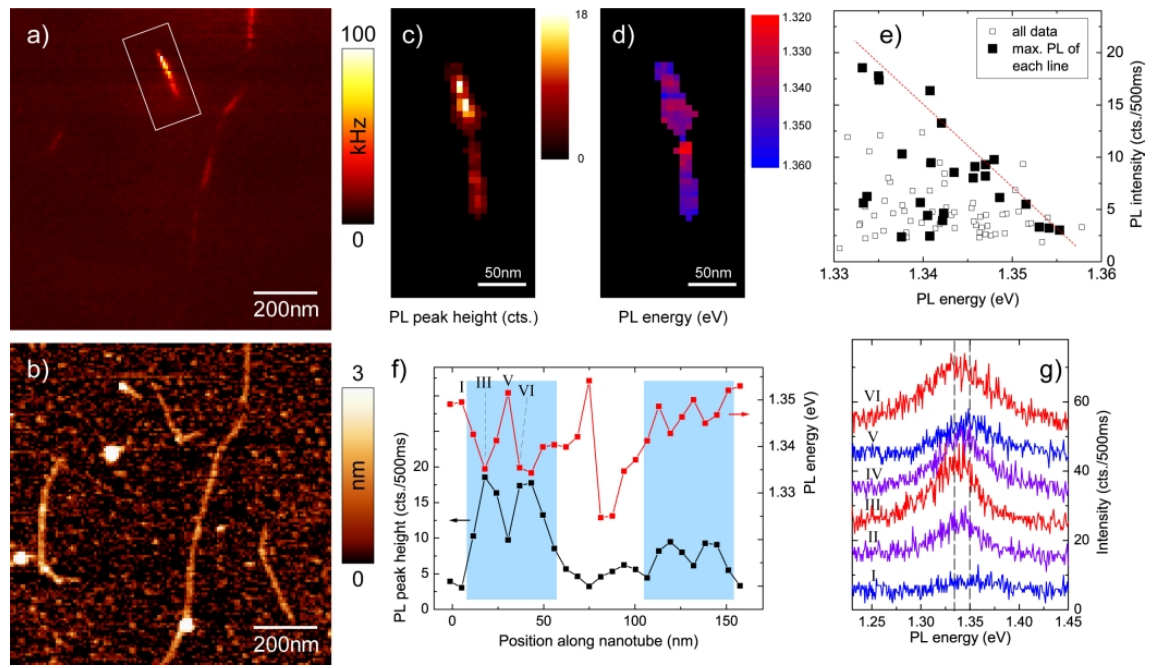


Figure 8.2: Exciton localization in a 160 nm long (9,1) SWNT evidenced by spectroscopic imaging. a) and b) Near-field PL image and corresponding topography showing several luminescent SWNTs. The very bright nanotube with strong local PL variations indicates exciton localization. c) and d) Maps of the PL intensity and energy from a subsequent spectroscopic image of the area marked in a. e) Correlation between PL intensity and energy for all image pixels (filled and open squares), with the brightest pixel of each image line being highlighted (filled squares) to account for the influence of finite spatial resolution (see text). f) PL intensity and energy plotted along the SWNT. In the upper and lower section of the tube (pale blue areas), bright PL is clearly correlated with lower energy. The weak PL in the middle section is probably due to a quenching defect. g) Near-field spectra from six adjacent positions (I-VI) along the SWNT, equally spaced by 6.5 nm and marked in f. The PL energy shifts by up to 15 meV between neighboring positions (indicated by two dashed lines). These strong exciton energy gradient of ~ 2 meV/nm in the configuration of a potential minimum lead to exciton localization.

The short nanotube in the upper part is much brighter than the other present SWNTs with strong PL intensity variations on length scales of about 10 nm. In particular, the strongest PL intensity with photon count rates above 100 kHz is emitted very locally in the upper part of this nanotube. This unusual bright and localized PL indicates exciton localization which is supported by the subsequent spectroscopic image from the marked area in Fig. 8.2a. Here, a complete spectrum was recorded at each pixel to determine the

local PL energy. The results are depicted in Figs. 8.2c and d, showing PL intensity and energy derived from a peak fit of the spectra at each image pixel.

Along the 160 nm long SWNT, the PL energy varies by about 30 meV. For the upper and lower nanotube section this correlates well with bright PL at energy minima (see also Fig. 8.2f). The PL in the middle section is very weak, which is attributed to a quenching defect at this position. During the preceding near-field scan on this SWNT (Fig. 8.2a), this section still appeared bright. However, also traces of PL blinking were seen, which is a sign for the formation of photo-induced defects. The first scan probably induced a defect which quenches the PL in the middle section of the nanotube. Although nanotube PL is found to be remarkably stable during image scans taking up to 30 minutes, additional quenching sites are sometimes introduced and need to be considered in the data analysis.

The correlation between PL intensity and energy is displayed in Fig. 8.2e, using data from all image pixels (open and filled squares). Clearly, bright PL is associated with lower energy and higher energy emission is weak, as expected for energy induced localization. For two reasons, an exclusive correlation between PL intensity and energy can not be expected. First, the imaging process with its finite point-spread-function results in many data points below the dashed line. In the present image, the pixel size of 6.5 nm is about three times smaller than the optical resolution. Hence, there are always several pixels with lower intensity surrounding a central pixel with maximum tip enhancement, all at the same PL energy. Selecting only the brightest pixel of each image line across the SWNT (closed squares in e), this effect is avoided at least in one direction and the correlation becomes much clearer, since most of the omitted pixels are below the line. Second, exciton localization is not the only factor determining the PL intensity. Local defects and doping will quench excitons and thus reduce PL intensity.

In Fig. 8.2f, PL intensity and energy are plotted against the position along the SWNT. In the upper part, where the relation between strong PL and low energy is most pronounced, the energy varies on very small length scales. The pronounced energy minimum between positions I and V has a depth of about 15 meV and extends only 25 nm. The corresponding energy gradients towards the minimum are about 1.2 meV/nm, which creates an efficient driving force for exciton drift. The neighboring positions V and VI have an energy difference of 15 meV at a distance of only 6.5 nm, corresponding to a gradient exceeding 2 meV/nm. Due to the finite optical resolution, the actual gradient in the nanotube is expected to be even larger. In the middle section a PL energy drop of even 30 meV/6.5 nm (~ 5 meV/nm) can be seen though due to the weak PL intensity this value is not as reliable. Fig. 8.2g shows the corresponding PL spectra from positions I-VI with clearly visible peak-shifts on very small length scales. It becomes clear that for efficient exciton localization, the exciton energy minima must be sufficiently deep and spatially confined.

Fig. 8.3a illustrates localized and strong PL for another nanotube. The simultaneously recorded topography (Fig. 8.3b) demonstrates that the nanotube is about 450 nm long.

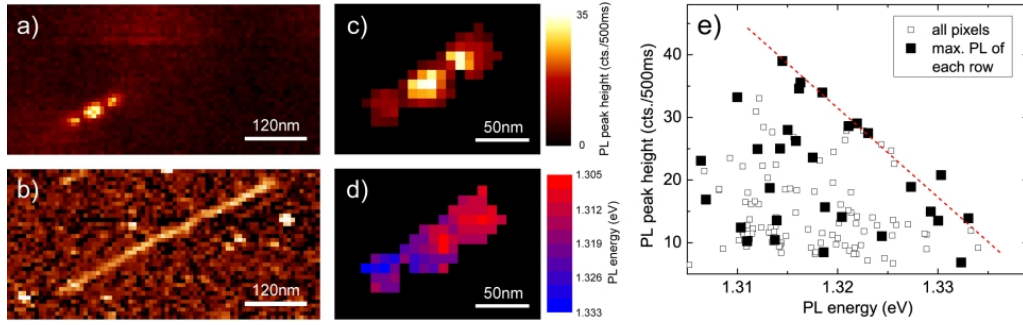


Figure 8.3: Exciton localization in a 450 nm long (9,1) SWNT evidenced by spectroscopic imaging. a) and b) Near-field PL image and corresponding topography showing several luminescent SWNTs. The very bright nanotube with strong local PL variations indicates exciton localization. c) and d) Maps of the PL intensity and energy from a subsequent spectroscopic image. e) Correlation between PL intensity and energy for all image pixels (filled and open squares), with the brightest pixel of each image line being highlighted (filled squares). Bright PL is apparently shifted to lower energy.

However, PL is only emitted from three points in the left part of the SWNT. A subsequent spectroscopic image (Figs. 8.3c and d) reveals again strong PL energy variations. The PL intensity and energy exhibit a similar correlation, presented in Fig. 8.3e. Based on the PL energy, the chirality of this SWNT is assigned as (9,1). Compared to the average PL energy of DNA-wrapped (9,1)-SWNTs on substrates, which is 1.332 eV [153], the localized PL observed in Fig. 8.3d with energies down to 1.310 eV is exceptionally red-shifted. This can account for the strong degree of localization apparent in Fig. 8.3a.

8.3 Numerical simulation of exciton diffusion directed by energy gradients

The experimental evidence presented so far is complemented by numerical simulations of the exciton diffusion in an inhomogeneous environment, which causes exciton energy variations. The numerical model was introduced in section 6.4 and is now used to calculate the near-field PL distribution along a nanotube with localized exciton energy minima. The enhancement factors for excitation and radiative rate in vicinity of the tip (f^2 and f_{rad}^2) were set to 25 and 10, respectively. The resulting signal enhancement is then in agreement with the observed near-field to far-field contrast in the images presented so far. f_{rad}^2 is smaller due to the weaker plasmonic response of the gold tip at the PL energy with respect to the excitation at 632.8 nm [102].

Fig. 8.4 shows calculated PL intensity profiles along a 300 nm long nanotube with three energy minima of depth ΔE , varied between 10 and 40 meV on a length scale of about 10 nm (see inset). The calculations indicate that for exciton energy minima with depths above 10 meV, the localization effect becomes significant and clearly observable with TENOM.

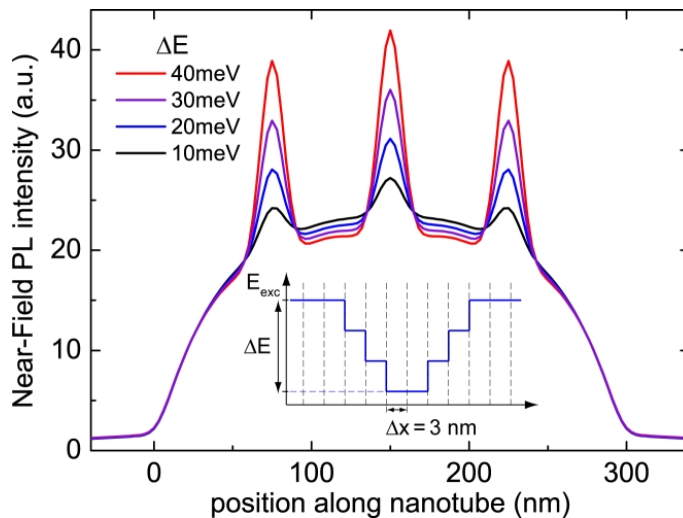


Figure 8.4: Simulated near-field PL intensity for a 300 nm long carbon nanotube. Three exciton energy minima have been introduced to the nanotube, centered at 75, 150 and 225 nm from the left nanotube end. The profile of the energy minima is shown in the inset, the depth ΔE is varied between 10 and 40 meV. Due to enhanced exciton diffusion towards energy minima, the PL intensity is increased at these positions.

This corresponds to exciton energy gradients in the order of several meV/nm, in good agreement with the presented experiments. These simulations thus strongly support the model of energy-induced exciton localization.

The numerical model also shows, that at low temperature the influence of energy gradients on exciton diffusion according to eq. 6.25 should be remarkably increased. Localization is then expected to be far more efficient and will dominate the PL properties even in far-field experiments. This is supported by the observation of quantum emission in terms of photon anti-bunching below 25 K [160,161]. For a confocal PL measurement at room temperature however, exciton localization will only lead to spectral broadening due to spatial averaging.

8.4 Origin of the exciton energy variations

The observed exciton energy variations can arise from dielectric screening, determined here by the dielectric constants of DNA and substrate, doping related screening and the Stark effect due to localized charges in the vicinity of the nanotube creating strong local fields [26, 123, 163–165]. Since DNA features a negatively charged backbone, its presence can induce PL energy variations via all three mechanisms. The observed spatial PL energy variations can thus be attributed mainly to the heterogenous environment resulting from nonuniform DNA-wrapping. Local changes of the PL energy caused by DNA-wrapping have been observed previously with TENOM, however without indication of exciton localization due to much smaller exciton energy gradients in the order of 0.2 meV/nm [153]. Assuming randomly distributed DNA-strands, a configuration forming isolated and deep potential

minima is expected to occur rarely. This can explain why pronounced exciton localization is only observed in 5 – 10% of the near-field PL images.

Localized PL emission in a SWNT has been observed previously with TENOM near a negatively charged defect connected to characteristic Raman scattering signals [71]. In this case, PL occurred at a single position only, inhibiting energy-resolved imaging and the investigation of energy induced localization. For the SWNT material studied here, the detected Raman scattering signal is very weak and a corresponding signal analysis regarding the defect type was not possible.

Conclusion

In this chapter, the observation of exciton localization in semiconducting SWNTs at room temperature was presented. It results from spatially confined exciton energy minima with depths of 15 meV and lateral energy gradients exceeding 2 meV/nm. This has been experimentally verified using near-field spectroscopic PL imaging, where PL intensity and energy can be mapped and correlated with nanoscale resolution. Simulations based on a modified exciton diffusion model considering energy variations support this interpretation predicting strongly enhanced exciton densities and near-field PL intensities at localized energy minima. Directional or limited diffusion affects all physical phenomena that are connected to exciton mobility such as exciton-exciton annihilation and quenching by local defects.

9 High-resolution spectroscopic imaging of localized defects

The following chapter is based on the paper "*Tip-enhanced Raman spectroscopic imaging of localized defects in carbon nanotubes*" that has been published in *Appl. Phys. Lett.* (Vol. 97, p. 143117, 2010).

This chapter reports on near-field Raman spectroscopic imaging of localized defects in SWNTs. The experiments were performed on metallic SWNTs where the resonance Raman process allows for a detailed investigation of the Raman spectrum reflecting the nanotube's structural properties. Owing to the high spatial resolution of 15 nm, the spatial extent of the D-band signal in the vicinity of localized defects can be visualized and was found to be about 2 nm only. In addition, localized defects were intentionally generated using the strong optical fields underneath the tip and the temporal evolution of the D-band intensity was recorded simultaneously. From this data, a relation between defect density and resulting D-band intensity could be derived, which is of high interest for the characterization of SWNTs via Raman spectroscopy.

9.1 Spatial extension of the D-band scattering process

As already discussed in section 2.4, D-band scattering in SWNTs is connected to a large momentum phonon and can not occur upon excitation of defect-free structures with visible light ($k \approx 0$) due to momentum conservation. The D-band scattering is a double resonance process, where the electron is resonantly excited and then scattered by a D-phonon. The large phonon momentum brings the electron from the K - to the K' -point in reciprocal space, where it can not recombine. A second elastic scattering event at a defect brings the electron back and thus enables the Raman process.

In ref. 64, a semi-classical real space description of this defect scattering in graphene has been derived, which can also be used for metallic SWNTs due to their comparable band structure for excitation energies below the first interband transition E_{11}^M . Upon photo excitation, a free electron and a hole are generated with opposite momenta. Radiative recombination can occur if one charge carrier is back-scattered by a D-phonon while the other is scattered back by a defect. In this real space model, one charge carrier therefore

needs to reach a defect during its lifetime, which limits the length scale of the D-band scattering process l_D near a defect. This picture is illustrated in Fig. 9.1.

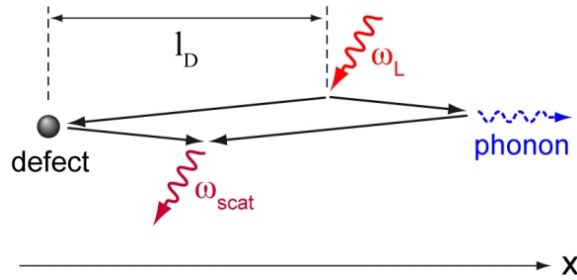


Figure 9.1: Illustration of the D-band scattering process in real space according to ref. 64. Upon photo excitation a free electron and a hole are generated with equal but opposite momenta. Radiative recombination can occur if one charge carrier is back-scattered by a D-phonon while the other is scattered back by a defect. The charge carrier lifetime and velocity limit the length scale of this process, since a defect must be reached. The maximum distance l_D between excitation and defect necessary for D-band scattering is important for the relation between D-band intensity and defect density. It can be determined using TENOM.

The determination of the defect density based on the D-band intensity depends critically on l_D . The length of the SWNT segment around a single defect which gives rise to the D-band is $2l_D$. If this length is large, the D-band intensity saturates quickly with increasing defect density, when the "activated" segments overlap. The saturation starts when the average defect distance approaches $2l_D$. Below saturation, a linear relation between D-band intensity and the number of defects can be expected.

For graphene, a length scale of about 4 nm has been estimated based on the uncertainty principle and the electron velocity [64]. A value of $l_D = 2$ nm was determined experimentally by connecting the D-band intensity with the defect density measured by scanning-tunneling microscopy [166]. Attempts to deduce the D-band extension near a graphene edge, which acts as a one-dimensional defect, using confocal Raman microscopy were hampered by the diffraction limited spatial resolution of several 100 nm [167,168]. Only recently, an improvement of the experimental approach allowed for a more accurate measurement of l_D despite the far-field resolution and a value of 3 nm was found [169]. A similarly small value could be expected for metallic SWNTs.

Spectroscopic near-field Raman imaging is ideally suited to investigate this issue in SWNTs. The different Raman bands can be imaged simultaneously with high spatial resolution and they can be very well spectrally separated in the subsequent data analysis.

Metallic SWNTs on bare glass cover slides have been studied in these experiments. Fig. 9.2a shows the near-field Raman G-band image of a 250 nm long SWNT, where the G-band signal was detected with the APD after bandpass filtering. The G-band intensity is rather homogeneous along the SWNT with only long range variations. The spatial resolution

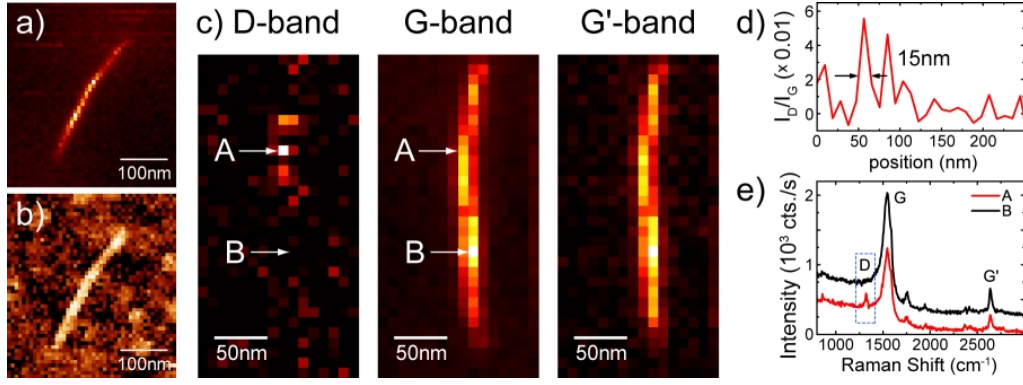


Figure 9.2: Near-field spectroscopic Raman image of a metallic SWNT with a localized defect site. a) G-band near-field image based on APD detection recorded prior to the spectroscopic image. b) Corresponding topography (height-range is 1.5 nm). c) Intensity maps of the D-, G-, and G'-band generated from the spectroscopic image. The pixel size is 10 nm. The D-band is strongly localized at a defect site in the upper half. d) Distribution of the I_D/I_G -ratio along the SWNT, showing strong local variations on length scales similar to the spatial resolution. e) Spectra from the positions A and B marked in c with maximum D- and G-band intensity, respectively. Spectra are offset by 250 cts. for clarity.

of this optical image is around 15 nm, determined by tip diameter. The resolution is defined by the full-width-at-half maximum of the Raman signal across the SWNT, since the SWNT is much thinner than this value. The simultaneously acquired topography in Fig. 9.2b shows no apparent inhomogeneities.

The results from a subsequent spectroscopic image are shown in Fig. 9.2c, namely the intensity maps of the D-, G- and G'-band. The integrated intensities of the G- and G'-band I_G and $I_{G'}$ are quite uniform along the SWNT, whereas the D-band intensity I_D is strongly localized in the upper half. For quantitative discussions, the ratio of I_D/I_G is commonly used as a measure for the defect concentration. The normalization by I_G eliminates possible variations in the signal enhancement and accounts for a modified resonance condition of the Raman process due to defect induced changes of the band structure. The distribution of I_D/I_G along the SWNT is plotted in Fig. 9.2d, showing that the D-band scattering is localized within 15 nm, equal to the spatial resolution of the experiment. Fig. 9.2e presents the spectra from the indicated pixels with highest and lowest I_D/I_G , respectively. D-band scattering is clearly seen at position A, whereas at position B the spectrum indicates the absence of defects.

The spatial extension of D-band scattering from a point-like defect that is measured in the experiment arises from the convolution of the intrinsic D-band active segment with a length of $2l_D$ and the point-spread-function of the near-field experiment, represented by a Gaussian with a FWHM corresponding to the spatial resolution. If $2l_D$ is much smaller than the resolution, the measured width of the I_D/I_G -signal along the SWNT is simply the sum of $2l_D$ and the width of the PSF. Here, a similar value of 15 nm for the width of both

the PSF and I_D/I_G is observed. Thus, l_D must be very small, definitely far below 10 nm. The rather large pixel size of 10 nm in this case hinders a more quantitative conclusion.

During a subsequent near-field scan of the SWNT in Fig. 9.2, it has been shifted on the sample surface by the gold tip. Accidentally, the tuning fork oscillation amplitude was increased, which lead to a stronger tip-sample interaction. The APD-based near-field image recorded during this scan is shown in Fig. 9.3c and d.

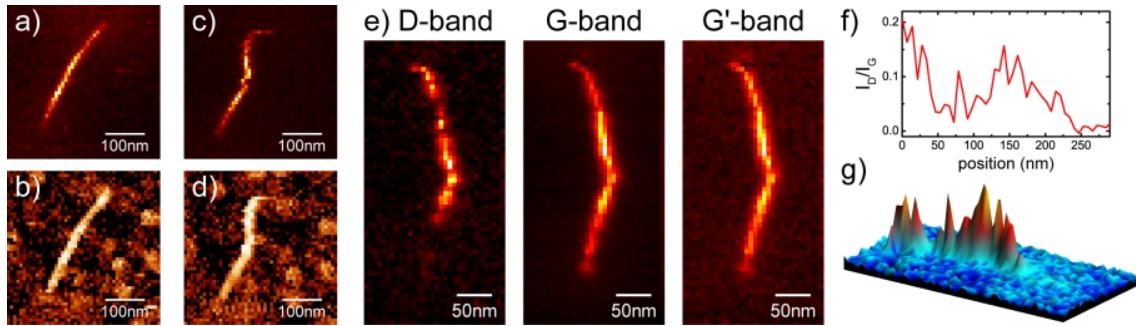


Figure 9.3: Mechanical generation of defects by the interaction of gold tip and SWNT. a) and b) Preceding near-field scan from Fig. 9.2, shown again for comparison. c) and d) Subsequent APD-based near-field scan during which the SWNT was shifted on the surface by a too strong interaction with the scanning tip. e) Results from a spectroscopic image recorded after this perturbation, revealing that the SWNT is now decorated with many localized defects. The pixel size is 6.5 nm. f) Distribution of the I_D/I_G -ratio along the tube. g) 3D plot of I_D , illustrating the D-band intensity variations. Changes occur on a length scale similar to the optical resolution.

In both G-band image and topography, it can be seen that the SWNT was shifted back and forth by the scanning tip during the first half of the scan. For comparison, the previous near-field scan is shown again in Fig. 9.3a and b. A spectroscopic image recorded after this perturbation reveals that the SWNT is now decorated with many localized defects that have been generated mechanically by the tip. The D-band intensity along the tube varies strongly on length scales similar to the spatial resolution, which again indicates that the length of l_D must be very small.

Another data set for a different SWNT with a few localized defects is shown in Fig. 9.4. The D-band intensity is again strongly localized to certain positions. Here, the utilized gold tip had a slightly larger diameter and the spatial resolution is about 30 nm. The minimum width of the peaks in the I_D/I_G distribution along the SWNT (Fig. 9.4d) has the same value, which again shows that l_D must be very small.

A more conclusive measurement is depicted in Fig. 9.5b, where a small pixel size of only 5.65 nm was used and the spatial resolution was again 15 nm. Furthermore, the D-band intensity is very strong here. One of the two defect sites in this SWNTs was intentionally generated, which is discussed in the following section. The spatial distribution of I_D/I_G along the SWNT after defect generation is shown in Fig. 9.5d. Apparently, the D-band

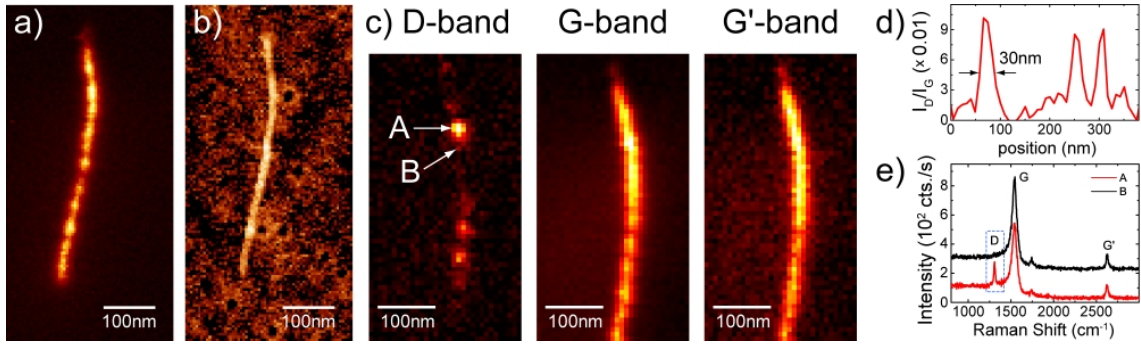


Figure 9.4: Near-field spectroscopic Raman image of a metallic SWNT with localized defect sites. a) G-band near-field image based on APD detection recorded prior to the spectroscopic image. b) Corresponding topography (height-range is 2 nm). c) Intensity maps of the D-, G-, and G'-band generated from the spectroscopic image. The pixel size is 8.6 nm. d) Distribution of the I_D/I_G -ratio along the SWNT, showing strong local variations on length scales similar to the spatial resolution. e) Spectra from the positions A and B marked in c with maximum D- and G-band intensity, respectively. Spectra are offset by 200 cts. for clarity.

scattering arises mainly from three defect sites and is localized within 17 nm around those. Given the optical resolution of 15 nm, a value of $2l_D \leq 2$ nm can be estimated, representing an approximate upper limit. A larger value as e.g. 5 nm would be clearly distinguishable in this experiment. The small value of l_D is comparable to the results reported for graphene.

9.2 Tip-induced generation of localized defects

As already mentioned, an additional defect site was intentionally generated on the SWNT in Fig. 9.5. This was done to generate a highly localized defect site with intense D-band, where l_D could be determined afterwards. Furthermore, the temporal evolution of I_D/I_G during defect generation was recorded. Fig. 9.5a shows the spectroscopic image before the experiment. One localized defect site is already present near the upper end of the SWNT, but the lower part appears nearly defect free. A localized defect site was photo-induced in this part using the intense and highly confined optical fields at the tip, similar to defect generation observed in the far-field experiments in chapter 5 and ref. 170.

The tip was placed on the SWNT at position B using the same laser power of $500 \mu\text{W}$ as for the spectroscopic imaging. From the observed Raman enhancement, an excitation enhancement factor f^2 of about 20 underneath the tip can be estimated, which facilitates photo-induced damage of the nanotube. Simultaneously, tip-enhanced spectra were acquired every 2 seconds in order to follow the evolution of D-band intensity at this position. The process was stopped after about 100s to prevent spatial broadening of the defective spot due to tip-drift. Nevertheless, two closely spaced localized defective spots were created as can be seen in the spectroscopic image recorded afterwards, shown in Fig. 9.5b.

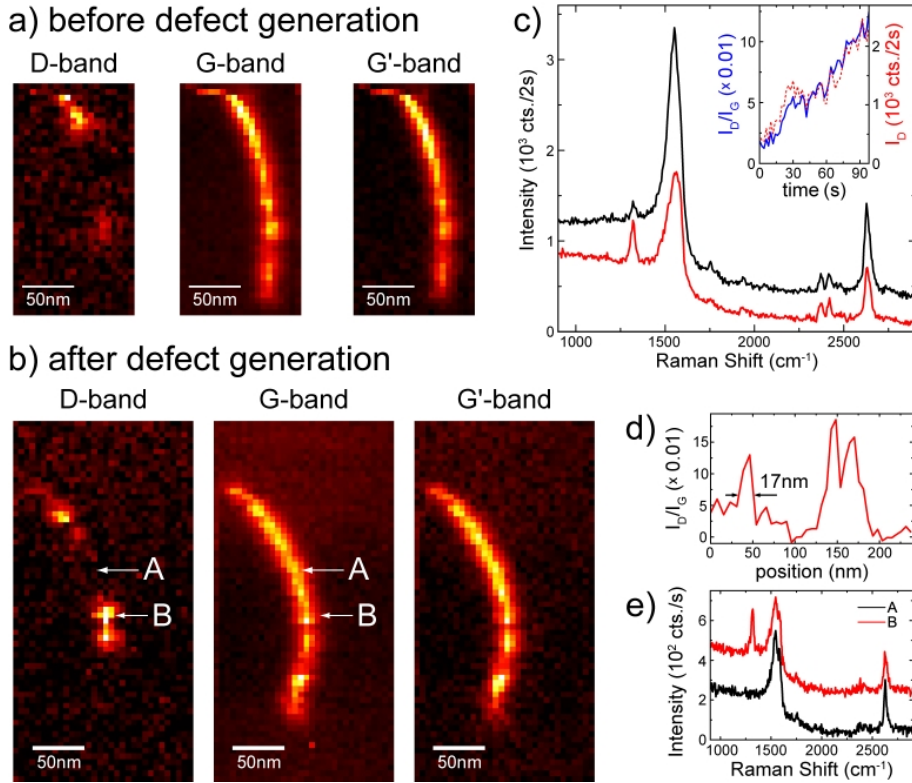


Figure 9.5: Spectroscopic images before and after the tip-induced generation of a localized defect site and the spectral evolution during this process. a) and b) Intensity maps of the D-, G-, and G'-band from spectroscopic images of the same SWNT before and after defect-generation. The pixel size for both is 5.65 nm. Afterwards the D-band intensity shows an additional bright spot in the lower half of the SWNT. c) Spectrum at position B before (black) and after (red) the near-field-induced generation of a localized defective region. The inset shows the temporal evolution of I_D/I_G (blue) and I_D (red dashed) when the tip was parked on position B. d) Distribution of the I_D/I_G -ratio along the SWNT. e) Spectra from positions A and B, representing defect free and highly defective positions within only 50 nm.

The D-band intensity has strongly increased around position B, whereas the G- and G'-band are still rather uniform along the SWNT, excluding major structural damage. Fig. 9.5c presents the spectra from before and after the tip-induced defect generation. Both the I_D/I_G -ratio and I_D increase strongly and rather continuously with time, which is shown in the inset. This means that many defects can be generated within the short nanotube segment that is probed and modified by the tip fields, without an apparent saturation of I_D . Saturation is expected when the average defect distance approaches $2l_D$ so that every excited electron or hole can scatter with a defect. Since the probed length is only 15 nm, $2l_D$ must be significantly smaller than 5 nm, since otherwise a step-like increase of I_D/I_G and a fast saturation are expected. This further supports the value of $2l_D \leq 2$ nm estimated above.

9.3 Relation between defect density and D-band intensity

Regarding the connection between defect density and the I_D/I_G -ratio, the model described in ref. 166 developed for D-band scattering in graphene can be adopted to one-dimensional SWNTs. For average defect distances $L_d > 10$ nm, I_D/I_G is inversely proportional to L_d , analogous to the $1/L_d^2$ dependence in two-dimensional graphene and the well-known Tuinstra-Koenig relation that is widely used for graphitic materials, linking I_D/I_G to the average crystalline size [171]. The "activated" length of the SWNT and thus D-band intensity increase linearly with the number of defects, as long as the interaction ranges do not significantly overlap. Since the number of defects is simply the probed SWNT length divided by L_d , this leads to the L_d^{-1} dependence.

$$\frac{I_D}{I_G} = \frac{C}{L_d} \quad (9.1)$$

The scaling factor C for the metallic SWNTs studied here can be estimated based on the spectra in Fig. 9.5c and the increase of I_D/I_G during defect generation. At the beginning, some weak D-band is already detectable, corresponding to at least one defect. The observed 8-fold increase after 100 s requires a minimum of 8 defects within the probed length of about 15 nm corresponding to $L_d \approx 2$ nm at $I_D/I_G = 0.12$. This results in $C = 0.24$ nm.

However, this value has to be corrected since for $L_d \approx 2$ nm, which is significantly smaller than 10 nm, the ratio I_D/I_G already deviates from the inverse linear scaling. The overlap of the activated segments for small defect distances can be taken into account using the model in ref. 166. The relation between I_D/I_G and L_d is then described by the equation

$$\frac{I_D}{I_G} = \frac{C}{2l_D} \left(1 - e^{-\frac{2l_D}{L_d}} \right). \quad (9.2)$$

using $2l_D = 2$ nm as determined before. At larger defect distances, this becomes equivalent to eq. 9.1. In order to get the measured value of $I_D/I_G = 0.12$ at $L_d \approx 2$ nm, a scaling constant of $C = 0.4$ nm is required. The calculated relation and the simple inverse scaling are plotted in Fig. 9.6.

In conclusion, the relation between defect density and D-band intensity can be written as

$$L_d = \frac{-2 \text{ nm}}{\ln \left[1 - 5 \frac{I_D}{I_G} \right]} \quad (9.3)$$

which can be simplified for $L_d > 10$ nm to

$$L_d = 0.4 \text{ nm} \left(\frac{I_D}{I_G} \right)^{-1}. \quad (9.4)$$

These equations allow the determination of defect densities by simply measuring the Raman spectrum. Determining L_d in SWNTs using the relation established for nanographite [172] is probably inaccurate, since the respective scaling factor is about 75 times larger.

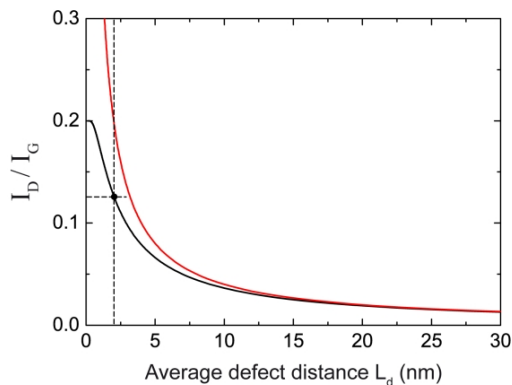


Figure 9.6: Calculated relation between defect density and D-band intensity according to eq. 9.2 using $2l_D = 2$ nm (black line) and the simple inverse scaling from eq. 9.1 valid for $L_d > 10$ nm (red line). To get the measured value of $I_D/I_G = 0.12$ at $L_d \approx 2$ nm (indicated by dashed lines), a scaling constant of $C = 0.4$ nm is required.

The type of defects that lead to the observed D-band could not be specified in these experiments. No changes in the shape of the G'-band characteristic for charged defects [71] or significant shifts of the G-band can be observed. Structural defects from the growth process and photo-induced local oxidation of the SWNT could be a reasonable explanation. In general, the nanotube material studied here exhibits only few defects per micrometer.

Importantly, the ends of the SWNTs do not show apparent D-band scattering in contrast to the armchair edge of graphene. In the case of SWNTs the D-band intensity connected to the edge could be very weak since the selection rules requiring a certain edge type and especially light polarization parallel to the edge will be rarely fulfilled [64]. Furthermore, the end probably acts only as a single defect, which will be very hard to detect.

Conclusion

Tip-enhanced Raman spectroscopic imaging was used to investigate the D-band scattering near defects in metallic SWNTs with high spatial resolution. It was found that the length scale of the D-band scattering process l_D is only about 1 nm, which is similar or even smaller than for graphene [64,166,169]. The knowledge of l_D allows to calculate the relation between average defect distance L_d and the I_D/I_G -ratio. Defects have been intentionally generated using the strong optical fields at the tip. From the simultaneously recorded temporal evolution of the Raman scattering, L_d and I_D/I_G for the modified SWNT segment could be determined. Thereby, the simple quantitative relation $L_d = 0.4 \text{ nm} \cdot (I_D/I_G)^{-1}$ could be derived for the investigated metallic SWNTs, which is valid as long as $L_d > 10$ nm. For higher defect densities, a slightly more complex relation could also be derived and quantitatively defined.

10 Summary and outlook

In this work, single-walled carbon nanotubes have been studied using optical microscopy. The photoluminescence and Raman scattering properties can thereby be imaged on the single nanotube level. Photoluminescence in semiconducting SWNTs arises from the recombination of strongly bound excitons, owing to the one-dimensionality of nanotubes. These excitons are highly mobile, and react strongly to perturbations along the nanotube, such as specific defects or an inhomogeneous environment. Their propagation and local interactions are reflected in the spatial distribution of PL intensity and energy along single nanotubes. The Raman scattering spectra display the nanotube's vibrational properties, which are highly sensitive to e.g. doping, electron-phonon coupling and in particular structural defects. In this thesis, the PL and Raman scattering signals along single SWNTs have been imaged, revealing fundamental exciton properties and the microscopic origin of the specific defect-induced Raman response.

The spatial resolution in optical microscopy is limited by diffraction, which hinders the imaging and investigation of processes on length scales below the wavelength of light. In this work, this problem was overcome by the use of tip-enhanced near-field optical microscopy, a sophisticated approach providing a sub-diffraction spatial resolution of about 15 nm despite the use of light in the visible range. Here, a sharp gold tip is used as an optical antenna that strongly increases the excitation and emission rates in a nanoscale volume, thus circumventing the diffraction limit. Importantly, the resulting huge signal enhancement provides a very high sensitivity, in contrast to other near-field microscopy techniques. It allows for the spectral analysis of the PL and Raman scattering signals from a nanoscale sample volume. The positioning of the antenna with respect to the sample is achieved by means of shear-force microscopy, which further yields information on the sample topography.

The first key finding of this work is that exciton propagation can be described by one-dimensional diffusion with a diffusion length of 100 nm for the SWNTs studied here. The high mobility leads to a strong impact of single quenching sites on the PL intensity, which has been first observed here as photo-induced PL blinking. It becomes also apparent in high-resolution near-field PL images, which reveal that the PL intensity is often very inhomogeneous along individual nanotubes. These findings show that excitons are locally quenched at specific defects and the nanotube ends, which strongly reduces the PL in the vicinity. The influence range of quenching sites is apparent in the PL blinking characteristics and the nanoscale PL distribution. It is connected to the exciton diffusion

length, which can thereby be determined from both experimental observations. In order to evaluate the experimental data quantitatively, a highly flexible numerical model has been developed which simulates the exciton propagation and the complete imaging process. It allows for a direct comparison of theoretical and experimental data. By using the simple picture of 1D diffusion and assuming efficient exciton quenching at localized defect sites and nanotube ends, the experimental data could be well reproduced by the simulation and the exciton diffusion length was deduced quantitatively, yielding a value of 100 nm. In contrast to other studies on the exciton diffusion length in SWNTs [41, 60, 142–145], the quenching range could be visualized directly with nanoscale spatial resolution in this work.

The second key finding was the first observation of exciton localization in SWNTs at ambient conditions. This effect was found for DNA-wrapped SWNTs on a mica surface and leads to highly confined and bright PL emission spots on the nanotube, which have been visualized with tip-enhanced near-field microscopy. These spots can not be attributed to local quenching sites only, because their confinement requires such small quenching site distances that no bright PL would be expected. Instead, the bright emissive spots result from an increased exciton density at exciton energy minima due to a trapping-like process. This was verified by simultaneous nanoscale imaging of the PL intensity and energy, which revealed the correlation of bright PL with lower energy as expected for exciton localization at energy minima. The trapping process can be understood as directed exciton diffusion towards energy minima, owing to the additional driving force generated by energy gradients. The exciton energy variations have been attributed to inhomogeneous DNA-wrapping which locally reduces the energy. Complementary simulations considering combined diffusion and drift resulting from energy variations support this interpretation. They predict observable exciton localization for confined exciton energy minima with depths above 20 nm, in agreement with the experiments. Exciton localization in SWNTs had been reported before, but could only be observed at low temperatures and was identified indirectly. In this work, exciton localization in SWNTs was observed for the first time at ambient conditions and it was directly verified by near-field spectroscopic imaging of the local exciton density and energy.

In the last part of this work, the relation between localized structural defects in SWNTs and the characteristic Raman scattering response was investigated. This was done on metallic nanotubes exhibiting a very strong Raman signal for the available excitation wavelength. As the main result, it was found that the Raman D-band scattering process is strongly confined in the vicinity of localized defects. The D-band intensity was imaged with nanoscale resolution, revealing that the length scale of this scattering process is limited to about 2 nm around a defect. Furthermore, localized defect sites were intentionally generated using the strong optical fields at the gold tip, while recording the temporal evolution of the local Raman spectrum. From these experiments, a quantitative relation between defect density and Raman D-band intensity could be derived, which is highly relevant for carbon nanotube metrology via Raman spectroscopy.

It will be very interesting to image the Raman scattering response and photoluminescence simultaneously for the same semiconducting nanotube, in order to study the interaction of excitons with defects, which can be characterized by their Raman response. It was shown, also in this work, that this is possible but requires a variable excitation wavelength to maximize the Raman signal. For the semiconducting SWNTs studied here, the Raman scattering was generally too weak to be quantitatively evaluated, owing to the laser excitation at 632.8 nm. A future modification of the experimental setup by integrating different laser sources will open up new possibilities for the combined study of Raman scattering and PL properties with nanoscale spatial resolution.

A project aiming at the local visualization of electron-phonon coupling in current-carrying metallic SWNTs via tip-enhanced Raman spectroscopy has been started during this thesis work and is still ongoing. Such measurements will help to understand current flow in contacted nanotubes and the limiting factors for optimum device performance. Tip-enhanced near-field optical microscopy offers the capability to study nanotube properties in nanotechnological device arrangements under operating conditions.

In recent years, functional tip-enhanced near-field microscopes have become commercially available, which raises hope that this versatile technique is going to be used more widespread and will be applied as a regular metrology tool. Its potential could be demonstrated for the study of single molecule fluorescence and Raman scattering, nanoscale chemical composition of polymer blends, semiconducting nanowires and nanocrystals, DNA-strands, dye-labeled proteins on biological membranes and of course carbon nanotubes [77,90,91,94,100,173–175]. The possibilities are widespread and should be exploited further.

Appendix: Tip-enhanced Raman scattering on single-layer graphene

In this appendix, the preliminary results of tip-enhanced near-field experiments on graphene are reported. In analogy to chapter 9, it would be highly interesting to visualize the spatial extent of Raman D-band scattering at the graphene edge using TENOM. However, it has turned out that these experiments are very difficult and could not be successfully realized so far.

As discussed in the sections 2.4.2 and 9.1, the edge of a graphene flake gives rise to the Raman D-band in its vicinity. The segments of the edge exhibiting an armchair configuration can provide the necessary momentum to elastically scatter the electron/hole back to the K -point and thus enable the D-band scattering process [64, 176]. According to ref. 64, the possible length scale l_D of this process in real space, i.e. the maximum possible distance between excitation of the electron-hole pair and the edge, is determined by the virtual electron-hole lifetime and the charge carrier velocity. The estimated length scale for this interpretation would be 4 nm. A different picture is discussed in refs. 167 and 169, suggesting that the D-band localization reflects the phase-breaking length of the conduction electron.

There are different approaches to determine the length scale l_D of D-band localization near defects and the edge in graphene. As discussed for carbon nanotubes in chapter 9, the value of l_D is strongly connected to the relation between defect density and D-band intensity. It can be determined from an experiment where these two quantities are measured independently as has been done in ref. 166, where the defect density was quantified by scanning-tunneling microscopy. There, a value of $l_D = 2$ nm was found.

Another approach uses a spectroscopic line scan across the graphene edge. Here, the exciting laser spot is scanned in small steps from the outside to the inside of the graphene flake and the Raman spectrum is recorded at every position. The D-band intensity measured along this scan line is the convolution of the laser intensity distribution in scan direction and the profile of the D-band scattering probability near the edge. The former is the point-spread-function of the experiment and for a significant length l_D , the D-band profile would be broader than the PSF. The width of the PSF can be determined independently from the same scan by analyzing the 2D-band profile. It is given by the convolution of the PSF and a simple step-function [167]. Therefore, the PSF is the spatial derivative of the

2D-band profile. These experiments have been reported in ref. 167, where only an upper bound of $l_D < 40$ nm could be specified due to the diffraction-limited width of the PSF of several hundred nanometers. This approach would be significantly improved by the use of TENOM with its narrow PSF of only 15 nm width.

Fig. A.1 shows the graphene flake studied in this work and illustrates the above mentioned approach of a spectroscopic scan line from a diffraction limited experiment.

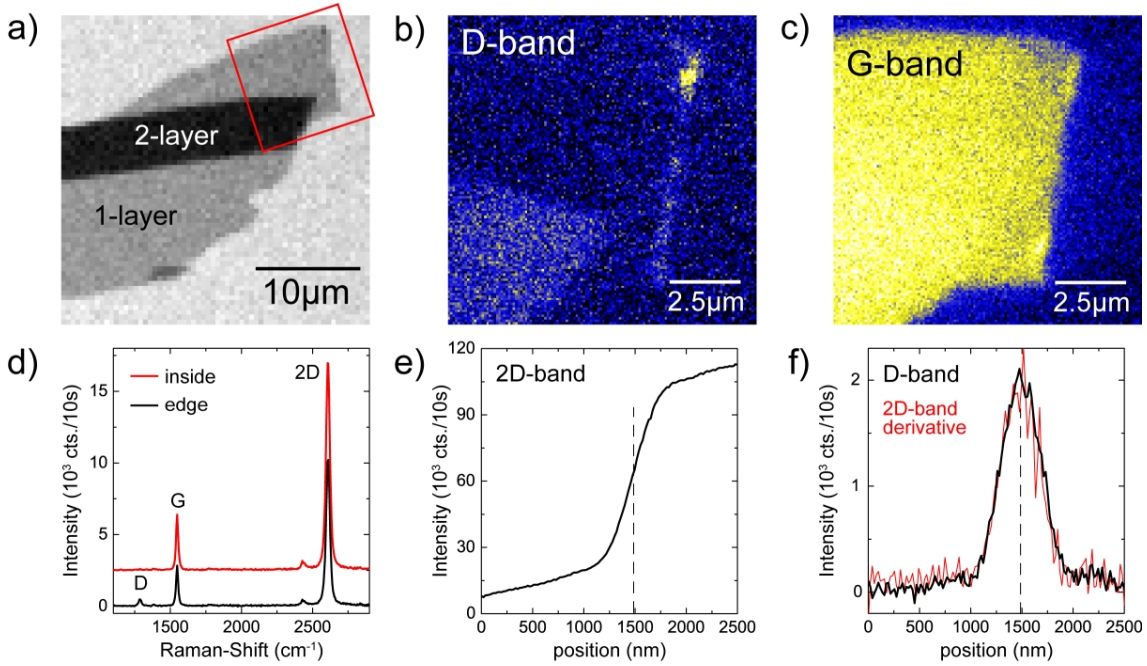


Figure A.1: Raman D-band scattering at a graphene edge. a) Elastic scattering image of the studied graphene flake. Parts of this flake are bi-layer graphene with a higher scattering contrast. Single-layer areas are identified by their specific Raman spectrum (see text). b) Raman D-band intensity image of the area marked by the red square in a. The signal was detected by APD (bandpass for $1300 \pm 100 \text{ cm}^{-1}$). D-band appears only at the edges and in the bi-layer area. c) Raman G-band intensity image of the same area using APD detection (bandpass for $1600 \pm 100 \text{ cm}^{-1}$). The G-band is rather homogeneous across the whole flake. d) Raman spectra of a position inside the graphene and at the edge. e) 2D-band intensity from a spectroscopic linescan across the edge (from outside to inside), plotted against scan position. The curve is the convolution of the PSF and a step-function located at the edge (position marked by the dashed line). f) D-band intensity from the same linescan (black line). Here, the curve can be described as the convolution of the PSF and the D-band scattering probability profile at the edge with a width of l_D . The red line is the spatial derivative of the 2D-intensity in e, which represents the PSF with a width of about 500 nm. The black and red curves are similar, which shows that l_D can not be resolved directly in such a diffraction-limited experiment.

The graphene was deposited on a transparent quartz cover slide, which can be used in the experimental TENOM setup. Fig. A.1a shows the elastic scattering image of the flake, where the back-scattered laser intensity was detected by APD. The investigated graphene

flake has single-layer and bi-layer areas that can be clearly distinguished by their scattering contrast and their specific Raman spectrum. The single-layer spectrum is characterized by a I_{2D}/I_G ratio of about two and a single Lorentzian lineshape for the 2D-band, as shown in Fig. A.1d [63]. The Raman D- and G-band intensity of this flake can be imaged using the APDs and specific bandpass filters (Figs. A.1b and c). Apparently, the D-band is localized to the single-layer edge and can also be detected in the bi-layer area. The G-band intensity is rather uniform across the whole flake. In Figs. A.1e and f, the results of a spectroscopic line scan are plotted. The 2D-band profile is reminiscent of an error function, the convolution of a Gaussian laser focus with a step function. Its derivative as shown in Fig. A.1f (red line) represents the experimental PSF with a width of about 500 nm. This value is larger than the theoretical width of 260 nm that should be achievable at a laser wavelength of 632.8 nm and NA=1.49. The deviation is probably due to the use of a quartz substrate which is not perfectly index-matched and slightly birefringent. The D-band profile in Fig. A.1f (black line) has the same width as the PSF and l_D can therefore not be inferred from this experiment.

The main difficulty for the realization of a TENOM experiment on graphene arises from the very strong selectivity to in-plane excitation. The 2D nature of single-layer graphene inhibits the absorption of light polarized perpendicular to the plane and this effect appears to be much more pronounced than the absorption anisotropy of carbon nanotubes. When using a radially polarized laser mode for measurements on graphene, the detectable Raman scattering signal is about an order of magnitude lower than for linear polarization, in rough agreement with the relative intensity of the in-plane components. This makes it almost impossible to detect the weak D-band signal at the edge, due to the lower signal-to-noise ratio. In particular, the tip-enhanced fields polarized along the tip axis are aligned perpendicular to the graphene in the standard TENOM configuration.

In order to circumvent this problem, the TENOM configuration was slightly modified for the experiments on graphene by tilting the tip axis and using a linearly polarized laser excitation. This configuration is illustrated in Fig. A.2a. The tip is tilted such that the projection of the axis is aligned along the laser polarization direction. Thereby, the tip should be efficiently excited by the in-plane polarized laser focus.

An additional difficulty that results from the 2D nature of graphene, is the reduced overall signal enhancement of the G- and 2D-band that can be expected in the TENOM measurement. Compared to 1D carbon nanotubes, the possible near-field to far-field contrast is only the square root for the 2D case, as already discussed in section 3.3.2. However, this should be less problematic for the quasi 1D distribution of the D-band at the edge.

To align the position of the tip inside the laser spot and optimize the signal enhancement, the tip was landed on the single-layer graphene and adjusted in x,y-direction while simultaneously observing the Raman spectrum. It was found that the G- and 2D-band intensity can be at least doubled in intensity, when the tip is brought into the focus. Subsequently,

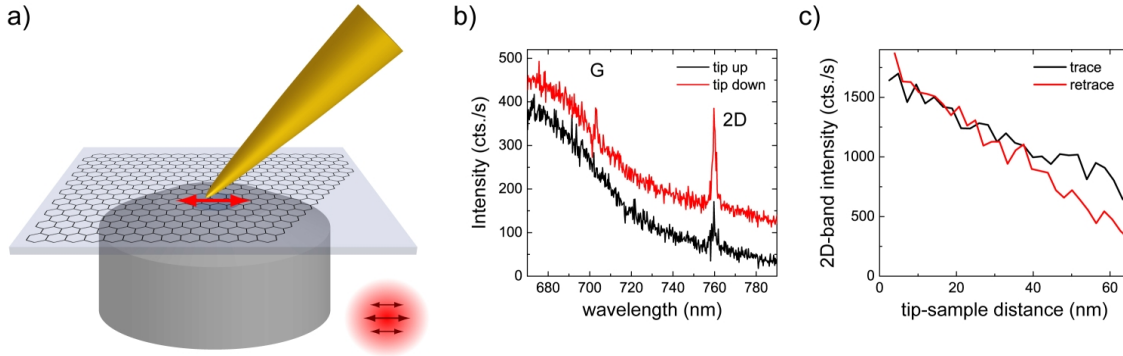


Figure A.2: Attempts for a TENOM experiment on graphene. a) Illustration of the modified TENOM setup for a near-field measurement on graphene. Because graphene can only be excited by in-plane optical fields, the tip was tilted in order to provide an in-plane component with the enhanced field at the tip, polarized along the tip axis. For excitation, a linearly polarized laser was used, with a polarization aligned along the projection of the tip axis to maximize excitation of the tip. b) Raman spectrum of graphene with the tip retracted by 70 nm (black line) and landed on the graphene (red line). An enhancement effect for the G- and 2D-band is clearly visible, the intense background is the PL from the gold tip. The spectra are offset by 100 cts. for clarity. c) 2D-band intensity from a spectroscopic approach curve, plotted against tip-sample distance. The intensity increases rather linearly and no near-field enhancement confined to small distances can be observed (compare Fig. 3.6). Hence, the enhancement as seen in b) does not arise from a near-field effect and can be explained as a simple back-reflection at the lower tip surface.

an approach curve was recorded to study the distance dependence of this enhancement effect and verify a possible near-field contribution. Raman spectra were acquired at every tip-sample distance from 70 – 0 nm in steps of about 2.5 nm. The spectra for the tip landed and retracted by 70 nm are shown in Fig. A.2b, revealing a significant signal enhancement of the G- and 2D-band. However, the distance dependence of the 2D-intensity plotted in Fig. A.2c is not characteristic for a near-field enhancement effect (compare Fig. 3.6). The intensity increases slowly and continuous with decreasing distance and no confined interaction on a length scale of few nanometers is seen.

The origin of this long-range enhancement effect is probably the reflection of the laser at the bottom side of the gold tip. This leads to a stronger excitation of the graphene under the tip. Since this effect is not confined to the very tip end, the resulting PSF is not as narrow as the tip diameter and a significant improvement of the spatial resolution can not be expected. Indeed, spectroscopic line scans across the edge with the tip landed and aligned did not show any indication of narrower D-band confinement. These experiments point out the importance to verify the near-field nature of tip-enhancement effects by recording approach curves. Tip-enhancement alone does not necessarily yield an improved spatial resolution, which is always the result of a confined enhancement effect.

In a recent publication, a new experimental approach to determine the D-band extension at the graphene edge using conventional far-field optics has been reported [169]. Instead of scanning across the edge, the focus position is fixed on the edge and its z-position is scanned. This means that the focal area is varied which changes the I_D/I_G ratio. The G-band intensity results from half of the focal area, whereas the D-band intensity arises from a narrow stripe with a width of l_D and a length corresponding to the focus size. Despite the focus size of a few hundred nanometers, l_D can be determined in these experiments with nanometer accuracy. A value of $l_D = 3$ nm has been deduced at room temperature and was also determined for temperatures down to 1.55 K, where l_D increases to about 10 nm. This temperature dependence is discussed as evidence for the interpretation that the D-band localization reflects the phase-breaking length of the electron.

Although the D-band scattering length can apparently also be studied with a far-field optical measurement, it would nevertheless be tempting to realize high-resolution near-field Raman imaging of graphene. Possible applications could be for example the local imaging of doping and the edge type. This would be of high interest for the nanoscale characterization of graphene or graphene-nanoribbon devices. However, TENOM on graphene could not be realized so far, owing to the difficulties as discussed in this section. Strongly increased field enhancement will be necessary to discriminate true near-field effects from the far-field background and sophisticated optical antenna designs could be used to provide the relevant in-plane polarization.

Bibliography

- [1] R. Saito, G. Dresselhaus, and M. S. Dresselhaus. *Physical Properties of Carbon Nanotubes*. Imperial College Press, London, 1998.
- [2] S. Reich, C. Thomsen, and J. Maultzsch. *Carbon Nanotubes: Basic Concepts and Physical Properties*. Wiley-VCH, Berlin, 2004.
- [3] Q. Cao and J. A. Rogers. Ultrathin Films of Single-Walled Carbon Nanotubes for Electronics and Sensors: A Review of Fundamental and Applied Aspects. *Adv. Mater.*, 20:1–25, 2008.
- [4] T. Ando. Excitons in Carbon Nanotubes. *J. Phys. Soc. Jap.*, 66:1066–1073, 1997.
- [5] F. Wang, G. Dukovic, L. E. Brus, and T. F. Heinz. The optical resonances in carbon nanotubes arise from excitons. *Science*, 308:838–841, 2005.
- [6] M. S. Dresselhaus, A. Jorio, M. Hofmann, G. Dresselhaus, and R. Saito. Perspectives on Carbon Nanotubes and Graphene Raman Spectroscopy. *Nano Lett.*, 10:751–758, 2010.
- [7] S. M. Bachilo, M. S. Strano, C. Kittrell, R. H. Hauge, R. Smalley, and R. B. Weisman. Structure-assigned optical spectra of single-walled carbon nanotubes. *Science*, 298:2361–2366, 2002.
- [8] L. Novotny and B. Hecht. *Principles of nano-optics*. Cambridge University Press, Cambridge, 2006.
- [9] D. W. Pohl, W. Denk, and M. Lanz. Optical stethoscopy: Image recording with resolution $\lambda/20$. *Appl. Phys. Lett.*, 44:651–653, 1984.
- [10] E. Betzig and J. K. Trautman. Near-field optics: Microscopy, spectroscopy, and surface modification beyond the diffraction limit. *Science*, 257:189–195, 1992.
- [11] M. Sandtke and L. Kuipers. Spatial distribution and near-field coupling of surface plasmon polariton Bloch modes. *Phys. Rev. B*, 77:235439, 2008.
- [12] J. Wessel. Surface-enhanced optical microscopy. *J. Opt. Soc. Am. B*, 2:1538–1541, 1985.
- [13] A. Hartschuh, E. J. Sánchez, X. S. Xie, and L. Novotny. High-resolution near-field raman microscopy of single-walled carbon nanotubes. *Phys. Rev. Lett.*, 90:095503–4, 2003.

- [14] A. Hartschuh, H. Qian, A. J. Meixner, N. Anderson, and L. Novotny. Nanoscale optical imaging of excitons in single-walled carbon nanotubes. *Nano Lett.*, 5:2310–2313, 2005.
- [15] S. Iijima and T. Ichihashi. Single-shell carbon nanotubes of 1-nm diameter. *Nature*, 363:603–605, 1993.
- [16] A. K. Geim and K. S. Novoselov. The rise of graphene. *Nature Mater.*, 6:183–191, 2007.
- [17] S. Reich, J. Maultzsch, C. Thomsen, and P. Ordejon. Tight-binding description of graphene. *Phys. Rev. B*, 66:0353412, 2002.
- [18] P. T. Araujo, S. K. Doorn, S. Kilina, S. Tretiak, E. Einarsson, S. Maruyama, H. Chacham, M. A. Pimenta, and A. Jorio. Third and Fourth Optical Transitions in Semiconducting Carbon Nanotubes. *Phys. Rev. B*, 98:067401, 2007.
- [19] H. Kataura, Y. Kumazawa, Y. Maniwa, I. Umezū, S. Suzuki, Y. Ohtsuka, and Y. Achiba. Optical properties of single-wall carbon nanotubes. *Synthetic Mat.*, 103:2555–2558, 1999.
- [20] H. Ajiki and T. Ando. Aharonov-Bohm Effect in Carbon Nanotubes. *Physica B*, 201:349–352, 1994.
- [21] H. Ajiki. Magneto-optical spectra of carbon nanotubes: effect of Aharonov–Bohm flux on depolarization effect. *Physica B*, 323:206–208, 2002.
- [22] G. S. Duesberg, I. Loa, M. Burghard, K. Syassen, and S. Roth. Polarized Raman Spectroscopy on Isolated Single-Wall Carbon Nanotubes. *Phys. Rev. Lett.*, 85:5436–5439, 2000.
- [23] M. F. Islam, D. E. Milkie, C. L. Kane, A. G. Yodh, and J. M. Kikkawa. Direct Measurement of the Polarized Optical Absorption Cross Section of Single-Wall Carbon Nanotubes. *Phys. Rev. Lett.*, 93:037404, 2004.
- [24] Y. Miyauchi, M. Oba, and S. Maruyama. Cross-polarized optical absorption of single-walled nanotubes by polarized photoluminescence excitation spectroscopy. *Phys. Rev. B*, 74:205440, 2006.
- [25] J. Lefebvre and P. Finnie. Excited Excitonic States in Single-Walled Carbon Nanotubes. *Nano Lett.*, 8:1890–1895, 2008.
- [26] A. G. Walsh, A. N. Vamivakas, Y. Yin, S. B. Cronin, M. S. Ünlü, B. B. Goldberg, and A. K. Swan. Scaling of exciton binding energy with external dielectric function in carbon nanotubes. *Physica E*, 40:2375–2379, 2007.
- [27] S. Abe. Exciton versus Interband Absorption in Peierls Insulators. *J. Phys. Soc. Jap.*, 58:62–65, 1989.

-
- [28] V. Perebeinos, J. Tersoff, and P. Avouris. Scaling of excitons in carbon nanotubes. *Phys. Rev. Lett.*, 92:257402–257405, 2004.
- [29] R. J. Elliott. Intensity of Optical Absorption by Excitons. *Phys. Rev.*, 108:1384–1389, 1957.
- [30] C. L. Kane and E. J. Mele. Electron interactions and scaling relations for optical excitations in carbon nanotubes. *Phys. Rev. Lett.*, 93:197402, 2004.
- [31] R. B. Capaz, C. D. Spataru, S. Ismail-Beigi, and S. G. Louie. Diameter and chirality dependence of exciton properties in carbon nanotubes. *Phys. Rev. B*, 74:121401(R), 2006.
- [32] T. Hertel, V. Perebeinos, J. Crochet, K. Arnold, M. Kappes, and P. Avouris. Intersubband Decay of 1-D Exciton Resonances in Carbon Nanotubes. *Nano Letters*, 8:87–91, 2008.
- [33] J. Maultzsch, R. Pomraenke, S. Reich, E. Chang, D. Prezzi, A. Ruini, E. Molinari, M. S. Strano, C. Thomsen, and C. Lienau. Exciton binding energies in carbon nanotubes from two-photon photoluminescence. *Phys. Rev. B*, 72:241402(R), 2005.
- [34] G. Dukovic, F. Wang, D. Song, M. Y. Sfeir, T. F. Heinz, and L. E. Brus. Structural Dependence of Excitonic Optical Transitions and Band-Gap Energies in Carbon Nanotubes. *Nano Lett.*, 5:2314–2318, 2005.
- [35] Y. Ohno, S. Iwasaki, Y. Murakami, S. Kishimoto, S. Maruyama, and T. Mizutani. Chirality-dependent environmental effects in photoluminescence of single-walled carbon nanotubes. *Phys. Rev. B.*, 73:235427, 2006.
- [36] O. Kiowski, S. Lebedkin, F. Hennrich, S. Malik, H. Rösner, K. Arnold, C. Sürgers, and M. M. Kappes. Photoluminescence microscopy of carbon nanotubes grown by chemical vapor deposition: Influence of external dielectric screening on optical transition energies. *Phys. Rev. B*, 75:075421, 2007.
- [37] A. G. Walsh, A. N. Vamivakas, Y. Yin, S. B. Cronin, M. S. Ünlü, B. B. Goldberg, and A. K. Swan. Screening of Excitons in Single, Suspended Carbon Nanotubes. *Nano Lett.*, 7:1485–1488, 2007.
- [38] L. Lüer, S. Hoseinkhani, D. Polli, J. Crochet, T. Hertel, and G. Lanzani. Size and mobility of excitons in (6,5) carbon nanotubes. *Nature Phys.*, 5:54–58, 2008.
- [39] Y.-Z. Ma, M. W. Graham, G. R. Fleming, A. A. Green, and M. C. Hersam. Ultrafast Exciton Dephasing in Semiconducting Single-Walled Carbon. *Phys. Rev. Lett.*, 101:217402, 2008.
- [40] Y. Miyauchi, H. Hirori, K. Matsuda, and Y. Kanemitsu. Radiative lifetimes and coherence lengths of one-dimensional excitons in single-walled carbon nanotubes. *Phys. Rev. B*, 80:081410(R), 2009.

- [41] L. Cognet, D. T. Tysboulski, J.-D. R. Rocha, C. D. Doyle, J. M. Tour, and R. B. Weisman. Stepwise quenching of exciton fluorescence in carbon nanotubes by single-molecule reactions. *Science*, 316:1465–1468, 2007.
- [42] T. Gokus, A. Hartschuh, H. Harutyunyan, M. Allegrini, F. Hennrich, M. Kappes, A. A. Green, M. C. Hersam, P. T. Araujo, and A. Jorio. Exciton decay dynamics in individual carbon nanotubes at room temperature. *Appl. Phys. Lett.*, 92:153116, 2008.
- [43] C. Manzoni, A. Gambetta, E. Menna, M. Meneghetti, G. Lanzani, and G. Cerullo. Intersubband exciton relaxation dynamics in single-walled carbon nanotubes. *Phys. Rev. Lett.*, 94:207401–207404, 2005.
- [44] L. Lüer, J. Crochet, T. Hertel, G. Cerullo, and G. Lanzani. Ultrafast Excitation Energy Transfer in Small Semiconducting Carbon Nanotube Aggregates. *ACS Nano*, 4:4265–4273, 2010.
- [45] C. D. Spataru, S. Ismail-Beigi, R. B. Capaz, and S. G. Louie. Theory and Ab Initio Calculation of Radiative Lifetime of Excitons in Semiconducting Carbon Nanotubes. *Phys. Rev. Lett.*, 95:247402–4, 2005.
- [46] V. Perebeinos, J. Tersoff, and P. Avouris. Radiative Lifetime of Excitons in Carbon Nanotubes. *Nano Lett.*, 5:2495–2499, 2005.
- [47] F. Wang, G. Dukovic, L. E. Brus, and T. F. Heinz. Time-resolved fluorescence of carbon nanotubes and its implication for radiative lifetimes. *Phys. Rev. Lett.*, 92:177401, 2004.
- [48] A. Hagen, M. Steiner, M. B. Raschke, C. Lienau, T. Hertel, H. Qian, A. J. Meixner, and A. Hartschuh. Exponential decay lifetimes of excitons in individual single-walled carbon nanotubes. *Phys. Rev. Lett.*, 95:197401, 2005.
- [49] S. Berciaud, L. Cognet, and B. Lounis. Luminescence Decay and the Absorption Cross Section of Individual Single-Walled Carbon Nanotubes. *Phys. Rev. Lett.*, 101:077402, 2008.
- [50] M. J. O’Connell, S. M. Bachilo, C. B. Huffman, V. C. Moore, M. S. Strano, E. H. Haroz, K. L. Rialon, P. J. Boul, W. H. Noon, C. Kittrell, J. Ma, R. H. Hauge, R. B. Weisman, and R. Smalley. Band gap fluorescence from individual single-walled carbon nanotubes. *Science*, 297:593–596, 2002.
- [51] J. Lefebvre, D. G. Austing, J. Bond, and P. Finnie. Photoluminescence imaging of suspended single-walled carbon nanotubes. *Nano Lett.*, 6:1603–1608, 2006.
- [52] J. Crochet, M. Clemens, and T. Hertel. Quantum Yield Heterogeneities of Aqueous Single-Wall Carbon Nanotube Suspensions. *J. Am. Chem. Soc.*, 129:8058–8059, 2007.

-
- [53] S.-Y. Ju, W. P. Kopcha, and F. Papadimitrakopoulos. Brightly Fluorescent Single-Walled Carbon Nanotubes via an Oxygen-Excluding Surfactant Organization. *Science*, 323:1319–1323, 2009.
- [54] V. Perebeinos and P. Avouris. Phonon and Electronic Nonradiative Decay Mechanisms of Excitons in Carbon Nanotubes. *Phys. Rev. Lett.*, 101:057401, 2008.
- [55] H. Qian, C. Georgi, N. Anderson, A. A. Green, M. C. Hersam, L. Novotny, and A. Hartschuh. Exciton energy transfer in pairs of single-walled carbon nanotubes. *Nano Lett.*, 8:1363–1367, 2008.
- [56] M. S. Arnold, S. I. Stupp, and M. C. Hersam. Enrichment of single-walled carbon nanotubes by diameter in density gradients. *Nano Lett.*, 5:713–718, 2005.
- [57] M. S. Strano, C. B. Huffman, V. C. Moore, M. J. O’Connell, E. H. Haroz, J. Hubbard, M. Miller, K. Rialon, C. Kittrell, S. Ramesh, R. H. Hauge, and R. E. Smalley. Reversible, Band-Gap-Selective Protonation of Single-Walled Carbon Nanotubes in Solution. *J. Phys. Chem. B*, 107:6979–6985, 2003.
- [58] G. Dukovic, B. E. White, Z. Zhou, F. Wang, S. Jockusch, M. L. Steigerwald, T. F. Heinz, R. A. Friesner, N. J. Turro, and L. E. Brus. Reversible Surface Oxidation and Efficient Luminescence Quenching in Semiconductor Single-Wall Carbon Nanotubes. *J. Am. Chem. Soc.*, 126:15269–15276, 2004.
- [59] F. Wang, G. Dukovic, E. Knoesel, L. E. Brus, and T. F. Heinz. Observation of rapid Auger recombination in optically excited semiconducting carbon nanotubes. *Phys. Rev. B*, 70:241403, 2004.
- [60] T. Hertel, S. Himmelein, T. Ackermann, D. Stich, and J. Crochet. Diffusion Limited Photoluminescence Quantum Yields in 1-D Semiconductors: Single-Wall Carbon Nanotubes. *ACS Nano*, 2010. published online, DOI: 10.1021/nn101612b.
- [61] Y. Z. Ma, L. Valkunas, S. L. Dexheimer, S. M. Bachilo, and G. Fleming. Femtosecond spectroscopy of optical excitations in single-walled carbon nanotubes: Evidence for exciton-exciton annihilation. *Phys. Rev. Lett.*, 94:157402, 2005.
- [62] M. S. Dresselhaus, G. Dresselhaus, R. Saito, and A. Jorio. Raman spectroscopy of carbon nanotubes. *Phys. Reports*, 409:47–99, 2005.
- [63] A. C. Ferrari. Raman spectroscopy of graphene and graphite: Disorder, electron–phonon coupling, doping and nonadiabatic effects. *Solid State Commun.*, 143:47–57, 2007.
- [64] C. Casiraghi, A. Hartschuh, H. Qian, S. Piscanec, C. Georgi, A. Fasoli, K. S. Novoselov, D. M. Basko, and A. Ferrari. Raman Spectroscopy of Graphene Edges. *Nano Lett.*, 9:1433–1441, 2009.

- [65] P. T. Araujo, C. Fantini, M. M. Lucchese, M. S. Dresselhaus, and A. Jorio. The effect of environment on the radial breathing mode of supergrowth single wall carbon nanotubes. *Appl. Phys. Lett.*, 95:261902, 2009.
- [66] S. Piscanec, M. Lazzeri, J. Robertson, A. C. Ferrari, and F. Mauri. Optical phonons in carbon nanotubes: Kohn anomalies, Peierls distortions, and dynamic effects. *Phys. Rev. B*, 75:035427, 2007.
- [67] M. S. Dresselhaus, G. Dresselhaus, A. Jorio, A. G. Souza Filho, and R. Saito. Raman spectroscopy on isolated single wall carbon nanotubes. *Carbon*, 40:2043–2061, 2002.
- [68] M. Oron-Carl, F. Hennrich, M. Kappes, H. v. Löhneysen, and R. Krupke. On the electron-phonon coupling of individual single-walled carbon nanotubes. *Nano Lett.*, 5:1761–1767, 2005.
- [69] M. Fouquet, H. Telg, J. Maultzsch, Y. Wu, B. Chandra, J. Hone, T. F. Heinz, and C. Thomsen. Longitudinal Optical Phonons in Metallic and Semiconducting Carbon Nanotubes. *Phys. Rev. Lett.*, 102:075501, 2009.
- [70] M. S. Strano, C. A. Dyke, M. L. Usrey, P. W. Barone, M. J. Allen, H. Shan, C. Kittrell, R. H. Hauge, J. M. Tour, and R. E. Smalley. Electronic structure control of single-walled carbon nanotube functionalization. *Science*, 301:1519–1522, 2003.
- [71] I. O. Maciel, N. Anderson, M. A. Pimenta, A. Hartschuh, H. Qian, M. Terrones, H. Terrones, J. Campos-Delgado, A. M. Rao, L. Novotny, and A. Jorio. Electron and phonon renormalization near charged defects in carbon nanotubes. *Nature Mater.*, 7:878–883, 2008.
- [72] I. O. Maciel, J. Campos-Delgado, E. Cruz-Silva, M. A. Pimenta, B. G. Sumpter, V. Meunier, F. López-Urías, E. Muñoz-Sandoval, H. Terrones, M. Terrones, and A. Jorio. Synthesis, Electronic Structure, and Raman Scattering of Phosphorus-Doped Single-Wall Carbon Nanotubes. *Nano Lett.*, 9:2267–2272, 2009.
- [73] A. Lewis, M. Isaacson, A. Harootunian, and A. Muray. Development of a 500 Å resolution light microscope. *Ultramicroscopy*, 13:227–231, 1984.
- [74] A. Harootunian, E. Betzig, M. Isaacson, and A. Lewis. Super-resolution fluorescence near-field scanning optical microscopy. *Appl. Phys. Lett.*, 49:674–676, 1986.
- [75] E. Betzig, J. K. Trautman, T. D. Harris, J. S. Weiner, and R. L. Kostelak. Breaking the Diffraction Barrier: Optical Microscopy on a Nanometric Scale. *Science*, 251:1468–1470, 1991.
- [76] E. Betzig, P. L. Finn, and J. S. Weiner. Combined shear force and near-field scanning optical microscopy. *Appl. Phys. Lett.*, 60:2484–2486, 1992.

-
- [77] J. Steidtner and B. Pettinger. Tip-enhanced Raman spectroscopy and microscopy on single dye molecules with 15 nm resolution. *Phys. Rev. Lett.*, 100:236101–4, 2008.
- [78] H. G. Frey, F. Keilmann, A. Kriele, and R. Guckenberger. Enhancing the resolution of scanning near-field optical microscopy by a metal tip grown on an aperture probe. *Appl. Phys. Lett.*, 81:530–532, 2002.
- [79] H. G. Frey, S. Witt, K. Felderer, and R. Guckenberger. High-resolution imaging of single fluorescent molecules with the optical near-field of a metal tip. *Phys. Rev. Lett.*, 93:200801–200804, 2004.
- [80] T. H. Taminiau, F. D. Stefani, F. B. Segerink, and N. F. van Hulst. Optical antennas direct single-molecule emission. *Nature Photon.*, 2:234–237, 2008.
- [81] R. Hillenbrand and F. Keilmann. Material-specific mapping of metal/ semiconductor/ dielectric nanosystems at 10 nm resolution by backscattering near-field optical microscopy. *Appl. Phys. Lett.*, 80:25–27, 2002.
- [82] R. Hillenbrand, Taubner T., and F. Keilmann. Phonon-enhanced light matter interaction at the nanometre scale. *Nature*, 418:159–27, 2002.
- [83] A. J. Huber, F. Keilmann, J. Wittborn, J. Aizpurua, and R. Hillenbrand. Terahertz Near-Field Nanoscopy of Mobile Carriers in Single Semiconductor Nanodevices. *Nano Lett.*, 8:3766–3770, 2008.
- [84] A. J. Huber, A. Ziegler, T. Köck, and R. Hillenbrand. Phonon-enhanced light matter interaction at the nanometre scale. *Nature Nanotech.*, 4:153–157, 2009.
- [85] M. Fleischmann, P. J. Hendra, and A. J. McQuillan. Raman spectra of pyridine adsorbed at a silver electrode. *Chem. Phys. Lett.*, 26:163–166, 1974.
- [86] M. Moskovits. Surface-enhanced Raman spectroscopy: a brief retrospective. *J. Raman Spectrosc.*, 36:485–496, 2005.
- [87] S. M. Stöckle, Y. D. Suh, V. Deckert, and R. Zenobi. Nanoscale chemical analysis by tip-enhanced raman spectroscopy. *Chem. Phys. Lett.*, 318:131–136, 2000.
- [88] M. S. Anderson. Locally enhanced Raman spectroscopy with an atomic force microscope. *Appl. Phys. Lett.*, 76:3130–, 2000.
- [89] A. Tarun, N. Hayazawa, M. Motohashi, and S. Kawata. Highly efficient tip-enhanced Raman spectroscopy and microscopy of strained silicon. *Rev. Sci. Instrum.*, 79:913706–10, 2007.
- [90] E. Bailo and V. Deckert. Tip-enhanced Raman spectroscopy of single RNA strands: Towards a novel direct-sequencing method. *Angew. Chem. Intern. Ed.*, 47:1658–1661, 2008.

- [91] D. Zhang, U. Heinemeyer, C. Stanciu, M. Sackrow, K. Braun, L. E. Henne-
mann, X. Wang, R. Scholz, F. Schreiber, and A. J. Meixner. Nanoscale Spectro-
scopic Imaging of Organic Semiconductor Films by Plasmon-Polariton Coupling.
Phys. Rev. Lett., 104:056601, 2010.
- [92] E. J. Sánchez, L. Novotny, and X. S. Xie. Near-Field Fluorescence Microscopy Based
on Two-Photon Excitation with Metal Tips. *Phys. Rev. Lett.*, 82:4014–4017, 1999.
- [93] A. Hartschuh. Tip-enhanced near-field optical microscopy. *Angew. Chem. Int. Ed.*,
47:8178–8198, 2008.
- [94] L. G. Cançado, A. Jorio, A. Ismach, E. Joselevich, A. Hartschuh, and L. Novotny.
Mechanism of Near-Field Raman Enhancement in One-Dimensional Systems.
Phys. Rev. Lett., 103:186101, 2009.
- [95] L. Novotny and S. Stranick. Near-field optical microscopy and spectroscopy with
pointed probes. *Annu. Rev. Phys. Chem.*, 57:303–31, 2006.
- [96] A. L. Demming, F. Festy, and D. Richards. Plasmon resonances on metal tips:
Understanding tip-enhanced Raman scattering. *J. Chem. Phys.*, 122:184716, 2005.
- [97] A. V. Goncharenko, H.-C. Chang, and J.-K. Wang. Electric near-field enhancing
properties of a finite-size metal conical nano-tip. *Ultramicroscopy*, 107:151–157, 2007.
- [98] W. Zhang, X. Cui, and O. J. F. Martin. Local field enhancement of an infinite conical
metal tip illuminated by a focused beam. *J. Raman Spectr.*, 40:1338–1342, 2009.
- [99] L. Novotny. Effective wavelength scaling for optical antennas. *Phys. Rev. Lett.*,
98:266802–4, 2007.
- [100] P. Anger, P. Bharadwaj, and L. Novotny. Enhancement and quenching of single
molecule fluorescence. *Phys. Rev. Lett.*, 96:113002, 2006.
- [101] S. Lebedkin, K. Arnold, F. Hennrich, R. Krupke, B. Renker, and M. M.
Kappes. FTIR-luminescence mapping of dispersed single-walled carbon nanotubes.
New. J. Phys., 5:140.1–140.11, 2003.
- [102] M. Böhmler, N. Hartmann, C. Georgi, F. Hennrich, A. A. Green, M. C. Hersam, and
A. Hartschuh. Enhancing and Redirecting Carbon Nanotube Photoluminescence by
an Optical Antenna. *Optics Express*, 18:16443–16451, 2010.
- [103] J. Stadler, C. Stanciu, C. Stupperich, and A. J. Meixner. Tighter focusing with a
parabolic mirror. *Optics Lett.*, 33:681–683, 2008.
- [104] S. W. Hell. Far-Field Optical Nanoscopy. *Science*, 316:1153–1158, 2007.
- [105] M. J. Rust, M. Bates, and X. Zhuang. Sub-diffraction-limit imaging by stochastic
optical reconstruction microscopy (STORM). *Nature Methods*, 3:793–796, 2006.

-
- [106] E. Betzig, G. H. Patterson, R. Sougrat, O. W. Lindwasser, S. Olenych, J. S. Bonifacino, M. W. Davidson, J. Lippincott-Schwartz, and H. F. Hess. Imaging intracellular fluorescent proteins at nanometer resolution. *Science*, 313:1642–1645, 2006.
- [107] L. Cognet, D. A. Tsyboulski, and R. B. Weisman. Subdiffraction far-field imaging of luminescent single-walled carbon nanotubes. *Nano Lett.*, 8:749–753, 2008.
- [108] K. Karrai and R. D. Grober. Piezoelectric tip-sample distance control for near field optical microscopes. *Appl. Phys. Lett.*, 66:1842–1844, 1995.
- [109] T. R. Albrecht, P. Grütter, D. Horne, and D. Rugar. Frequency modulation detection using high-Q cantilevers for enhanced force microscope sensitivity. *J. Appl. Phys.*, 69:668–673, 1991.
- [110] A. G. T. Ruiter, K. O. van der Werf, J. A. Veerman, M. F. Garcia-Parajo, W. H. J. Rensen, and N. F. van Hulst. Tuning fork shear-force feedback. *Ultramicroscopy*, 71:149–157, 1998.
- [111] B. Ren, G. Picardi, and B. Pettinger. Preparation of gold tips suitable for tip-enhanced Raman spectroscopy and light emission by electrochemical etching. *Rev. Sci. Instrum.*, 75:837–841, 2008.
- [112] C. Williams and D. Roy. Fabrication of gold tips suitable for tip-enhanced Raman spectroscopy. *J. Vac. Sci. Technol. B*, 26:1761–1764, 2008.
- [113] L. Eligal, F. Culfaz, V. McCaughan, N. I. Cade, and D. Richards. Etching gold tips suitable for tip-enhanced near-field optical microscopy. *Rev. Sci. Instrum.*, 80:033701, 2009.
- [114] M. S. Arnold, A. A. Green, J. F. Hulvat, S. I. Stupp, and M. C. Hersam. Sorting carbon nanotubes by electronic structure using density differentiation. *Nature Nanotech.*, 1:60–65, 2006.
- [115] A. A. Green and M. C. Hersam. Ultracentrifugation of single-walled nanotubes. *Materials Today*, 10:59–60, 2007.
- [116] M. Zheng, A. Jagota, E. D. Semke, B. A. Diner, R. S. Mclean, S. R. Lustig, R. E. Richardson, and N. G. Tassi. DNA-assisted dispersion and separation of carbon nanotubes. *Nature Mater.*, 2:338–342, 2003.
- [117] M. Beversluis, A. Bouhelier, and L. Novotny. Continuum generation from single gold nanostructures through near-field mediated intraband transitions. *Phys. Rev. B*, 68:115433–10, 2003.
- [118] A. Jorio, M. S. Dresselhaus, and G. Dresselhaus, editors. *Carbon Nanotubes*, volume 111 of *Topics in Applied Physics*. Springer, Berlin / Heidelberg, 2008.

- [119] P. Cherukuri, S. M. Bachilo, S. H. Litovsky, and R. B. Weisman. Near-Infrared Fluorescence Microscopy of Single-Walled Carbon Nanotubes in Phagocytic Cells. *J. Am. Chem. Soc.*, 126:15638–15639, 2004.
- [120] K. Welsher, Z. Liu, D. Daranciang, and H. Dai. Selective probing and imaging of cells with single walled carbon nanotubes as near-infrared fluorescent molecules. *Nano Lett.*, 8:586–590, 2008.
- [121] B. C. Satishkumar, L. O. Brown, Y. Gao, C.-C. Wang, H.-L. Wang, and S. K. Doorn. Reversible fluorescence quenching in carbon nanotubes for biomolecular sensing. *Nature Nanotech.*, 2:560–564, 2007.
- [122] A. Hartschuh, H. N. Pedrosa, L. Novotny, and T. D. Krauss. Simultaneous fluorescence and Raman scattering from single carbon nanotubes. *Science*, 301:1354–1356, 2003.
- [123] H. Htoon, M. J. O’Connell, P. J. Cox, S. K. Doorn, and V. I. Klimov. Low temperature emission spectra of individual single-walled carbon nanotubes: Multiplicity of subspecies within single-species nanotube-ensembles. *Phys. Rev. Lett.*, 93:027401, 2004.
- [124] O. Kiowski, S. Lebedkin, F. Henrich, and M. M. Kappes. Single-walled carbon nanotubes show stable emission and simple photoluminescence spectra with weak excitation sidebands at cryogenic temperatures. *Phys. Rev. B*, 76:075422, 2007.
- [125] L. J. Carlson, S. E. Maccagnano, J. Silcox, and T. D. Krauss. Fluorescence efficiency of individual carbon nanotubes. *Nano Lett.*, 7:3698–3703, 2007.
- [126] J. Lefebvre, P. Finnie, and Y. Homma. Temperature-dependent photoluminescence from single-walled carbon nanotubes. *Phys. Rev. B*, 70:045419, 2004.
- [127] K. Matsuda, Y. Kanemitsu, K. Irie, T. Saiki, T. Someya, Y. Miyauchi, and S. Maruyama. Photoluminescence intermittency in an individual single-walled carbon nanotube at room temperature. *Appl. Phys. Lett.*, 86:123116, 2005.
- [128] M. J. O’Connell, E. E. Eibergen, and S. K. Doorn. Chiral selectivity in the charge-transfer bleaching of single-walled carbon-nanotube spectra. *Nature Mater.*, 4:410–418, 2005.
- [129] P. G. Collins, K. Bradley, M. Ishigami, and A. Zettl. Extreme Oxygen Sensitivity of Electronic Properties of Carbon Nanotubes. *Science*, 287:1801–1804, 2000.
- [130] D. C. Sorescu, K. D. Jordan, and P. Avouris. Theoretical Study of Oxygen Adsorption on Graphite and the (8,0) Single-walled Carbon Nanotube. *J. Phys. Chem. B*, 105:11227–11232, 2001.

-
- [131] V. A. Margulis and E. E. Muryumin. Atomic oxygen chemisorption on the sidewall of zigzag single-walled carbon nanotubes. *Phys. Rev. B*, 75:035429, 2007.
- [132] R. B. Weisman, S. M. Bachilo, and D. Tsyboulski. Fluorescence spectroscopy of single-walled carbon nanotubes in aqueous suspension. *Appl. Phys. A*, 78:1111–1116, 2004.
- [133] T. Savage, S. Bhattacharya, B. Sadanadan, J. Gaillard, Tritt, T. M., Y.-P. Sun, Y. Wu, S. Nayak, R. Car, N. Marzari, P. M. Ajayan, and A. M. Rao. Photoinduced oxidation of carbon nanotubes. *J. Phys.: Condens. Matter*, 15:5915–5921, 2003.
- [134] S.-H. Jhi, S. G. Louie, and M. L. Cohen. Electronic Properties of Oxidized Carbon Nanotubes. *Phys. Rev. Lett.*, 85:1710–1713, 2000.
- [135] S.-P. Chan, G. Chen, X. G. Gong, and Z.-F. Liu. Oxidation of Carbon Nanotubes by Singlet O₂. *Phys. Rev. Lett.*, 90:086403, 2003.
- [136] J. Hu, X.-D. Xiao, D. F. Ogletree, and M. Salmeron. The structure of molecularly thin films of water on mica in humid environments. *Surf. Science*, 344:221–236, 1995.
- [137] S. Davy, M. Spajer, and D. Courjon. Influence of the water layer on the shear force damping in near-field microscopy. *Appl. Phys. Lett.*, 73:2594–2596, 1998.
- [138] Y. Lill and B. Hecht. Single dye molecules in an oxygen-depleted environment as photostable organic triggered single-photon sources. *Appl. Phys. Lett.*, 84:1665–1667, 2004.
- [139] Y. Fu and J. R. Lakowicz. Single-Molecule Studies of Enhanced Fluorescence on Silver Island Films. *Plasmonics*, 2:1–4, 2007.
- [140] D. A. Vanden Bout, W.-T. Yip, D. Hu, D.-K. Fu, T. M. Swager, and P. F. Barbara. Discrete Intensity Jumps and Intramolecular Electronic Energy Transfer in the Spectroscopy of Single Conjugated Polymer Molecules. *Science*, 277:1074–1077, 1997.
- [141] D. Hu, J. Yu, and P. F. Barbara. Single-Molecule Spectroscopy of the Conjugated Polymer MEH-PPV. *J. Am. Chem. Soc.*, 121:6936–6937, 1999.
- [142] A. T. Siitonen, D. A. Tsyboulski, S. M. Bachilo, and R. B. Weisman. Surfactant-Dependent Exciton Mobility in Single-Walled Carbon Nanotubes Studied by Single-Molecule Reactions. *Nano Lett.*, 10:1595–1599, 2010.
- [143] A. T. Siitonen, D. A. Tsyboulski, S. M. Bachilo, and R. B. Weisman. Dependence of Exciton Mobility on Structure in Single-Walled Carbon Nanotubes. *J. Phys. Chem. Lett.*, 1:2189–2192, 2010.

- [144] K. Yoshikawa, K. Matsuda, and Y. Kanemitsu. Exciton Transport in Suspended Single Carbon Nanotubes Studied by Photoluminescence Imaging Spectroscopy. *J. Phys. Chem. C*, 114:4353–4356, 2010.
- [145] S. Moritsubo, T. Murai, T. Shimada, Y. Murakami, S. Chiashi, S. Maruyama, and Y. K. Kato. Exciton Diffusion in Air-Suspended Single-Walled Carbon Nanotubes. *Phys. Rev. Lett.*, 104:247402, 2010.
- [146] R. M. Russo, E. J. Mele, C. L. Kane, I. V. Rubtsov, M. J. Therien, and D. E. Luzzi. One-dimensional diffusion-limited relaxation of photoexcitations in suspensions of single-walled carbon nanotubes. *Phys. Rev. B*, 74:041405, 2006.
- [147] T. Gokus, L. Cagnet, J. G. Duque, M. Pasquali, A. Hartschuh, and B. Lounis. Mono- and Biexponential Luminescence Decays of Individual Single-Walled Carbon Nanotubes. *J. Phys. Chem. C*, 114:14025–14028, 2010.
- [148] S. Kühn, U. Hakanson, L. Rogobete, and V. Sandoghdar. Enhancement of single molecule fluorescence using a gold nanoparticle as an optical nano-antenna. *Phys. Rev. Lett.*, 97:017402, 2006.
- [149] A. De Vita, J. C. Charlier, X. Blase, and R. Car. Electronic structure at carbon nanotube tips. *Appl. Phys. A.*, 68:283–286, 1999.
- [150] D. L. Carroll, P. Redlich, P. M. Ajayan, J. C. Charlier, X. Blase, A. De Vita, and R. Car. Electronic Structure and Localized States at Carbon Nanotube Tips. *Phys. Rev. Lett.*, 78:2811–2814, 1997.
- [151] J. Hafner, C. L. Cheung, and C. M. Lieber. Direct Growth of Single-Walled Carbon Nanotube Scanning Probe Microscopy Tips. *J. Am. Chem. Soc.*, 121:9750, 1999.
- [152] S. J. Tans and C. Dekker. Potential modulations along carbon nanotubes. *Nature*, 404:834–835, 2000.
- [153] H. Qian, P. T. Araujo, C. Georgi, T. Gokus, N. Hartmann, A. A. Green, A. Jorio, M. C. Hersam, L. Novotny, and A. Hartschuh. Visualizing the local optical response of semiconducting carbon nanotubes to DNA-wrapping. *Nano Lett.*, 8:2706–2711, 2008.
- [154] A. Rajan, M. S. Strano, D. A. Heller, T. Hertel, and K. Schulten. Length-dependent optical effects in single walled carbon nanotubes. *J. Phys. Chem. B*, 112:6211–6213, 2008.
- [155] D. A. Heller, R. M. Mayrhofer, S. Baik, Y. V. Grinkova, M. L. Usrey, and M. S. Strano. Concomitant Length and Diameter Separation of Single-Walled Carbon Nanotubes. *J. Am. Chem. Soc.*, 126:14567–14573, 2004.

-
- [156] Y. Miyauchi, K. Matsuda, Y. Yamamoto, N. Nakashima, and Y. Kanemitsu. Length-Dependent Photoluminescence Lifetimes in Single-Walled Carbon Nanotubes. *J. Phys. Chem. C*, 114:12905–12908, 2010.
- [157] T. E. Kaiser, H. Wang, V. Stepanenko, and F. Würthner. Supramolecular Construction of Fluorescent J-Aggregates Based on Hydrogen-Bonded Perylene Dyes. *Angew. Chem. Intern. Ed.*, 46:5541–5544, 2007.
- [158] E. S. Jeng, A. E. Moll, A. C. Roy, J. B. Gastala, and M. S. Strano. Detection of DNA hybridization using the near-infrared band-gap fluorescence of single-walled carbon nanotubes. *Nano Lett.*, 6:371–375, 2006.
- [159] B. A. Gregg. Excitonic Solar Cells. *J. Phys. Chem. B*, 107:4688–4698, 2003.
- [160] A. Högele, C. Galland, M. Winger, and A. Imamoğlu. Photon Antibunching in the Photoluminescence Spectra of a Single Carbon Nanotube. *Phys. Rev. Lett.*, 100:217401, 2008.
- [161] C. Galland, A. Högele, H. E. Türeci, and A. Imamoğlu. Non-Markovian Decoherence of Localized Nanotube Excitons by Acoustic Phonons. *Phys. Rev. Lett.*, 101:067402, 2008.
- [162] H. Hirori, K. Matsuda, Y. Miyauchi, S. Maruyama, and Y. Kanemitsu. Exciton Localization of Single-Walled Carbon Nanotubes Revealed by Femtosecond Excitation Correlation Spectroscopy. *Phys. Rev. Lett.*, 97:257401, 2006.
- [163] M. Freitag, M. Steiner, A. Naumov, J. P. Small, A. A. Bol, V. Perebeinos, and P. Avouris. Carbon Nanotube Photo- and Electroluminescence in Longitudinal Electric Fields. *ACS Nano*, 3:3744–3748, 2009.
- [164] K. Matsuda, T. Inoue, Y. Murakami, S. Maruyama, and Y. Kanemitsu. Exciton fine structure in a single carbon nanotube revealed through spectral diffusion. *Phys. Rev. B*, 77:193405, 2008.
- [165] V. Perebeinos and P. Avouris. Exciton Ionization, Franz-Keldysh, and Stark Effects in Carbon Nanotubes. *Nano Lett.*, 7:609–613, 2007.
- [166] M. M. Lucchese, F. Stavale, E. H. Martins Ferreira, C. Vilani, M. V. O. Moutinho, R. B. Capaz, C. A. Achete, and A. Jorio. Quantifying ion-induced defects and Raman relaxation length in graphene. *Carbon*, 48:1592–1597, 2010.
- [167] L. G. Cançado, R. Beams, and L. Novotny. Optical Measurement of the Phase-Breaking Length in Graphene. 2008. arXiv:0802.3709v1.
- [168] A. K. Gupta, T. J. Russin, H. R. Gutiérrez, and P. C. Eklund. Probing Graphene Edges via Raman Scattering. *ACS Nano*, 3:45–52, 2009.

- [169] R. Beams, L. G. Cançado, and L. Novotny. Optical Measurement of the Phase-Breaking Length in Graphene. 2010. arXiv:1008.1563v1.
- [170] H. Harutyunyan, T. Gokus, A. A. Green, M. C. Hersam, M. Allegrini, and A. Hartschuh. Defect-Induced Photoluminescence from Dark Excitonic States in Individual Single-Walled Carbon Nanotubes. *Nano Lett.*, 9:2010–2014, 2009.
- [171] F. Tuinstra and J. L. Koenig. Raman Spectrum of Graphite. *J. Chem. Phys.*, 53:1126–1130, 1970.
- [172] L. G. Cançado, K. Takai, T. Enoki, M. Endo, Y. A. Kim, H. Mizusaki, A. Jorio, L. N. Coelho, R. Magalhães-Paniago, and M. A. Pimenta. *Appl. Phys. Lett.*, 88:163106, 2006.
- [173] P. Bharadwaj, P. Anger, and L. Novotny. Nanoplasmonic enhancement of single molecule fluorescence. *Nanotechnol.*, 18:044017–044022, 2007.
- [174] C. Höppener and L. Novotny. Antenna-based optical imaging of single Ca^{2+} transmembrane proteins in liquids. *Nano Lett.*, 8:642–646, 2008.
- [175] S. Berweger, C. C. Neacsu, Y. Mao, H. Zhou, S. S. Wong, and M. B. Raschke. Optical nanocrystallography with tip-enhanced phonon Raman spectroscopy. *Nature Nanotech.*, 4:496–499, 2009.
- [176] B. Krauss, P. Nemes-Incze, V. Skakalova, L. P. Biro, K. Klitzing, and J. H. Smet. Raman Scattering at Pure Graphene Zigzag Edges. *Nano Lett.*, 10:4544–4548, 2010.

Abbreviations

1D	...	one-dimensional
2D	...	two-dimensional
3D	...	three-dimensional
AFM	...	atomic force microscopy
APD	...	avalanche photo diode
BGR	...	band gap renormalization
CCD	...	charge coupled device
DOS	...	density of states
FWHM	...	full-width-at-half-maximum
LA	...	longitudinal acoustic
LO	...	longitudinal optical
MPD	...	multi-phonon decay
NA	...	numerical aperture
PAIEI	...	phonon-assisted indirect exciton ionization
PALM	...	photo-activated localization microscopy
PL	...	photoluminescence
PLL	...	phase-locked loop
PSF	...	point-spread-function
QY	...	quantum yield
RBM	...	radial breathing mode
RRS	...	resonant Raman scattering
SC	...	sodium cholate
SEM	...	scanning electron microscope
SERS	...	surface enhanced Raman scattering
SNOM	...	scanning near-field optical microscopy
STED	...	stimulated emission depletion
STM	...	scanning tunneling microscopy
STORM	...	stochastic optical reconstruction microscopy
SWNT	...	single-walled carbon nanotube
TA	...	transverse acoustic

ABBREVIATIONS

TENOM	...	tip-enhanced near-field optical microscopy
TERS	...	tip-enhanced Raman scattering
TF	...	tuning fork
TO	...	transverse optical
vHS	...	Van Hove singularity

List of Figures

2.1	Unit cell of graphene in real space and reciprocal space	6
2.2	Schematic of the formation of SWNTs by rolling-up a graphene sheet	7
2.3	The Brillouin zones for the (5,5), (5,0) and (4,2)-SWNT	9
2.4	The two-dimensional electronic dispersion relation of graphene	11
2.5	Illustration of the zone-folding approach	12
2.6	Kataura-plot and the zone-folding approach for different types of SWNTs	14
2.7	Transitions in semiconducting SWNTs in the free-particle picture	15
2.8	Schematic of the free-particle and excitonic states in SWNTs	17
2.9	Photoluminescence spectra for different SWNTs	19
2.10	Decay mechanisms in the photoluminescence process	20
2.11	Raman scattering process and Resonance Raman scattering	22
2.12	Phonon dispersion of graphene	24
2.13	Intra-valley Raman scattering processes in graphene	25
2.14	Inter-valley Raman scattering processes in graphene	26
2.15	Raman spectrum for graphene and a metallic SWNTs	27
3.1	Schematic of the angular spectrum representation	32
3.2	The loss of spatial information upon propagation of optical fields	34
3.3	Illustration of the resolution limit in optical microscopy	36
3.4	Different concepts of scanning near-field optical microscopy	37
3.5	Field enhancement at a metal tip and enhancement of Raman and PL	41
3.6	Approach curves of tip-enhanced Raman and PL intensity	43
3.7	Three possible setup designs for a TENOM experiment	45
4.1	Schematic of the experimental setup	50
4.2	Generation and focusing of a radially polarized donut mode	51
4.3	Schematic of the shear-force feedback for tip-sample distance control	53
4.4	SEM images of electrochemically etched gold tips	55
4.5	Simultaneous near-field Raman and PL imaging with APD detection	57
4.6	Spectroscopic near-field imaging	58
5.1	Typical time traces of SWNT PL under laser irradiation	61
5.2	PL decay rate against laser intensity for different substrates and atmospheres .	61
5.3	Evolution of the Raman and PL intensity during laser irradiation	64
5.4	Evaluation of step-like changes in the PL time traces	66

6.1	Experimental and simulated near-field PL image	75
6.2	Simulation of exciton diffusion in an inhomogeneous environment	77
6.3	Simulation of the time-resolved exciton distribution in a SWNT	79
6.4	Calculated PL enhancement for 1D systems with low and high QY	81
7.1	Near-field PL images showing strong intensity variations	84
7.2	PL quenching at ends and defects in experiment and simulation	85
7.3	Spectroscopic image of the PL near a localized quenching site	87
8.1	TENOM images of SWNTs showing strongly localized and bright PL	92
8.2	Exciton localization in a SWNT evidenced by spectroscopic imaging	93
8.3	Exciton localization in a SWNT evidenced by spectroscopic imaging	95
8.4	Simulated near-field PL intensity for the case of exciton energy minima	96
9.1	Illustration of the D-band scattering process in real space	100
9.2	Near-field spectroscopic Raman image of a localized defect site	101
9.3	Mechanical generation of defects by the interaction of gold tip and SWNT	102
9.4	Near-field spectroscopic Raman image of a localized defect site	103
9.5	Spectroscopic images before and after the tip-induced generation of defects	104
9.6	Relation between defect density and D-band intensity	106
A.1	Raman D-band scattering at a graphene edge	112
A.2	Tip-enhancement on graphene	114

List of Publications

During the course of my PhD research, the following peer-reviewed papers have been published:

H. Qian, C. Georgi, N. Anderson, A.A. Green, M.C. Hersam, L. Novotny, A. Hartschuh, "Exciton Energy Transfer in Pairs of Single-Walled Carbon Nanotubes", *Nano Letters* **8**, 1363 (2008)

C. Georgi, N. Hartmann, T. Gokus, A. A. Green, M. C. Hersam, A. Hartschuh, "Photo-induced luminescence blinking and bleaching in individual Single-Walled Carbon Nanotubes", *ChemPhysChem* **9**, 1460 (2008)

H. Qian, P. T. Araujo, C. Georgi, T. Gokus, N. Hartmann, A. A. Green, A. Jorio, M. C. Hersam, L. Novotny, A. Hartschuh, "Visualizing the Local Optical Response of Semiconducting Carbon Nanotubes to DNA-wrapping", *Nano Letters* **8**, 2706 (2008)

H. Qian, C. Georgi, N. Anderson, A. A. Green, M. C. Hersam, L. Novotny, A. Hartschuh, "Exciton transfer and propagation in carbon nanotubes studied by near-field optical microscopy", *physica status solidi (b)* **245**, 2243 (2008)

H. Qian, N. Anderson, C. Georgi, L. Novotny, A. Hartschuh, "Tip-enhanced optical microscopy", book chapter in "Nano-Optics and Near-Field Optical Microscopy", A. Zayats & D. Richards (Eds.) (2009)

C. Casiraghi, A. Hartschuh, H. Qian, S. Pisanec, C. Georgi, A. Fasoli, K. Novoselov, D. Basko, A. C. Ferrari, "Raman Spectroscopy of Graphene Edges", *Nano Letters* **9**, 1433 (2009)

A. Hartschuh, H. Qian, C. Georgi, M. Böhmler, L. Novotny, "Tip-enhanced near-field optical microscopy of carbon nanotubes", *Analytical and Bioanalytical Chemistry* **394**, 1787 (2009)

C. Georgi, M. Böhmler, H. Qian, L. Novotny, A. Hartschuh, "Probing exciton propagation and quenching in carbon nanotubes with near-field optical microscopy", *physica status solidi (b)* **246**, 2683 (2009)

M. Böhmler, N. Hartmann, C. Georgi, F. Hennrich, M. C. Hersam, A. Hartschuh, "Enhancing and Redirecting Carbon Nanotube Photoluminescence by an Optical Antenna", *Optics Express* **18**, 16443 (2010)

LIST OF PUBLICATIONS

C. Georgi, A. A. Green, M. C. Hersam, A. Hartschuh, "Probing Exciton Localization in Single-Walled Carbon Nanotubes using High-resolution Near-field Microscopy", *ACS Nano* **4**, 5914 (2010)

C. Georgi, A. Hartschuh, "Tip-enhanced Raman spectroscopic imaging of localized defects in carbon nanotubes", *Applied Physics Letters* **97**, 143117 (2010)

List of Conferences

DPG Frühjahrstagung 2008, Berlin (Germany), 25.02. - 29.02.2008

Poster: Tip-Enhanced Optical Microscopy of Single-Walled Carbon Nanotubes

416. WE-Heraeus-Seminar: "Ultrafast Nanooptics",

Bad Honnef (Germany), 02.06. - 04.06.2008

Poster: Tip-Enhanced Near-Field Optical Microscopy (TENOM) of Carbon Nanotubes

CeNS Workshop: "Complex Nanosystems: Assembly, Control and Functionality",

San Servolo (Italy), 29.09. - 03.10.2008

Poster: Tip-Enhanced Optical Microscopy of Single-Walled Carbon Nanotubes

DPG Frühjahrstagung 2009, Dresden (Germany), 22.03. - 27.03.2009

Poster: Tip-Enhanced Optical Microscopy of Single-Walled Carbon Nanotubes

Workshop: "Carbon Nanotube Optics",

Kleinwalsertal (Austria), 17.07. - 19.07.2010

Poster: Tip-Enhanced Optical Microscopy of Carbon Nanotubes and Graphene

Workshop: "Frontiers in Nanoscale Spectroscopy and Tomography",

Inlet (USA), 24.06. - 26.09.2009

Oral presentation: Exciton Mobility and Localization in SWNTs studied with Near-Field Microscopy

DPG Frühjahrstagung 2010, Regensburg (Germany), 21.03. - 26.03.2010

Poster: Probing Exciton Propagation and Localization in Single-Walled Carbon Nanotubes

EMRS 2010 Spring Meeting, Strasbourg (France), 07.06. - 11.06.2010

Poster: Probing Exciton Localization in Single-Walled Carbon Nanotubes

Oral presentation: High resolution optical microscopy of single nanostructures

Oral presentation: Probing Exciton Localization in Single-Walled Carbon Nanotubes

3rd German-Japanese Seminar on Nanophotonics,

Ilmenau (Germany), 27.09. - 29.09.2010

Poster: Near-Field Optical Imaging of Defects and Exciton Localization in Carbon Nanotubes

LIST OF CONFERENCES

Workshop "Nano-Carbon Optics", Niederstetten (Germany), 07.10. - 10.10.2010

Poster and Oral presentation: Near-Field Optical Imaging of Defects and Exciton Localization in Carbon Nanotubes

Acknowledgments

First of all I want to thank my doctoral adviser **Prof. Achim Hartschuh** for the opportunity to do this research in his group. He provided a great working atmosphere, constant support and always a handful of cookies.

I also thank **Prof. Tobias Hertel** for his support as the second reviewer of my thesis.

I thank **Huihong Qian**, who introduced me to the near-field setup and showed me how to get real tip-enhancement. She has always been very supportive and a pleasant colleague.

I thank all the other people in our research group, **Tobias, Nicolai, Matthias, Giovanni** and **Nina**, for their constant support and all the fun we had. Working in this group has always been a great pleasure. Thanks for all the discussions, especially the non-scientific ones.

I thank **Alexander Green** and **Prof. Mark Hersam** from the Northwestern University for supporting us with excellent nanotube material. I also acknowledge **Nanointegris** for their free supply of nanotube solutions.

I thank **Steffen Schmidt** for his patience at the SEM, examining hundreds of gold tips over the years. It helped a lot.

A big thank goes to my fellows from the **KVWK**, who always made me feel at home. May the friction be with you.

The biggest thank goes to **Miriam Böhmler**, who changed my life. I am deeply grateful that we have met.